

**Density Functional Theory (DFT) Studies
of Solids and Molecules**

EVA D. ZUREK

**MAX-PLANCK-INSTITUT FÜR FESTKÖRPERFORSCHUNG
STUTTGART, 2006**

Density Functional Theory (DFT) Studies of Solids and Molecules

**Von der Fakultät Chemie der Universität Stuttgart zur
Erlangung der Würde eines Doktors der Naturwissenschaften
(Dr. rer. nat.) genehmigte Abhandlung**

vorgelegt von

EVA D. ZUREK

aus Krakau (Polen)

Hauptberichter:	Prof. Dr. A. SIMON
1. Mithberichter:	Prof. Dr. O. K. ANDERSEN
2. Mithberichter:	Prof. Dr. H. STOLL
Tag der Einreichung:	15.05.2006
Tag der mündlichen Prüfung:	07.07.2006

**MAX-PLANCK-INSTITUT FÜR FESTKÖRPERFORSCHUNG
STUTTGART, 2006**

Contents

Abbreviations	7
Abstract	9
Zusammenfassung	13
1 Introduction	17
2 Theoretical Methods	19
2.1 Density Functional Theory	19
2.2 Linear Muffin Tin Orbitals	22
2.3 Wannier Functions	26
2.4 Properties of Solids	28
2.4.1 Phonons	28
2.4.2 Electron–Phonon Interactions	29
2.5 Molecular Properties	29
2.5.1 NMR Chemical Shifts	30
2.5.2 Thermodynamic Quantities and Frequencies	30
I Solids	35
3 An Introduction to NMTO Wannier-like Functions	37
3.1 Introduction	37
3.2 NMTO Basics	38
3.2.1 Tight-Binding Calculation of the Benzene π -bond	38
3.2.2 NMTOs for Real Systems	41
3.3 Computational Methods	44
3.4 Results and Discussion	44
3.4.1 Graphite: A Semi-Metal	44

3.4.2	Boron Nitride: An Insulator	47
3.5	Summary and Conclusions	49
4	Theoretical Studies of High Pressure Cesium	51
4.1	Introduction	51
4.2	Computational Details	53
4.3	Results and Discussion	54
4.3.1	Energy Bands of Cesium Under Pressure	54
4.3.2	Band Structure of Cesium	56
4.3.3	Phonon Spectra and Electron Phonon Coupling in Cs-II	58
4.3.4	Wannier-like Functions of Cesium	61
4.3.5	Bonding in Cs-IV	64
4.4	Summary and Conclusions	67
5	The Electronic Structure of α-ThSi₂ and β-ThSi₂	69
5.1	Introduction	69
5.2	Computational Details	71
5.3	Results and Discussion	73
5.3.1	Gross Features of the Band Structure of β -ThSi ₂	73
5.3.2	NMTO Wannier-like Functions for β -ThSi ₂	74
5.3.3	Gross Features of the Band Structure of α -ThSi ₂	81
5.3.4	NMTO Wannier-like Functions for α -ThSi ₂	83
5.3.5	Comparison of α -ThSi ₂ and Cs-IV	87
5.4	Summary and Conclusions	92
II	Molecules	95
6	The ¹³C NMR Chemical Shifts in (9,0) Carbon SWNTs	97
6.1	Introduction	97
6.2	Computational Details	99
6.3	Results and Discussion	100
6.3.1	The Electronic Structure of (9,0) SWNTs	100
6.3.2	The NMR Chemical Shifts of (9,0) SWNTs	105
6.4	Summary and Conclusions	115
7	Magic (C₆₀)_n-Metal Compound Clusters	117
7.1	Introduction	117
7.2	Computational Details	119

7.3	Results and Discussion	121
7.3.1	Ba_nC_{60} and K_nC_{60} Clusters	121
7.3.2	Bonding and Stability of $Ba_n(C_{60})_2$ ($1 \leq n \leq 6$) Clusters	123
7.3.3	The Gibbs Free Energy of $Ba_n(C_{60})_2$ ($1 \leq n \leq 6$) Clusters	128
7.3.4	Bonding and Stability of $K_n(C_{60})_2$ ($1 \leq n \leq 6$) Clusters	130
7.3.5	The Gibbs Free Energy of $K_n(C_{60})_2$ ($1 \leq n \leq 6$) Clusters	133
7.3.6	Energetics of Doubly and Singly Charged Clusters	134
7.4	Summary and Conclusions	135
III	Summary	139
8	Conclusions and Outlook	141
	Bibliography	147
	Acknowledgments	157
	Lebenslauf	159

Abbreviations

ADF	Amsterdam density functional
AFM	atomic force microscopy
ASA	atomic spheres approximation
bcc	body centered cubic
<i>BEM</i>	bonding energy per metal atom
<i>BEM</i> _{Ba–Ba}	bonding energy per metal atom which arises from Ba–Ba bonding
<i>BEM</i> _{covalent}	bonding energy per metal atom which arises from covalent bonding
<i>BEM</i> _{geo}	bonding energy per metal atom which arises from geometrical distortions
<i>BEM</i> _{ionic}	bonding energy per metal atom which arises from ionic bonding
B3LYP	Becke 3-parameter hybrid based on Lee-Yang-Parr functional
CPU	computer power unit
DFPT	density functional perturbation theory
DFT	density functional theory
DNA	deoxyribonucleic acid
DOS	density of states
DZ basis	valence double- ζ Slater type basis
DZP basis	valence double- ζ Slater type basis with one set of polarization functions
EA	electron affinity
ECP	effective core potential
ELF	electron localization function
fcc	face centered cubic
FP-LMTO	full potential LMTO
<i>GFM</i>	Gibbs free energy change per metal atom
GGA	generalized gradient approximation
GIAO	gauge-including atomic orbitals
<i>H_{EC}M</i>	change in the finite temperature enthalpy correction per metal atom
HK	Hohenberg-Kohn
HOMO	highest occupied molecular orbital
IP	ionization potential

KKR	Korringa, Kohn, Rostoker
KS	Kohn-Sham
LDA	local density approximation
LMTO	linear muffin tin orbital
LUMO	lowest unoccupied molecular orbital
MAS	magic angle spinning
MD	molecular-dynamics
MPI-FKF	Max Planck Institut für Festkörperforschung
MT	muffin tin
MTZ	muffin tin zero
NMR	nuclear magnetic resonance
<i>N</i> MTO	muffin tin orbitals of order <i>N</i> , also known as 3 rd generation LMTOs
PBE	Perdew, Burke, Ernzerhof
PES	potential energy surface
QM	quantum mechanics
revPBE	revised Perdew, Burke, Ernzerhof
RI	resolution-of-identity
SCF	self-consistent field
$S_{conf} M$	change in the configurational entropy per metal atom
SEM	scanning electron microscopy
SOMO	singly occupied HOMO
STM	scanning tunneling microscopy
STO	Slater type orbital
SV(P) basis	polarized split-valence basis
SWNT	single-walled nanotube
TB	tight-binding
TEM	transmission electron microscopy
TMS	tetramethylsilane
TOF	time of flight
<i>TSM</i>	the temperature multiplied by the entropy change per metal atom
TZP basis	valence triple- ζ Slater type basis with one set of polarization functions
TZ2P basis	valence triple- ζ Slater type basis with two sets of polarization functions
VWN	Vosko-Wilk-Nusair
XPS	X-ray photoemission spectroscopy
ZORA	zero order regular approximation

Abstract

Density functional calculations were performed in order to elucidate the electronic structure, bonding and properties of solids and molecules. In particular, within the first part of this work we outline and employ the *N*MTO method to gain a chemical picture of bonding within the solid state for graphite, boron nitride, cesium, α -ThSi₂ and β -ThSi₂. In the second part we study systems which are typically investigated using solid-state methods, C₆₀-metal clusters and single-walled carbon nanotubes, using molecular calculations.

Part I: Solids

An Introduction to *N*MTO Wannier-like Functions

A method that is able to generate truly minimal basis sets that accurately describe either a group of bands, a band or even just the occupied part of a band is outlined. These basis sets are the so-called *N*MTOs, muffin-tin orbitals of order *N*. For an isolated set of bands, symmetrical orthonormalization of the *N*MTOs yields a set of Wannier functions that are atom-centered and localized by construction. They are not necessarily maximally localized, but a procedure by which this may be accomplished is described. For bands that overlap others, Wannier-like functions may be generated. It is shown that *N*MTOs give a chemical understanding of an extended system. In particular, we construct orbitals for the π and σ bands in an insulator, boron nitride, and a semi-metal, graphite.

Theoretical Studies of High Pressure Cesium

Under pressure, cesium undergoes a number of interesting structural phase transitions accompanied by an $s \rightarrow d$ valence electronic transition. A simple explanation for the raising of the s and lowering of the d band under compression is provided, based upon the pressure theorem applied to an elemental solid in the atomic spheres approximation. The calculated TB-LMTO band structures of Cs-I, Cs-II and Cs-IV are presented. Examination of the band structures decorated with eigenvectors in an orthogonal representation (fat bands) clearly shows that the d -character of the occupied bands increases with increasing pressure. The regions of the Brillouin zone where Lifshitz transitions (changes in the topology of the Fermi surface) occur with decreasing volume are pointed out. FP-LMTO calculations for Cs-II reveal that at a volume

of approximately $v/v_0 = 0.40$ the $T_{[1\bar{1}0]}[\xi\xi0]$ phonon frequencies become imaginary around $\xi = 1/4$ and that the largest electron phonon coupling occurs at $\xi = 0.375$ and $\xi = 0.25$. It is shown that the regions of the Fermi surface which arise due to the Lifshitz transition nest onto each other and cause the structural instability. We illustrate that it is possible to obtain Wannier-like functions for only the occupied states in a metallic system by generating NMTOs for Cs-I, Cs-II and Cs-IV. This allows us to visualize the pressure-induced electronic $s \rightarrow d$ transition. The stability of Cs-IV is analyzed and attributed to the splitting of the xz/yz bands near the N -point.

The Electronic Structure of α -ThSi₂ and β -ThSi₂

The electronic structure and bonding in two intermetallic compounds, α -ThSi₂ and β -ThSi₂, is analyzed. We present NMTO Wannier-like functions which yield a good description of just the occupied bands. The bonding within both structures could be explained in a similar manner. It was found that the lowest lying bands arise from σ -bonding within the silicon sublattice. The π -bonding bands were full and yielded orbitals which showed some hybridization with s and d orbitals on the nearest neighbour thorium atoms. The upper two bands could be described by an $s^*\pi^*$ NMTO which hybridized strongly with the Th d_{z^2} orbitals. Due to the fact that the thorium sublattice in α -ThSi₂ has the same structure as Cs-IV and both systems yield similar electron densities, an alternative analysis of the bonding in α -ThSi₂, based upon the previous results for Cs-IV, was performed. A basis composed of Si σ , π , π^* and Th s , s^* orbitals was found to reproduce the occupied bands quite well. The Th and Cs s -like NMTOs were found to resemble each other, both showing a high degree of sd hybridization. However, the former contained just one lobe pointing along the center of the prisms, whereas the latter consisted of two such lobes.

Part II: Molecules

The ¹³C NMR Chemical Shifts in (9,0) Carbon SWNTs

The electronic structure and ¹³C NMR chemical shifts of finite carbon single-walled nanotube (SWNT) fragments are studied theoretically. Density functional calculations were carried out on progressively longer C₃₀-capped and H-capped systems. The convergence of the properties with respect to the length of the fragments was examined. At relatively short lengths, the H-capped tubes displayed a vanishing HOMO-LUMO gap and therefore such systems were predicted to exhibit “metallic” behaviour. However, the HOMO and LUMO energies themselves were not converged even for the largest system studied, C₁₆₂H₁₈. The chemical shift of the central carbon atom approached ≈ 133 ppm from above. The shift of a carbon atom at the end of a tube was smaller than that in the tube’s center if the carbon was directly bound to a hydrogen, otherwise it was larger. The C₃₀-capped fragments of D_{3d}/D_{3h} symmetry, on

the other hand, were found to be small-gap semiconductors like the infinite (9,0) tubes. It was predicted that for systems containing around 300 atoms the HOMO-LUMO gaps and energies of the frontier orbitals should converge. The shift of the central carbon atom approached ≈ 130 ppm from above while the shifts of the carbon atoms found in the tips of the caps were about 25 ppm larger. The results suggest that the C_{30} -capped fragments are better models for the infinite (9,0) tubes, which should therefore yield chemical shifts of around 130 ppm, in reasonably good agreement with experimental estimates. For the H-capped systems the frontier orbitals were found to be localized on the tubes ends. However, the HOMOs and LUMOs of the tubes terminated with fullerene hemispheres were delocalized over the whole fragment, further suggesting that they are indeed better models for the infinite system. The findings imply that NMR might be useful in the characterization of SWNT samples.

Magic $(C_{60})_n$ -Metal Clusters of Extreme Thermal Stability

We have performed density functional calculations in order to elucidate the enhanced stability and bonding of the recently measured $Ba_3(C_{60})_2$ and $K_4(C_{60})_2$ magic clusters. Possible geometries of a number of different $M_n(C_{60})_2$ ($M = K, Ba, 1 \leq n \leq 6$) clusters have been optimized. For Ba, the energetically most favourable clusters contained Ba atoms sandwiched between two fullerenes with a $C_{60}-Ba_n-C_{60}$ configuration. A bonding analysis revealed that the stability of these clusters results from an interplay between ionic and covalent bonding. The former occurs due to electron transfer from the valence Ba $[6s^2]$ orbitals into the unoccupied fullerene orbitals. The latter is a result of $C_{60} \rightarrow Ba$ back donation into the empty Ba $5d$ orbitals which then covalently bond with orbitals which are unoccupied in the free C_{60} s. For $1 \leq n \leq 3$ and $n = 5, 6$ the dominant interaction is ionic and covalent, respectively. With increasing n , the ionic bonding decreases, as does the average Mulliken charge per Ba atom. This may be explained by realizing that the positively charged Ba atoms repel each other electrostatically and therefore for large n full charge donation cannot occur. Instead, as n increases so does back donation into the Ba $5d$ orbitals, stabilizing clusters where all of the metal atoms are located between the two fullerenes. Thus, the d -element character of Ba is important in order to understand the preferred geometries of, and bonding within, these clusters. The energies revealed that $Ba_3(C_{60})_2$ is the most stable, however it was only slightly more favourable than $Ba(C_{60})_2$. Calculations showed that the entropic contribution to the Gibbs free energy has a larger destabilizing effect on smaller clusters than on larger ones. In full agreement with experiment the Gibbs free energy per metal atom at the experimental conditions (150 K and 10^{-6} Torr) exhibited a distinct minimum for $Ba_3(C_{60})_2$, confirming the stability of this configuration. For the Ba clusters an interplay between covalent and ionic bonding and the entropic contributions to the Gibbs free energy determine which cluster is magic.

The preferred geometries for the K clusters contained all of the metal atoms between the

two C_{60} s for $n \leq 4$. For $n = 5, 6$, a structural transition to a $K-C_{60}-K_{n-2}-C_{60}-K$ configuration was predicted to occur in order to reduce the electrostatic repulsion between positively charged metal ions. The bonding was found to be purely ionic, with an almost complete transfer of the valence $[4s^1]$ electrons into the unoccupied fullerene orbitals. A simple model showed that the most stable structural alternatives minimize the total electrostatic energy. In this case consideration of the finite temperature contributions to the Gibbs free energy changed the order of stability of the clusters: $K(C_{60})_2$ and $K_4(C_{60})_2$ were predicted to be magic at 0 K and 150 K, respectively. Thus, in full agreement with experiment $K_4(C_{60})_2$ was found to be the preferred cluster at the experimental conditions.

Zusammenfassung

Um die Elektronenstruktur, die chemische Bindung und andere Eigenschaften von Molekülen und Festkörpern zu bestimmen, wurden theoretische Berechnungen mit Hilfe der Dichtefunktionaltheorie (DFT) durchgeführt. Im ersten Teil der Arbeit wird die *NMTO*-Methode beschrieben und angewendet. Hierbei wird ein chemisch orientiertes Bild der Bindung in kristallinem Grafit, Bor-Nitrid (BN), Cäsium sowie α -ThSi₂ und β -ThSi₂ erarbeitet. Im zweiten Teil der Arbeit untersuchen wir mittels molekularer Rechnungen C₆₀-Metall-Cluster und einwandige Kohlenstoff-Nanoröhrchen.

Teil I: Festkörper

Einführung in die *NMTO*-Methode

Eine Methode zur Berechnung minimaler Basissätze – sogenannter *NMTOs*, “Muffin–Tin” Orbitale N -ter Ordnung – wird vorgestellt. Sie ermöglicht es, eine Gruppe von Bändern, einzelne Bänder oder auch nur den besetzten Teil eines Bandes korrekt zu beschreiben. Für isolierte Bänder wird mittels symmetrischer Orthogonalisierung der *NMTOs* ein Satz von Wannier-Funktionen erhalten, die per Konstruktion atom-zentriert und lokalisiert sind. Diese sind jedoch nicht notwendigerweise maximal lokalisiert. Deshalb wird eine weitere Technik beschrieben, mit der die Lokalisierung realisiert werden kann. Außerdem wird gezeigt, dass auch für Bänder, die mit anderen Bändern überlappen, Wannier-Funktionen generiert werden können und dass *NMTOs* ein chemisches Verständnis eines Festkörpers ermöglichen. Besonderes Augenmerk wird auf die Konstruktion von σ - und π -Bändern in einem Isolator (BN) und einem Halbmetall (Grafit) gerichtet.

Theoretische Untersuchungen an Cäsium unter hohem Druck

Cäsium erfährt unter Druck eine Anzahl interessanter Phasenumwandlungen, die mit einem $s \rightarrow d$ Elektronenübergang verbunden sind. Eine einfache Erklärung für das Anheben des s -Bandes und das Absenken des d -Bandes, welche auf dem Druck-Theorem für einen elementaren Festkörper in Atom-Sphären-Näherung basiert, wird vorgestellt. Hierzu werden Bandstrukturen für Cs-I, Cs-II und Cs-IV präsentiert. Eine Untersuchung der Bandstrukturen, welche mit den Eigenvektoren in orthogonaler Darstellung verbreitert wurden (“fette Bänder”),

zeigt eindeutig, dass der d -Charakter der besetzten Bänder mit zunehmendem Druck zunimmt. Bereiche der Brillouin-Zone in denen Lifschitz-Übergänge (dies sind Änderungen in der Topologie der Fermi-Fläche) mit abnehmendem Volumen vorkommen, verdienen besondere Beachtung. FP-LMTO-Berechnungen für Cs-II zeigen, dass die $T_{[1\bar{1}0]}[\xi\xi0]$ Phonon-Frequenzen um $\xi = 1/4$ bei einem Volumen von etwa $v/v_0 = 0.40$ imaginär werden und dass die stärkste Elektron-Phonon-Kopplung bei $\xi = 0.375$ und $\xi = 0.25$ erhalten wird. Es wird gezeigt, dass mit Hilfe der NMTOs für Cs-I, Cs-II und Cs-IV Wannier-ähnliche Funktionen für die besetzten Zustände eines metallischen Systems erhalten werden können. Diese Wannier-Funktionen erlauben die Visualisierung des $s \rightarrow d$ Übergangs. Die Stabilität von Cs-IV wird analysiert und mittels der Aufspaltung der xz/yz -Bänder in der Nähe des N -Punkts erklärt.

Die Elektronenstruktur von α -ThSi₂ und β -ThSi₂

In zwei intermetallischen Verbindungen, α -ThSi₂ und β -ThSi₂, wird die Elektronenstruktur untersucht. Wir stellen NMTO-Orbitale vor, die eine gute Beschreibung der besetzten Zustände liefern und erlauben, die chemische Bindung in beiden Systemen zu verstehen. Die am niedrigsten liegenden Zustände können den σ -Bindungen innerhalb des Si-Gitters zugeschrieben werden. Die π -Bänder sind voll besetzt und ergeben Orbitale, die eine leichte Hybridisierung mit den s - und d -Zuständen der angrenzenden Thorium-Atome zeigen. Die zwei am höchsten liegenden Bänder können mittels eines $s^*\pi^*$ -NMTOs beschrieben werden, welches stark mit den Th- d_{z^2} -Zuständen hybridisiert. Da das Th-Gitter in α -ThSi₂ die gleiche Struktur wie Cs-IV und auch eine sehr ähnliche Elektronendichte hat, wurde die Bindung in α -ThSi₂ auf der Basis der Ergebnisse von Cs-IV weiter untersucht. Ein Basissystem aus Si σ -, π -, π^* - und Th s - und s^* -Orbitalen reproduzieren die besetzten Bänder recht gut. Die s -artigen NMTOs von Th und Cs-IV sind sehr ähnlich und zeigen beide eine ausgeprägte sd -Hybridisierung. Allerdings enthalten erstere lediglich ein Dichtemaximum entlang der Prismen-Zentren während letztere zwei solcher Maxima enthalten.

Teil II: Moleküle

¹³C NMR Chemische Verschiebungen von einwandigen (9,0) Kohlenstoff-Nanoröhrchen
 DFT-Rechnungen an molekularen Fragmenten von Kohlenstoff-Nanoröhrchen ("single-walled carbon nanotubes" oder SWNTs) mit zunehmender Länge wurden durchgeführt und die Elektronenstruktur und ¹³C NMR chemische Verschiebungen untersucht. Die endlichen Fragmente wurden mit Wassertoff-Atomen oder je einer halben C₆₀-Einheit terminiert. Für kurze Fragmente zeigen die H-terminierten SWNTs ein metallisches Verhalten (verschwindende HOMO-LUMO-"Bandlücke"), wobei allerdings selbst für ein C₁₆₂H₁₈ Fragment die Grenzorbinale-Energien noch nicht vollständig konvergiert sind. Die chemische Verschiebung der C-Atome im Zentrum konvergiert mit zunehmender Länge von oben gegen einen Wert von etwa 133

ppm. Die Werte der Atome an Rand sind etwas kleiner für C-Atome, die direkt mit einem Wasserstoff-Atom verbunden sind, und etwas größer für die Atome, die nicht mit Wasserstoff verbunden sind. Die C-terminierten Fragmente mit D_{3d}/D_{3h} -Symmetrie sind halbleitend, was auch für das unendlich lange (9,0) SWNT-System erwartet wird. Die chemischen Verschiebungen konvergieren von oben gegen einen Wert von etwa 130 ppm für länger werdende Fragmente. Die Verschiebungen in den C-“Kappen” sind ca. 25 ppm größer. Die Ergebnisse dieser Rechnungen suggerieren, dass die Fragmente mit den C_{30} -Kappen bessere Modelle für unendlich lange (9,0) SWNT darstellen. Wir erwarten daher für (9,0) SWNT eine chemische Verschiebung von ca. 130 ppm. Dieses Ergebnis ist in guter Übereinstimmung mit experimentellen Abschätzungen. Es wird geschlussfolgert, dass NMR in der Zukunft eine wertvolle Methode zur Charakterisierung von SWNTs sein wird.

“Magische” $(C_{60})_n$ -Metall-Cluster mit hoher thermischer Stabilität

Es wurden DFT-Rechnungen durchgeführt, um die hohe Stabilität sowie die Bindungseigenschaften von kürzlich entdeckten, sogenannten “magischen”, $Ba_3(C_{60})_2$ - und $K_4(C_{60})_2$ -Clustern zu verstehen. Verschiedene mögliche Geometrien einiger $M_n(C_{60})_2$ -Oligomere ($M = K, Ba, 1 \leq n \leq 6$) wurden optimiert. Für Ba bestehen die energetisch günstigsten Cluster aus einem Kern von Ba-Atomen zwischen zwei Fullerenen, d.h. einer C_{60} - Ba_n - C_{60} Konfiguration. Eine Analyse der chemischen Bindungen in diesen Clustern zeigte, dass deren Stabilität von einer Balance zwischen ionischer und kovalenter Bindung herrührt. Erstere wird durch einen Elektronentransfer von den Ba- $6s^2$ -Orbitalen zu den unbesetzten tiefliegenden Fulleren-Orbitalen herbeigeführt, letztere ist eine Konsequenz einer Ladungsrückdonation von C_{60} in die leeren Ba- $5d$ Orbitale. Es entsteht so eine kovalente Bindung unter Einbezug der Ba- $5d$ -Orbitale und unbesetzter Orbitale im freien C_{60} . Die wichtigste Wechselwirkung für $1 \leq n \leq 3$ und $n = 5, 6$ ist ionisch beziehungsweise kovalent. Mit steigendem n nimmt die ionische Bindung ab und die kovalente zu. Ebendso nehmen die Mulliken-Ladungen der Metall-Atome zu. Eine einfache Erklärung dafür ist, dass die Metall-Atome sich gegenseitig abstoßen, weswegen in größeren Clustern keine vollständige Ionisierung mehr erfolgen kann. Statt dessen steigt mit größerem n der Beitrag der Rückbindung in die Ba- $5d$ -Orbitale an. Hierbei werden solche Cluster stabilisiert, bei denen sich alle Metallatome zwischen den Fullerenen befinden. Zum Verständnis der Geometrien und der Bindung in diesen Clustern spielt daher der Charakter von Barium als d-Element eine wichtige Rolle. Den Bindungsenergien zufolge ist $Ba_3(C_{60})_2$ der stabilste Cluster. Er ist jedoch nur geringfügig stabiler als $Ba(C_{60})_2$. Aus den Berechnungen folgt, dass entropische Terme in der freien Enthalpie einen größeren destabilisierenden Effekt bei kleineren als bei größeren Clustern haben. Unter Einbezug der entropischen Terme hat daher $Ba_3(C_{60})_2$ eine deutlich größere Stabilität und ist daher im Einklang mit dem Experiment “magisch”. Die Stabilität ergibt sich aus dem Zusammenspiel

von ionischer und kovalenter Bindung sowie den entropischen Termen in der freien Enthalpie.

In der bevorzugten Geometrie der K-Cluster mit $n \leq 4$ befinden sich alle Metall-Atome zwischen den C_{60} -Molekülen. Für $n = 5, 6$ wird ein Strukturübergang vorhergesagt, bei dem $K-C_{60}-K_{n-2}-C_{60}-K$ -Konfigurationen stabiler sind. Deren Stabilität wird mit Hilfe der verminderten elektrostatischen Abstoßung erklärt. Die Bindung zwischen Metall und Fulleren ist rein ionisch, mit einem nahezu kompletten Übergang der $K-4s^1$ -Elektronen in die unbesetzten C_{60} -Orbitale. Ein einfaches Modell mit Atomladungen zeigt, dass das stabilste Strukturmotiv die elektrostatische Abstoßung zwischen den Metallatomen minimiert. Im Fall der K-Cluster ändert der Einbezug der entropischen Terme die Reihenfolge der Stabilitäten: den Rechnungen zufolge ist am absoluten Nullpunkt $K(C_{60})_2$ die stabilste Spezies, während bei 150 K $K_4(C_{60})_2$ am stabilsten ist. Im Experiment wurde ebenfalls $K_4(C_{60})_2$ als der "magische" Cluster identifiziert.

Chapter 1

Introduction

The development of quantum mechanics (QM) in the beginning of the 1900s made it in principle possible to calculate the properties of atoms, molecules and solids. However, the mathematical machinery was not available to solve the equations for these complicated systems. Thus, in 1929 Paul Dirac stated that: “*The fundamental laws necessary for the mathematical treatment of large parts of physics and the whole of chemistry are thus fully known, and the difficulty lies only in the fact that application of these laws leads to equations that are too complex to be solved.*”

It was not only the advent of modern computers, but moreover of approximate means by which the QM equations may be solved, that has made the fields of quantum chemistry and computational condensed matter physics what they are today. One of the most widely used methods is density functional theory (DFT) and its importance was highlighted by the 1998 Nobel Prize in Chemistry which was awarded “to Walter Kohn for his development of the density functional theory and to John Pople for his development of computational methods in quantum chemistry.” Within this thesis DFT is employed to study solids and molecules. The application to very different systems and the calculation of a variety of properties shows that DFT is versatile and ubiquitous in both solid state physics and theoretical chemistry.

In Chapter 2 a basic outline of the standard theoretical methods used in this work is given. Due to the fact that NMTOs are a new approach in band structure calculations and one of the major themes of this thesis, they will be described in greater detail within Chapter 3.

In the first part of this thesis we will apply DFT methods to study bonding in the solid state. Particular emphasis is placed on outlining and using the newly developed NMTO method for the construction of Wannier-like functions for a number of very different compounds.

Chapter 3 is devoted to outlining the NMTO method. The application to well understood systems such as the π -bond in benzene and later to graphite and boron nitride will aid the reader in understanding the associated terminology and concepts.

A procedure which may be used to obtain Wannier-like functions for only the occupied

bands in a metal is presented in Chapter 4. The pressure driven electronic $s \rightarrow d$ transition in cesium is visualized via construction of N MTOs for Cs-I, Cs-II and Cs-IV. FP-LMTO is used to calculate the phonon spectra and electron phonon coupling in Cs-II at different pressures. It is suggested that the Cs-II \rightarrow Cs-III transition is a result of Fermi surface nesting. Finally, the origin of the stability of Cs-IV is discussed.

In Chapter 5 the bonding of two intermetallic compounds, α -ThSi₂ and β -ThSi₂, is analyzed by constructing N MTOs for sets of occupied bands. A truly minimal basis for both structures is proposed. Due to the fact that Cs-IV and α -ThSi₂ have the same space group, with the thorium and cesium atoms located at equivalent positions and that they both display a similar maximum electron density, an alternative basis based upon the calculations on Cs-IV is presented. We compare and contrast the bonding within α -ThSi₂ and Cs-IV.

In the second part of this thesis, quantum chemical programs are used to perform molecular calculations on fullerene-metal clusters and nanotube fragments. In Chapter 6 two different models for finite (9,0) carbon single-walled nanotubes (SWNTs) are considered. The tubes are capped with hydrogen or with half of a C₆₀ hemisphere. The HOMO-LUMO gaps for successively larger fragments are computed and the results are compared with experimental ones for infinite tubes. An analysis of the frontier MOs reveals that those for the H-capped systems are localized on the ends of the tubes whereas those of the C₃₀-terminated systems are delocalized over the whole fragment. The ¹³C NMR chemical shifts of most of the symmetry inequivalent atoms are computed. Based upon the current work and previous theoretical predictions, it is postulated that semiconducting and metallic tubes should display shifts of approximately 130 ppm and 141 ppm, respectively. Thus, it is suggested that NMR might be a useful tool in characterizing SWNT samples.

Chapter 7 presents the results of DF computations on Ba-C₆₀ and K-C₆₀ clusters which were studied experimentally in the Kern group (MPI-FKF). Contrary to common belief, these superstable compound clusters were not found to be characterized by filled geometrical or electronic shells. The most energetically stable isomers of $M_n(C_{60})_2$ ($M = K, Ba$ and $1 \leq n \leq 6$) are computed and the bonding within them is analyzed. Particular emphasis is placed on evaluating the ionic and covalent contributions to the total bonding energy. Next, the entropic and enthalpic contributions to the Gibbs free energies are determined. It is shown that an interplay between ionic (K, Ba) and covalent (Ba) interaction between C₆₀ and the metal atoms, on the one hand, and entropic contributions to the Gibbs free energy, on the other hand, determine the unusual stability.

In the final chapter, the results are summarized and future directions for study are presented.

Chapter 2

Theoretical Methods

2.1 Density Functional Theory

The Born-Oppenheimer approximation assumes that the nuclei of the atoms, molecules or solids remain fixed and generate a static external potential in which the electrons move. For such a system containing N electrons Schrödinger's equation can be written as

$$\left[-\frac{\hbar^2}{2m} \sum_{i=1}^N \nabla_i^2 + \sum_{i=1}^N V_{ext}(\mathbf{r}_i) + \frac{1}{2} \sum_{j \neq i=1}^N \frac{e^2}{|\mathbf{r}_i - \mathbf{r}_j|} \right] \Psi(\mathbf{x}_1, \mathbf{x}_2, \dots, \mathbf{x}_N) = E \Psi(\mathbf{x}_1, \mathbf{x}_2, \dots, \mathbf{x}_N), \quad (2.1)$$

where the first, second and third terms on the left are the kinetic energy (T), the external potential (V_{ext}) and the electron-electron interaction (U), respectively. Here, $\mathbf{x}_i = \mathbf{r}_i, \sigma_i$, where \mathbf{r} and σ are the electronic space and spin coordinates. Most often V_{ext} is the electrostatic potential generated by the nuclei,

$$\sum_{i=1}^N V_{ext}(\mathbf{r}_i) = \sum_{ik} \frac{Z_k e^2}{|\mathbf{r}_i - \mathbf{R}_k|}, \quad (2.2)$$

where Z_k is the atomic number of nucleus k at \mathbf{R}_k . However it may also contain contributions from the surroundings or perturbations of the system.

The usual quantum-mechanical approach taken to solve Eq. 2.1 involves specifying the external potential, calculation of the wavefunction and finally of observables by taking expectation values of operators with this wavefunction. One such observable is the particle density, $n(\mathbf{r})$, which is given as

$$n(\mathbf{r}) = N \int d\sigma_1 \int d\mathbf{x}_2 \int d\mathbf{x}_3 \dots \int d\mathbf{x}_N \Psi^*(\mathbf{x}_1, \mathbf{x}_2, \dots, \mathbf{x}_N) \Psi(\mathbf{x}_1, \mathbf{x}_2, \dots, \mathbf{x}_N). \quad (2.3)$$

Similarly, integrating over all but one spin and space coordinate yields the spin-density, $n(\mathbf{r}, \sigma)$.

The Hohenberg-Kohn (HK) theorem¹ states that for a ground state Eq. 2.3 can be reversed. That is, given a ground-state density, $n_0(\mathbf{r})$, it is possible, in principle, to calculate the cor-

responding ground state wavefunction $\Psi_0(\mathbf{x}_1, \mathbf{x}_2, \dots, \mathbf{x}_N)$. This implies that Ψ_0 , along with all other ground-state observables, are functionals of n_0 ,

$$\Psi_0 = \Psi[n_0](\mathbf{x}_1, \mathbf{x}_2, \dots, \mathbf{x}_N). \quad (2.4)$$

In particular, the relationships established by Hohenberg and Kohn are as follows:

- **Theorem I:** For any system of interacting particles in an external potential $V_{ext}(\mathbf{r})$, the potential is determined uniquely by the ground state particle density n_0 , except for a constant. This implies that the Hamiltonian is fully determined, except for a constant shift of the energy, and therefore the wavefunctions for all ground states may be found. Thus, all of the properties of the system can be calculated from the ground state density n_0 . In essence, the expectation value of any observable \hat{O} is a functional of n_0 :

$$O_0 = O[n_0] = \langle \Psi[n_0] | \hat{O} | \Psi[n_0] \rangle. \quad (2.5)$$

- **Theorem II:** It is possible to define a universal functional for the energy $E[n]$ in terms of the density $n(\mathbf{r})$ valid for any external potential $V_{ext}(\mathbf{r})$. For a given $V_{ext}(\mathbf{r})$, the global minimum of this functional is the exact ground state energy of the system and the density that minimizes the functional is the exact ground state density n_0 . In other words, the ground-state energy, $E_{V_{ext}}[n_0]$, has the useful variational property

$$E_{V_{ext}}[n_0] \leq E_{V_{ext}}[n'] \quad (2.6)$$

where n_0 is the ground state density for V_{ext} and n' is another density.

The HK theorems by themselves do not give a prescription of how one may obtain the ground state density and would probably be only an interesting curiosity if it were not for the Kohn and Sham *ansatz*. Kohn and Sham's approach was to replace the difficult interacting many-body problem of Eq. 2.1 by an auxiliary independent particle problem. In particular, they proposed that the density of the original interacting system can be decomposed into that of a non-interacting system plus all of the many-body terms grouped into an exchange-correlation functional of the density. For the non-interacting system, the independent particle equations can in practice be solved exactly by numerical means. The accuracy of the method is therefore only limited by the approximations made for the exchange-correlation functional. Herein, we will describe the Kohn-Sham² approach which has made DFT the most common method for electronic structure calculations. In the following equations Hartree atomic units ($\hbar = m_e = e = 4\pi/\epsilon_0 = 1$) will be used.

It is useful to decompose the kinetic-energy functional of interacting electrons, $T[n]$ into one part which represents the kinetic energy of non-interacting particles and one which represents the remainder, that is the correlation as

$$T[n] = T_s[n] + T_c[n]. \quad (2.7)$$

$T_s[n]$ is not known as a functional of n , however it can be expressed in terms of the single-particle orbitals, $\phi_i(\mathbf{x})$, of a non-interacting system with density n via

$$T_s[n] = -\frac{1}{2} \sum_{\sigma} \sum_i^N \int d\mathbf{x} \phi_i^*(\mathbf{x}) \nabla^2 \phi_i(\mathbf{x}). \quad (2.8)$$

For a system containing an even number of spin-up and spin-down electrons the density of the original many-body system can be written in terms of the orbitals as

$$n(\mathbf{r}) = \sum_{\sigma} n(\mathbf{r}, \sigma) = \sum_{\sigma} \sum_i^N |\phi_i(\mathbf{x})|^2. \quad (2.9)$$

Thus, all $\phi_i(\mathbf{x})$ are functionals of n and since T_s is an explicit orbital functional it is also an implicit density functional, $T_s[n] = T_s[\phi_i[n]]$. Moreover the total number of electrons N is a simple functional of the density

$$N = \int n(\mathbf{r}) d\mathbf{r}. \quad (2.10)$$

The classical Coulomb self-interaction energy of the electron density, otherwise known as the Hartree energy, is defined as

$$U_H[n] = \frac{1}{2} \int \int d\mathbf{r} d\mathbf{r}' \frac{n(\mathbf{r})n(\mathbf{r}')}{|\mathbf{r} - \mathbf{r}'|} = \frac{1}{2} \int V_C(\mathbf{r})n(\mathbf{r})d\mathbf{r}, \quad (2.11)$$

and the energy of the external potential can be written as a functional of the density

$$\int n(\mathbf{r})V_{ext}(\mathbf{r})d\mathbf{r}. \quad (2.12)$$

The Kohn-Sham approach is to rewrite the energy functional of the interacting system in the form

$$\begin{aligned} E_{KS}[n] &= T[n] + U[n] + V[n] \\ &= T_s[\phi_i[n]] + U_H[n] + E_{xc}[n] + V_{ext}[n] \\ &= T_s[n] + \int n(\mathbf{r}) \left[V_{ext}(\mathbf{r}) + \frac{1}{2} V_C(\mathbf{r}) \right] d\mathbf{r} + E_{xc}[n] \end{aligned} \quad (2.13)$$

where, by definition E_{xc} contains the differences between $T - T_s$ (i.e. T_c) and $U - U_H$. The exchange-correlation (xc) energy, E_{xc} is often decomposed as $E_{xc} = E_x + E_c$, where E_x arises from the Pauli exclusion principle (exchange energy) and E_c (correlation energy) arises from the Coulombic electron-electron repulsion. This term contains all of the many-body effects. If it were known then the exact ground state energy and density of the many-body electron problem could be found by solving the Kohn-Sham equations for independent particles.

Applying the variational principle (Eq. 2.6) to the Kohn-Sham energy and including the constraint Eq. 2.10 via the method of Lagrange multipliers yields

$$\begin{aligned} \frac{\delta}{\delta n} \left[E_{KS} - \mu \left(\int n(\mathbf{r}) d\mathbf{r} - N \right) \right] &= 0 \\ \implies \frac{\delta T_s}{\delta n} + V_C(\mathbf{r}) + \frac{\delta E_{xc}}{\delta n} + V_{ext}(\mathbf{r}) &= \mu, \end{aligned} \quad (2.14)$$

where μ , the Lagrange multiplier, is the chemical potential.

The effective Hamiltonian for a system of non-interacting particles moving in an external potential, V_{KS} , constructed so that the total density of the system is the same as for the real system of interacting electrons

$$V_{KS}(\mathbf{x}) = V_{ext}(\mathbf{r}) + V_C(\mathbf{r}) + V_{xc}(\mathbf{x}), \quad (2.15)$$

with

$$V_{xc} = \frac{\delta E_{xc}}{\delta n} \quad (2.16)$$

is given as

$$H_{KS}(\mathbf{x}) = -\frac{1}{2}\nabla^2 + V_{KS}(\mathbf{x}). \quad (2.17)$$

This gives rise to the Kohn-Sham Schrödinger-like equation

$$(H_{KS} - \varepsilon_i)\phi_i(\mathbf{x}) = 0, \quad (2.18)$$

where ε_i are the eigenvalues of H_{KS} , and the orbitals satisfying Eq. 2.18, ϕ_i , minimize the Kohn-Sham energy.

This yields orbitals that reproduce the density of the original interacting system and the total energy, E_{KS} . These are independent particle equations with a potential that must be found self-consistently with the resulting density. In practice usually one starts with an initial guess for $n(\mathbf{r})$, calculates the resulting $V_{KS}(\mathbf{x})$, then solves Eq. 2.18 for the ϕ_i . The orbitals yield a new density and the process is repeated until it converges.

If the exact functional $E_{xc}[n]$ were known then the exact ground state density could be computed. Unfortunately, this is not the case and two main approximations known as the LDA (local density approximation) and GGA (generalized gradient approximation) are commonly used. In the former, the functional depends only upon the density at the coordinate where the functional is evaluated and in the latter it also takes into account the gradient of the density at this coordinate.

2.2 Linear Muffin Tin Orbitals

Within this section we will first of all describe the muffin tin (MT) approach which forms a basis of augmented localized orbitals.³ Muffin tin orbitals (MTOs) aim to provide a minimal

basis of accurate meaningful orbitals which are constructed from the Kohn-Sham Hamiltonian. The MTO method however leads to non-linear equations due to the fact that the basis functions are energy dependent. Next we will show how the equations may be linearized as in the LMTO (linear MTO) approach. Finally, we comment on the TB (tight-binding) LMTO and the FP (full potential) LMTO techniques.

A muffin tin potential assumes that the total effective potential is spherically symmetric around each atom within an atomic sphere of radius S and to have a constant value V_{MTZ} , the muffin-tin zero, in the interstitial region between the spheres:

$$V_{MT}(\mathbf{r}) = \begin{cases} V(r) & r < S \\ V_{MTZ} & r \geq S \end{cases} . \quad (2.19)$$

Within this potential, the basis functions can be constructed as Bloch sums of muffin tin orbitals (MTOs) defined as

$$\chi_L^{MTO}(\varepsilon, \kappa, \mathbf{r}) = i^l Y_L(\hat{\mathbf{r}}) \begin{cases} \varphi_l(\varepsilon, r) + \kappa \cot(n_l(\varepsilon)) j_l(\kappa r), & r < S \\ \kappa n_l(\kappa r), & r > S \end{cases} \quad (2.20)$$

where $L \equiv lm$, the phase factor i^l is introduced for convenient notation, $\kappa^2 = E - V_{MTZ}$ is the kinetic energy of the basis function outside the MT sphere, $Y_L(\hat{\mathbf{r}})$ are spherical harmonics and j_l and n_l are spherical Bessel and Neumann functions (radial solutions of the Helmholtz equation in three dimensions). The MTO is localized and continuous in value and derivative at the sphere boundary. Since the wavefunction within the sphere itself is modified to account for the influence of the neighbouring atoms, a minimal basis can be constructed in order to accurately describe the system.

It is possible to simplify the construction of MTOs by fixing a value for κ in Eq. 2.20 in such a way which yields accurate results for most problems.⁴ This constant primarily represents the variation of the wavefunction between the atomic spheres. Due to the fact that the wavefunction is required to have the correct value and slope at the sphere boundary, choosing $\kappa = 0$ is a good approximation if the interstitial region is small. In the atomic sphere approximation (ASA), the MT spheres are chosen to have the same volume as the Wigner-Seitz cell. For close-packed solids this leads to overlapping spheres with a small distance between neighbours and the aforementioned approximation is valid. For open structures “empty spheres” may be introduced in the interstitial region to simulate a closed-packed system. In this case the MTO from Eq. 2.20 may be rewritten as

$$\chi_L^{MTO}(\varepsilon, 0, \mathbf{r}) = i^l Y_L(\hat{\mathbf{r}}) \varphi_l(\varepsilon, S) \begin{cases} \frac{\varphi_l(\varepsilon, r)}{\varphi_l(\varepsilon, S)} - \frac{D_l(\varepsilon) + l + 1}{2l + 1} \left(\frac{r}{S}\right)^l, & r < S \\ \frac{l - D_l(\varepsilon)}{2l + 1} \left(\frac{S}{r}\right)^{l+1}, & r > S \end{cases} , \quad (2.21)$$

where $D_l(\varepsilon)$ is the dimensionless logarithmic derivative of $\varphi_l(\varepsilon, r)$ evaluated at the sphere boundary:

$$D_l(\varepsilon) = \left[\frac{r}{\varphi(\varepsilon, r)} \frac{d\varphi(\varepsilon, r)}{dr} \right]_{r=S}. \quad (2.22)$$

For a given κ it is possible to define structure constants, $S_{L,L'}(\mathbf{k})$, which depend only upon the structure. For $\kappa = 0$ and 1 atom/cell they are

$$S_{L,L'}(\mathbf{k}) = g_{l'm',lm} \sum_{\mathbf{T} \neq 0} e^{i\mathbf{k} \cdot \mathbf{T}} \left[\frac{S}{|\mathbf{T}|} \right]^{l''+1} \left[\sqrt{4\pi} i^{l''} Y_{L''}(\hat{\mathbf{T}}) \right]^*, \quad (2.23)$$

where $l'' = l' + l$ and $g_{l'm',lm}$ can be written in terms of Gaunt coefficients⁵ (the integrals over three spherical harmonics).

The MTO basis function for a given wavevector is constructed by placing the MTO on each lattice site with the appropriate Bloch phase factor

$$\chi_{L,\mathbf{k}}^{MTO}(\varepsilon, 0, \mathbf{r}) = \sum_{\mathbf{T}} e^{i\mathbf{k} \cdot \mathbf{T}} \chi_L^{MTO}(\varepsilon, 0, \mathbf{r} - \mathbf{T}). \quad (2.24)$$

The wavefunction in the sphere at the origin is the sum of the head ($r < S$) plus the tails ($r > S$) in other spheres (Eq. 2.21) and can be written as

$$\begin{aligned} \chi_{L,\mathbf{k}}^{MTO}(\varepsilon, 0, \mathbf{r}) &= \varphi_l(\varepsilon, r) i^l Y_L(\hat{\mathbf{r}}) - \frac{D_l(\varepsilon) + l + 1}{2l + 1} \varphi_l(\varepsilon, S) \left(\frac{r}{S} \right)^l i^l Y_L(\hat{\mathbf{r}}) \\ &+ \frac{l - D_l(\varepsilon)}{2l + 1} \varphi_l(\varepsilon, S) \sum_{L'} \left(\frac{r}{S} \right)^{l'} \frac{1}{2(2l' + 1)} i^{l'} Y_{L'}(\hat{\mathbf{r}}) S_{LL'}(\mathbf{k}). \end{aligned} \quad (2.25)$$

The eigenstates are determined as a linear combination of the Bloch MTOs (Eq. 2.25)

$$\varphi_{\mathbf{k}}(\varepsilon, \mathbf{r}) = \sum_L a_L(\mathbf{k}) \chi_{L,\mathbf{k}}^{MTO}(\varepsilon, 0, \mathbf{r}). \quad (2.26)$$

Due to the fact that the first term on the right hand side of Eq. 2.25 is already a solution inside the atomic sphere, $\varphi_{\mathbf{k}}(\varepsilon, \mathbf{r})$ can only be an eigenfunction if the last two terms cancel each other out. This can be accomplished via the following

$$\sum_L (S_{L,L'}(\mathbf{k}) - P_l(\varepsilon) \delta_{L,L'}) a_L(\mathbf{k}) = 0, \quad (2.27)$$

where the potential function is given as

$$P_l(\varepsilon) = 2(2l + 1) \frac{D_l(\varepsilon) + l + 1}{D_l(\varepsilon) - l}. \quad (2.28)$$

Eq. 2.27 yields a set of linear, homogeneous equations for the eigenvectors $a_L(\mathbf{k})$ at a given energy where the determinant of the coefficient matrix vanishes

$$\det[S_{LL'}(\mathbf{k}) - P_l(\varepsilon) \delta_{LL'}] = 0. \quad (2.29)$$

If the hybridization between different l is neglected, the elements of $S_{LL'}(\mathbf{k})$ with $l \neq l'$ are set to zero. In this case the unhybridized bands can be found by solving the following equation

$$|P_l(\varepsilon) - S_{lm,lm'}(\mathbf{k})| = 0. \quad (2.30)$$

This gives rise to the idea of canonical bands which are dependent only upon the crystal structure. All of the material dependent properties are included in the potential function which can then be given in terms of a few parameters that one can calculate using very simple models.⁶

The main drawback of the MTO method is that the basis functions are energy dependent and matching conditions must be satisfied for every eigenstate at its eigenenergy. This leads to non-linear equations which are much more difficult to solve than those obtained using a fixed basis, for example plane waves, gaussians or atomic orbitals. The LMTO method^{4,7} introduces a way in which the equations may be linearized while still retaining accuracy. Within this scheme, if $\Delta\varepsilon$ is the difference between the actual energy and that chosen for linearization (E_v) then the wavefunctions are correct to first order, $(\Delta\varepsilon)$, and the energies to $(\Delta\varepsilon)^3$ due to the variational principle.

Linearization can be achieved by defining augmentation functions as linear combinations of a radial function $\varphi(E_v, r)$ (partial wave) and its energy derivative $\dot{\varphi}(E_v, r)$ evaluated at a chosen fixed energy E_v

$$\dot{\varphi}(E_v, r) \equiv \frac{\partial}{\partial \varepsilon} \varphi(\varepsilon, r)|_{\varepsilon=E_v}. \quad (2.31)$$

In essence $\varphi(E_v, r)$ and $\dot{\varphi}(E_v, r)$ form a basis constructed for a particular system that can be used to calculate all states in a given energy window. Linearization leads to secular equations similar to those for fixed bases.

The LMTO differs from the MTO defined in Eq. 2.20 since: (i) inside the central sphere it is a linear combination of $\varphi_l(E_v, r)$ and $\dot{\varphi}_l(E_v, r)$, and (ii) the tail in other spheres is replaced by a combination of $\dot{\varphi}_l(E_v, r)$. It may be written as

$$\chi_L^{LMTO}(\varepsilon, \kappa, \mathbf{r}) = i^l Y_L(\hat{\mathbf{r}}) \begin{cases} \varphi_l(\varepsilon, r) + \kappa \cot(n_l(\varepsilon)) J_l(\kappa r), & r < S \\ \kappa N_l(\kappa r), & r > S \end{cases} \quad (2.32)$$

where J_l and N_l are Bessel and Neumann functions augmented in such a way so that conditions (i) and (ii) are satisfied. Thus, the LMTO continues smoothly from the central sphere to the interstitial region where it joins smoothly to $\dot{\varphi}$ in the neighbouring sphere.

Choosing $\kappa = 0$ leads to a simplification of the equations in a manner similar to that for MTOs. The linear combination of φ and $\dot{\varphi}$ with logarithmic derivative $D_l(\varepsilon)$ is given as

$$\varphi(D_l, r) = \varphi(r) + \omega(D_l) \dot{\varphi}(r), \quad (2.33)$$

where

$$\omega(D_l) = -\frac{\varphi(s) D - D(\varphi)}{\dot{\varphi}(s) D - D(\dot{\varphi})}, \quad (2.34)$$

and $D(\dot{\varphi})$ is the logarithmic derivative of $\dot{\varphi}$.

Using the notation that $\varphi_{l-}(r) \equiv \varphi_l(D = -l - 1, r)$ and $\varphi_{l+}(r) \equiv \varphi_l(D = l, r)$, the LMTO is defined as

$$\chi_{L\mathbf{k}}^{LMTO}(\mathbf{r}) = \frac{\varphi_{L-}(\mathbf{r})}{\varphi_{l-}(S)} - \frac{1}{\varphi_{l+}(S)} \sum_{L'} \varphi_{L+}(\mathbf{r}) \frac{1}{2(2l' + 1)} S_{LL'}(\mathbf{k}). \quad (2.35)$$

This orbital contains the effects of the neighbours via the structure constants and by the boundary condition that the wavefunction at the sphere boundary is continuous and has a continuous slope. Finally, the eigenvalues are found using the LMTO basis and a variational expression with the full Hamiltonian by solving the eigenvalue equation,

$$\det \left| \langle \mathbf{k}L | \hat{H} | \mathbf{k}L' \rangle - \varepsilon \langle \mathbf{k}L | \mathbf{k}L' \rangle \right| = 0. \quad (2.36)$$

TB-LMTO (tight-binding LMTO) is an “ab-initio” tight-binding scheme where a unitary transformation is applied to transform the LMTO basis functions to a localized, short-range form. This yields a minimal basis tight-binding formulation where all of the Hamiltonian matrix elements are determined from the the Kohn-Sham equations. In Chapters 3-5 the TB-LMTO method is used to calculate the band structures of graphite, boron nitride, cesium under pressure, α -ThSi₂ and β -ThSi₂.

In FP-LMTO⁸ (full potential LMTO), it is no longer required that the potentials and charge densities retain spherical symmetry. The unit cell is divided into non-overlapping MTs and the interstitial region between them. In the former region the effective potential is expanded in spherical harmonics and in the latter by a Fourier series. The basis functions are linearized in the same fashion as within LMTO and in principle the accuracy of the method is only limited by the linearization. In Chapter 4 FP-LMTO is used to calculate the band structure of Cs-II for different v/v_0 .

2.3 Wannier Functions

Wannier functions,⁹⁻¹¹ the solid state analogue of Boys localized molecular orbitals in chemistry, are orthonormal localized functions which span the same space as the eigenstates of a band or a group of bands. In a crystal, the eigenstates of the Hamiltonian are also the eigenstates of the translation operations, \hat{T}_n , leading to the Bloch theorem

$$\Psi_{i\mathbf{k}}(\mathbf{r}) = e^{i\mathbf{k}\cdot\mathbf{r}} u_{i\mathbf{k}}(\mathbf{r}). \quad (2.37)$$

Due to the fact that the phase of each eigenstate is arbitrary, the Bloch functions are subject to a “gauge transformation”, which leaves physically meaningful quantities unchanged, as

$$\Psi_{i\mathbf{k}}(\mathbf{r}) \rightarrow \tilde{\Psi}_{i\mathbf{k}}(\mathbf{r}) = e^{i\phi_i(\mathbf{k})} \Psi_{i\mathbf{k}}(\mathbf{r}). \quad (2.38)$$

Since the Bloch functions are periodic in reciprocal space, the Wannier functions are generated from a Fourier transformation of the Bloch eigenstates. The function for the cell labeled by the lattice point \mathbf{T} for the band i can be found from

$$w_i(\mathbf{r} - \mathbf{T}) = \frac{V}{(2\pi)^3} \int_{BZ} d\mathbf{k} e^{-i\mathbf{k}\cdot\mathbf{T}} \Psi_{i\mathbf{k}}(\mathbf{r}) = \frac{V}{(2\pi)^3} \int_{BZ} d\mathbf{k} e^{i\mathbf{k}\cdot(\mathbf{r}-\mathbf{T})} u_{i\mathbf{k}}(\mathbf{r}), \quad (2.39)$$

where V is the cell volume. For a different cell, \mathbf{T}' , the function w_i remains unchanged, but is translated by $\mathbf{T}' - \mathbf{T}$. Moreover, Eq. 2.39 shows that for the L lattice translations

$$\Psi_{i\mathbf{k}}(\mathbf{r}) = \sum_{\mathbf{T}=1}^L e^{-i\mathbf{k}\cdot\mathbf{T}} w_i(\mathbf{r} - \mathbf{T}). \quad (2.40)$$

In general, the Wannier functions can be defined as a linear combination of the Bloch functions of different bands. For example, in diamond the combination of the occupied s and p bands are needed to form the chemically intuitive sp^3 bond orbital. If $U_{ji}^{\mathbf{k}}$ is a \mathbf{k} -dependent unitary transformation, then each function is given by 2.39 with

$$u_{i\mathbf{k}} = \sum_j U_{ji}^{\mathbf{k}} u_{j\mathbf{k}}. \quad (2.41)$$

As can be seen from Eq. 2.39 with Eqs. 2.38 or 2.41, variations in $\phi_i(\mathbf{k})$ and $U_{ji}^{\mathbf{k}}$ change the relative phases and amplitudes of the Bloch functions for different bands i at different \mathbf{k} . Thus, Wannier functions are not uniquely defined. This is one of their most serious drawbacks. Nonetheless, they can be useful as minimal basis sets for order- \mathbf{N} methods and in constructing many-electron wavefunctions for the study of, for example, strongly correlated systems.

A number of different approaches which aim to construct chemically intuitive Wannier functions have appeared. In maximally projected Wannier functions, the phases of the Bloch functions can be chosen so that the Wannier function has a maximum overlap with a chosen localized function, for example at a bond center or a p -like state on an atom.^{12,13} On the other hand, the so-called maximally localized Wannier functions¹⁴ require minimization of the mean square spread, Ω , defined by

$$\Omega = \sum_{i=1}^{N_{bands}} [\langle r^2 \rangle_i - \langle \mathbf{r} \rangle_i^2] \quad (2.42)$$

where $\langle \dots \rangle_i$ is the expectation value over the i th Wannier function. This method is often used in electronic structure calculations and is equivalent to the Boys localization used in quantum chemistry.¹⁵

At times it might prove useful to construct Wannier-like functions for “entangled” bands, ones which are not isolated from others. Here, the desired bands lie within a given energy range but cross with, or are attached to others which extend further out in energy. In this case

it is unclear exactly which bands to choose, particularly in those regions of k -space where hybridization with unwanted bands occurs. If the bands cannot be disentangled then there will be non-analytic properties which arise from mixing with other bands in the integrals over the Brillouin zone and the Wannier functions, as defined previously, will not be useful. However, it is possible to construct useful *Wannier-like functions* which yield a localized basis for a subspace of bands spanning a desired energy range. There are basically two main approaches how this may be done. The first maximizes the overlap with the Bloch functions only over an energy window, generating a finite subspace of bands that describes those within the chosen range.¹⁶ The second identifies the types of orbitals which are involved and generates a reduced set of localized functions that describes the bands spanning a specified energy window.¹⁷ This is the general idea behind the *NMTO* method, which will be described and applied in Chapters 3, 4 and 5.

2.4 Properties of Solids

Many properties of solids are found by variations of the energy around the equilibrium geometry configuration. Phonons, magnons and dielectric response functions are only a few examples. A number of schemes may be employed to calculate these properties, however here we will only give a brief outline of the methods that have been used within this work.

2.4.1 Phonons

In Section 4.3.3 we calculate the phonon spectrum of Cs-II for different v/v_0 using a FP-LMTO code that employs density functional perturbation theory (DFPT) for calculating the linear response to an external perturbation.¹⁸ The main advantage of DFPT is that the standard equations with sums over empty states can be rewritten only in terms of the occupied states, which are easily evaluated in DFT.

The first-order change in the density, in terms of the wavefunction, is given as

$$\Delta n(\mathbf{r}) = 2\text{Re} \sum_{i=1}^N \varphi_i^*(\mathbf{r}) \Delta \varphi_i(\mathbf{r}) \quad (2.43)$$

where $\Delta \varphi_i(\mathbf{r})$ can be calculated from first-order perturbation theory via

$$(H_{KS} - \varepsilon_i) |\Delta \varphi_i\rangle = -(\Delta V_{KS} - \Delta \varepsilon_i) |\varphi_i\rangle. \quad (2.44)$$

In Eq. 2.44 H_{KS} is the unperturbed Kohn–Sham Hamiltonian, $\Delta \varepsilon_i = \langle \varphi_i | \Delta V_{KS} | \varphi_i \rangle$ is the first-order variation of the eigenvalue ε_i , and the change in the potential is found by

$$\Delta V_{KS}(\mathbf{r}) = \Delta V_{ext}(\mathbf{r}) + \int d\mathbf{r}' \frac{\Delta n(\mathbf{r}')}{|\mathbf{r} - \mathbf{r}'|} + \int d\mathbf{r}' \frac{dV_{xc}(\mathbf{r}')}{dn(\mathbf{r}')} \Delta n(\mathbf{r}'). \quad (2.45)$$

The correction to the occupied orbitals can be obtained by

$$(H_{KS} - \varepsilon_i)|\Delta\varphi_i\rangle = -(1 - \hat{P}_{\text{occ}})\Delta V_{KS}|\varphi_i\rangle \quad (2.46)$$

where the projection operator is defined as

$$\hat{P}_{\text{occ}} = \sum_{i=1}^N |\varphi_i\rangle\langle\varphi_i|. \quad (2.47)$$

The basic self-consistent algorithm is to solve Eq. 2.46 for $\Delta\varphi_i$ using the definition of \hat{P}_{occ} in Eq. 2.47 and V_{KS} (Eq. 2.45) in terms of $\Delta n(\mathbf{r})$ from Eq. 2.43. Since Δn depends on the occupied orbitals, $\Delta\varphi_i$, a self-consistent loop is established. In practice the problem is often more complicated. For example in the FP-LMTO scheme the basis functions are dependent upon the perturbation and this change must also be calculated.

2.4.2 Electron–Phonon Interactions

The calculation of electron–phonon interactions is important not only in the study of superconductivity, but also of other phenomena such as structural phase transitions. In Section 4.3.3 the electron–phonon coupling along a given phonon mode for Cs-II under pressure is calculated. As the phonon mode softens, the coupling increases leading to an instability in the fcc structure.

The matrix element for the emission or absorption of a phonon $\nu\mathbf{q}$ with frequency ω while scattering an electron from the state $i\mathbf{k}$ to $j\mathbf{k} + \mathbf{q}$ is given as

$$g_{i\mathbf{k};j\mathbf{k}+\mathbf{q}}(\nu) = \frac{1}{\sqrt{2M\omega_{\nu\mathbf{q}}}} \langle i\mathbf{k} | \Delta V_{\nu\mathbf{q}} | j\mathbf{k} + \mathbf{q} \rangle, \quad (2.48)$$

where M is the reduced mass and $1/\sqrt{2M\omega_{\nu\mathbf{q}}}$ is the zero-point phonon amplitude. At the Fermi surface, the coupling to the phonon branch ν is found from

$$\lambda_{\nu} = \frac{2}{N_F} \sum_{\mathbf{q}} \frac{1}{\omega_{\nu\mathbf{q}}} \sum_{ij\mathbf{k}} |g_{i\mathbf{k};j\mathbf{k}+\mathbf{q}}(\nu)|^2 \delta(\varepsilon_{i\mathbf{k}}) \delta(\varepsilon_{j\mathbf{k}+\mathbf{q}} - \varepsilon_{i\mathbf{k}} - \omega_{\nu\mathbf{q}}). \quad (2.49)$$

Here, N_F is the density of states at the Fermi level, $\omega_{\nu\mathbf{q}}$ is the energy of phonon ν with wavevector \mathbf{q} and $\varepsilon_{i\mathbf{k}}$ is the energy of the band i with wavevector \mathbf{k} .

A number of methods exist in order to evaluate $\Delta V_{\nu\mathbf{q}}$. Within this work, this is done by calculating the phonons via DFPT as outlined above.^{18,19}

2.5 Molecular Properties

Many molecular properties may be calculated as second derivatives of the energy, E . These properties include, but are not limited to: NMR parameters (chemical shifts, nuclear spin-spin coupling constants), EPR observables, harmonic force constants and infrared intensities.

2.5.1 NMR Chemical Shifts

Chapter 6 will be concerned with calculating the nuclear magnetic resonance (NMR) chemical shifts of finite single-walled carbon nanotubes (SWNTs). Classically, the interaction of an external magnetic field, \mathbf{B} , with a nuclear magnetic moment is given by

$$E = -\boldsymbol{\mu}_A \cdot \mathbf{B}. \quad (2.50)$$

Here, $\boldsymbol{\mu}_A$ is the spin magnetic moment of a particular nucleus and \mathbf{B} is an external static homogeneous magnetic field. In atoms, molecules and solids \mathbf{B} is shielded by the electrons and thus the nucleus interacts with an effective field. Thus, if $\boldsymbol{\sigma}$ is the nuclear shielding tensor for nucleus A in a given chemical environment,

$$E = -\boldsymbol{\mu}_A \cdot (1 - \boldsymbol{\sigma})\mathbf{B}. \quad (2.51)$$

Since the term $-\boldsymbol{\mu}_A \cdot \mathbf{B}$ is not usually included in zero-order quantum chemistry computations, the nuclear shielding tensor may be written as²⁰

$$\sigma_A = \left. \frac{\partial^2 E}{\partial \mathbf{B} \partial \boldsymbol{\mu}_A} \right|_{\mathbf{B}=0, \boldsymbol{\mu}_A=0}. \quad (2.52)$$

This second derivative may be computed analytically, however often numerical methods are used due to the fact that the energy expression may involve many complicated terms. The formal agreement with Eq. 2.52 is established by expanding E , H , and Ψ in a perturbation series in $\boldsymbol{\mu}_A$ and \mathbf{B} , then collecting terms that are bi-linear in both. $\boldsymbol{\sigma}$ is dimensionless and is usually given in units of 10^{-6} (parts per million, or ppm). The isotropic shielding constant, σ , is the rotational average. Experimental data usually report the chemical shift, δ , which is defined as

$$\delta = \sigma^{reference} - \sigma. \quad (2.53)$$

Here, $\sigma^{reference}$ is determined for a reference nucleus in a reference compound. For ^1H and ^{13}C NMR the experimental reference often chosen is TMS (tetramethylsilane). NMR quantum chemical calculations of similar molecules often yield errors with the same sign and order of magnitude, for a given basis set and functional. Thus, computationally a better reference may be a molecule with an experimentally well known chemical shift which is chemically similar to the one being studied.

2.5.2 Thermodynamic Quantities and Frequencies

The energies computed using quantum chemical programs are for isolated, stationary nuclei at 0K. Comparison to experimental values therefore necessitates the addition of terms which arise from the zero-point vibration and from the finite temperature of the experiment. From

statistical mechanics and assuming ideal gas behavior, the change in enthalpy from 0K to some finite temperature T is given by

$$\Delta H(T) = H_{trans}(T) + H_{rot}(T) + \Delta H_{vib}(T) + RT. \quad (2.54)$$

The translational, rotational and change in vibrational enthalpy correction and the zero-point energy can be written, respectively, as²¹

$$H_{trans}(T) = (3/2)RT, \quad (2.55)$$

$$H_{rot}(T) = (3/2)RT \quad (RT \text{ for a linear molecule}), \quad (2.56)$$

$$\Delta H_{vib}(T) = H_{vib}(T) - H_{vib}(0) = N_0 h \sum_i \frac{v_i}{(e^{hv_i/kT} - 1)}, \quad (2.57)$$

$$H_{vib}(0) = \frac{1}{2} h \sum_i v_i, \quad (2.58)$$

where the summations in Eqs. 2.57 and 2.58 are performed over all i normal modes.

Under the assumption of ideal gas behavior, statistical mechanics may also be used to obtain equations for the total entropy, given as²¹

$$S(T) = S_{trans}(T) + S_{rot}(T) + S_{vib}(T) + S_{el} - nR[\ln(nN_0) - 1] \quad (2.59)$$

The translational, rotational, vibrational and electronic entropic contributions can be calculated using Eqs. 2.60-2.63.²¹

$$S_{trans}(T) = nR \left\{ \frac{3}{2} + \ln \left[\left(\frac{2\pi M k T}{2} \right)^{3/2} \left(\frac{nRT}{P} \right) \right] \right\} \quad (2.60)$$

$$S_{rot}(T) = nR \left\{ \frac{3}{2} + \ln \left[\frac{(\pi v_A v_B v_C)^{1/2}}{s} \right] \right\} \quad (2.61)$$

$$S_{vib}(T) = nR \sum_i \{ (u_i e^{u_i} - 1)^{-1} - \ln(1 - e^{-u_i}) \} \quad (2.62)$$

$$S_{el} = nR \ln \omega_{el} \quad (2.63)$$

In Eqs. 2.54-2.63 the following notation is used,

- n = moles of molecules
- R = ideal gas constant
- N_0 = Avogadro's number
- M = mass of molecule
- k = Boltzmann's constant
- T = temperature
- h = Planck's constant
- P = pressure
- I_A, I_B, I_C = principle moments of inertia
- $\nu_A, \nu_B, \nu_C = h^2/8\pi I_A kT$, etc.
- s = symmetry number
- $u_i = h\nu_i/kT$
- ν_i = vibrational frequencies
- ω_{el} = electronic ground state degeneracy.

Thus in order to calculate thermodynamic quantities, the vibrational frequencies of a molecule must be known. Consider a molecule consisting of N atoms whose nuclei are located near their equilibrium positions. The mass-weighted cartesian displacements for nucleus A , (X_A , Y_A and Z_A) are given by taking the difference between the equilibrium and displaced cartesian coordinates and multiplying them by $\sqrt{M_A}$, where M_A is the mass of the given nucleus. Assuming the harmonic approximation and truncating the energy expansion around the equilibrium position to second order yields the energy in terms of $\mathbf{X} = (X_1, \dots, X_N)$ as

$$E = (1/2)\mathbf{X}^\dagger \mathbf{Q} \mathbf{X} \quad (2.64)$$

where the energy scale has been chosen so that $E = 0$ at the equilibrium position. The $3N \times 3N$ matrix \mathbf{Q} is given by²⁰

$$\mathbf{Q} = \left. \frac{\partial^2 E}{\partial \mathbf{X} \partial \mathbf{X}'} \right|_{\mathbf{X}=\mathbf{X}'=0} \quad (2.65)$$

with the eigenvectors, \mathbf{q}_α , yielding the normal modes and the eigenvalues, k_α , the respective mass-weighted force constants. Within the harmonic approximation, the vibrational frequencies, ω , are related to the mass-weighted force constant via

$$\omega_\alpha = \sqrt{k_\alpha}. \quad (2.66)$$

In some quantum chemical programs the second derivative of the energy with respect to the nuclear displacements is calculated analytically. In cases where analytic derivatives are not available, but analytic gradients are found, the second derivative in Eq. 2.65 is replaced by a finite difference,

$$Q = \left. \frac{\partial^2 E}{\partial \mathbf{X} \partial \mathbf{X}'} \right|_{\mathbf{X}=\mathbf{X}'=0} \approx \frac{\Delta(\partial E / \partial \mathbf{X})|_{\mathbf{X}=0}}{\Delta \mathbf{X}'}, \quad (2.67)$$

and the frequencies are said to be calculated numerically.

Within Chapter 7 we will use the aforementioned equations, along with the calculated analytic frequencies, in order to determine the entropic and enthalpic contributions to the Gibbs free energy of a number of $(\text{C}_{60})_2$ -metal clusters.

Part I

Solids

Chapter 3

An Introduction to N MTO Wannier-like Functions

3.1 Introduction

The electronic structure of condensed matter is usually described in terms of one-electron basis sets. Basis functions used for computation are often simple, eg. Gaussians or plane waves, but their number is large, 1-2 orders of magnitude larger than the number of electrons to be described. This is so because the potential in the effective one-electron Schrödinger equation, arising say in density functional theory, is rather deep inside the atoms. The results of this kind of computation therefore require interpretation and simplification in terms of a small set of intelligible orbitals. The results of band-structure calculations for crystals, for instance, are often parameterized in terms of tight-binding models.

The Car-Parinello technique for performing *ab initio* molecular-dynamics simulations using density functional theory, pseudopotentials, plane-wave basis sets, and supercells,²² created a need to visualize chemical bonds, and this caused renewed interest in generating localized Wannier functions for the occupied bands. For a set of M isolated energy bands, $\varepsilon_j(\mathbf{k})$, the M Wannier functions, $w_m(\mathbf{r} - \mathbf{T})$, enumerated by m and by the L ($\rightarrow \infty$) lattice translations, \mathbf{T} , is a set of orthonormal functions which spans the eigenfunctions,

$$\Psi_{j\mathbf{k}}(\mathbf{r}) = L^{-\frac{1}{2}} \sum_{\mathbf{T}=1}^L \sum_{m=1}^M w_m(\mathbf{r} - \mathbf{T}) u_{jm} e^{i\mathbf{k}\cdot\mathbf{T}} \quad (3.1)$$

with eigenvalues $\varepsilon_j(\mathbf{k})$, of the one-electron Schrödinger equation. The Bloch states, Eq. 3.1, are delocalized, and the set is enumerated by the band index j and the Bloch vector \mathbf{k} . Wannier functions are not unique, because performing a unitary transformation, $W_{m,m';\mathbf{T}-\mathbf{T}'}$, of one set produces another set which also satisfies Eq. 3.1, merely with different $j\mathbf{k}$ -dependent phases of the Bloch functions. For molecules, it had long been recognized that chemical bonds should

be associated with those linear combinations of the occupied molecular orbitals which are most localized, because those linear combinations are most invariant to the surroundings.¹⁵ For infinite periodic systems, Marzari and Vanderbilt have developed a useful method for projecting from the Bloch states a set of so-called maximally localized Wannier functions.^{14,23,24}

This chapter deals with a different kind of basis set, specifically, minimal basis sets of localized orbitals, the newly developed *N*MTOs (Muffin Tin Orbitals of order *N*, also known as 3rd generation MTOs.^{17,25–27}) We shall demonstrate that with *N*MTOs it is possible to generate Wannier functions directly, instead of via projection from the delocalized Bloch states. *N*MTOs are constructed from the partial-wave solutions of Schrödinger's equation for spherical potential wells (overlapping muffin tins) and *N*MTO sets are therefore selective in energy. As a consequence, one can construct an *N*MTO set which picks a specific set of isolated energy bands. Since *N*MTOs are atom-centered and localized by construction, they do –after symmetrical orthonormalization– form a set of localized Wannier functions which, if needed, can be recombined locally to have maximal localization. The *N*MTO technique is primarily for generating a localized, minimal basis set with specific orbital characters, and it can therefore be used also to pick a set of bands which overlap other bands outside the energy region of interest. The corresponding *N*MTOs –orthonormalized or not– we refer to as Wannier-like.

*N*MTO-generated Wannier functions have so-far been used only in a few cases to visualize chemical bonding.^{27–29} In Chapter 5 we will employ *N*MTOs to analyze the bonding in α -ThSi₂ and β -ThSi₂. They have more often been used to construct Hubbard Hamiltonians for strongly correlated 3*d*-electron systems.^{28–32} In the future, it may be possible to use *N*MTOs for real-space electronic-structure methods in which the computational effort increases merely linearly with system size (order-*N* methods).^{33,34}

Within this chapter we will focus mainly on showing how *N*MTOs may be used to pick specific states in insulators and semi-metals, namely boron nitride and graphite. In Chapter 4, we will outline a strategy how this may be extended to the description of only the occupied states in a metal. Since *N*MTOs are currently a non-standard method in electronic structure calculations, and more complicated than plane waves, we start out by illustrating the main ideas by performing an elementary analytical calculation of the π -bonds in the simplest tight-binding (TB) model of benzene. Then follows a concise summary of the *N*MTO formalism.

3.2 *N*MTO Basics

3.2.1 Tight-Binding Calculation of the Benzene π -bond

The simplest TB model for the six π -electrons in benzene has six orthonormal p_z -orbitals, $\varphi_1, \dots, \varphi_6$, placed on the consecutive corners of the hexagon. The hopping integrals over the

short (double) bonds are: $H_{12} = H_{34} = H_{56} = -(1 + d)$, and those over the long (single) bonds are: $H_{61} = H_{23} = H_{45} = -(1 - d)$, where d is the dimerization.

In order to calculate the Wannier function for the three occupied bonding states, it is convenient to *partition* the orbitals into those on the even (e)- and those on the odd (o)-numbered sites. The eigenvalue equations are then: $H_{oo}u_o + H_{oe}u_e = \varepsilon 1_{oo}u_o$ and $H_{eo}u_o + H_{ee}u_e = \varepsilon 1_{ee}u_e$, in terms of the 3×3 blocks of the Hamiltonian and the unit matrices. Solving the last set of equations for the eigenvector for the even orbitals yields:

$$u_e = (\varepsilon - H_{ee})^{-1} H_{eo}u_o, \quad (3.2)$$

and inserting in the first equations results in the eigenvalue equation:

$$\left[H_{oo} + H_{oe} (\varepsilon 1_{ee} - H_{ee})^{-1} H_{eo} \right] u_o = \varepsilon 1_{oo}u_o, \quad (3.3)$$

for the energy dependent (Löwdin) *downfolded* Hamiltonian for the odd sites.

In the present case where there is no hopping between even or odd sites, $H_{ee} = H_{oo} = 0$. Moreover,

$$H_{eo} = H_{oe}^\dagger = \begin{pmatrix} -(1+d) & -(1-d) & 0 \\ 0 & -(1+d) & -(1-d) \\ -(1-d) & 0 & -(1+d) \end{pmatrix}, \quad (3.4)$$

and

$$H_{oo} + H_{oe} (\varepsilon 1_{ee} - H_{ee})^{-1} H_{eo} = \frac{1}{\varepsilon} \begin{pmatrix} 2(1+d^2) & 1-d^2 & 1-d^2 \\ 1-d^2 & 2(1+d^2) & 1-d^2 \\ 1-d^2 & 1-d^2 & 2(1+d^2) \end{pmatrix}. \quad (3.5)$$

The latter, downfolded Hamiltonian is periodic with period 3 and is therefore diagonalized by the unitary transformation

$$U_{ok} = \begin{pmatrix} \frac{1}{\sqrt{3}} & \frac{-1}{\sqrt{2}} & \frac{-1}{\sqrt{6}} \\ \frac{1}{\sqrt{3}} & \frac{1}{\sqrt{2}} & \frac{-1}{\sqrt{6}} \\ \frac{1}{\sqrt{3}} & 0 & \frac{2}{\sqrt{6}} \end{pmatrix}, \quad (3.6)$$

yielding singly degenerate a -states ($k = 0$) with $\varepsilon = \pm 2$ and doubly degenerate e -states ($k = \pm 1$) with $\varepsilon = \pm \sqrt{1 + 3d^2}$. The even components of the eigenvectors are obtained from Eq. 3.2: $U_{ek} = \varepsilon^{-1} H_{eo} U_{ok}$, and finally we can renormalize: $u = U / \sqrt{2}$.

Having found all six Bloch eigenstates, we need to form three Wannier functions, that is, three *congruent* linear combinations of the bonding states. The three *downfolded* p_z -orbitals, χ_o , defined by: $\chi_o U_{ok} = \varphi_o u_{ok} + \varphi_e u_{ek}$, are obviously congruent. Moreover, they are *localized* in the sense that χ_1 vanishes on the other odd sites (3 and 5). In the present case, they are also orthonormal and, hence, Wannier functions. Left-multiplication with $(U_{ok})^{-1} = U_{ko}$ yields:

$$\chi_1 = \frac{1}{\sqrt{2}} \left[\varphi_1 + \left(\frac{2}{3} + d \right) \varphi_2 + \left(\frac{2}{3} - d \right) \varphi_6 - \frac{1}{3} \varphi_4 \right], \quad (3.7)$$

and χ_3 and χ_5 by cyclic permutation of site indices. Here and in the following, we work merely to first order in the dimerization, d . The Wannier function in Eq. 3.7 is essentially the NMTO. It is atom-centered and, as the dimerization increases, it becomes lopsided towards site 2, i.e., it spills into the short bond. It breaks the symmetry (when $d \neq 0$) because it was chosen to vanish on the *odd* sites different from its own, and it is not *maximally* localized (unless $d = 0$). Nevertheless, it is a fairly simple matter to achieve maximal localization and, hence, to restore the symmetry, by finding a unitary transformation, $W_{T-T'}$, which maximizes eg. $\langle |w|^4 \rangle \equiv \sum_{R=1}^6 |w|^4$. Here, $w_1 \equiv \sum_T W_{1-T} \chi_T$ is the maximally localized Wannier function. In the present case, W has only one independent matrix element and we find:

$$w_1 = \frac{1}{3\sqrt{2}} \left\{ \left(\sqrt{3} + 1 + \frac{\sqrt{3}}{2}d \right) (\varphi_1 + \varphi_2) + \left(1 - \sqrt{3}d \right) (\varphi_3 + \varphi_6) - \left(\sqrt{3} - 1 - \frac{\sqrt{3}}{2}d \right) (\varphi_4 + \varphi_5) \right\}, \quad (3.8)$$

which is clearly symmetric (bond-centered). From Eq. 3.7: $\langle |\chi|^4 \rangle = \frac{19}{54} + O(d^2)$, and from Eq. 3.8: $\langle |w|^4 \rangle = \frac{19}{54} + \frac{2\sqrt{3}}{9}d + O(d^3)$. Hence, for $d = 0$, the atom-centered and the bond-centered Wannier functions are *both* maximally localized and symmetric.

Now, the NMTO set, $\chi_o^{(N)}$, is obtained without solving the eigenvalue equations, i.e., it is *not* obtained by projection from the Bloch states through multiplication by $(U_{ko})^{-1}$, but in a more tricky way. We first define a set of downfolded, energy-dependent orbitals,

$$\phi_o(\varepsilon) \equiv \varphi_o 1_{oo} + \varphi_e (\varepsilon 1_{ee} - H_{ee})^{-1} H_{eo}, \quad (3.9)$$

which are localized when ε does not coincide with an eigenvalue of H_{ee} . Projection onto the even sites yields: $\langle \varphi_e | \hat{H} - \varepsilon | \phi_o(\varepsilon) \rangle = 0_{oo}$, so we realize that the functions of the set $\phi_o(\varepsilon)$ are solutions of the impurity problems specified by the boundary conditions that $\phi_o(\varepsilon)$ *vanishes* at the *other* odd sites and is normalized to φ at its own site. Projection onto the odd sites yields:

$$\langle \varphi_o | \hat{H} - \varepsilon | \phi_o(\varepsilon) \rangle = H_{oo} + H_{oe} (\varepsilon 1_{ee} - H_{ee})^{-1} H_{eo} - \varepsilon 1_{oo} \equiv -G_{oo}(\varepsilon)^{-1}, \quad (3.10)$$

and comparison with Eq. 3.3 shows that, if ε is an eigenvalue of the (downfolded) Hamiltonian and u_o an eigenvector, then $\phi_o(\varepsilon) u_o$ is an eigenfunction. $G(\varepsilon)$ defined in Eq. 3.10 is the resolvent. Finally, we need to find an energy-independent, N th-order approximation to the set $\phi_o(\varepsilon)$: We form the set, $\phi_o(\varepsilon) G_{oo}(\varepsilon)$, of (contracted Greens) functions and add an analytical function of energy determined in such a way that the two sets of functions, $\phi_o(\varepsilon) G_{oo}(\varepsilon)$ and $\chi_o^{(N)} G_{oo}(\varepsilon)$, coincide when ε is on an energy mesh, $\varepsilon_0, \dots, \varepsilon_N$, specifying the energy range of interest. By taking the highest-order finite difference on this mesh, one obtains:

$$\chi_o^{(N)} \frac{\Delta^N G_{oo}}{\Delta [0 \dots N]} = \frac{\Delta^N \phi_o G_{oo}}{\Delta [0 \dots N]}, \quad (3.11)$$

which determines the set of (non-orthonormal) NMTOs. For $N = 1$, for instance:

$$\chi_o^{(1)} = [\phi_o(\epsilon_1) G_{oo}(\epsilon_1) - \phi_o(\epsilon_0) G_{oo}(\epsilon_0)] [G_{oo}(\epsilon_1) - G_{oo}(\epsilon_0)]^{-1}. \quad (3.12)$$

For the simple benzene model, Eq. 3.9 yields:

$$\phi_1(\epsilon) = \varphi_1 - \frac{1+d}{\epsilon} \varphi_2 - \frac{1-d}{\epsilon} \varphi_6, \quad (3.13)$$

and $\phi_3(\epsilon)$ and $\phi_5(\epsilon)$ by cyclic permutation of site indices. To order d , the downfolded Hamiltonian Eq. 3.5 is independent of d , and by subtracting ϵ and inverting, we find:

$$G_{oo}(\epsilon) = \frac{\epsilon}{(\epsilon^2 - 1)(\epsilon^2 - 4)} \begin{pmatrix} \epsilon^2 - 3 & 1 & 1 \\ 1 & \epsilon^2 - 3 & 1 \\ 1 & 1 & \epsilon^2 - 3 \end{pmatrix}. \quad (3.14)$$

Specializing to $N = 1$, the NMTO found from Eq. 3.12 is:

$$\chi_1^{(1)} = \varphi_1 - \frac{\epsilon_0 + \epsilon_1}{(\epsilon_0 \epsilon_1 + 4)(\epsilon_0 \epsilon_1 + 1)} \{ [\epsilon_0 \epsilon_1 + 2 + (\epsilon_0 \epsilon_1 + 4)d] \varphi_2 + [\epsilon_0 \epsilon_1 + 2 - (\epsilon_0 \epsilon_1 + 4)d] \varphi_6 - 2\varphi_4 \}, \quad (3.15)$$

and if, with the benefit of hindsight, we choose $\epsilon_0 = -2$ and $\epsilon_1 = -1$, we obtain the exact result Eq. 3.7, apart from the normalization, $1/\sqrt{2}$. With other choices, the NMTO set is an approximation to the exact Hilbert space spanned by χ_o or w_o , as explained in connection with Eq. 3.17 below. Had we chosen $\epsilon_0 = 2$ and $\epsilon_1 = 1$, we would have obtained the Wannier functions for the anti-bonding levels.

By considering a simple TB model, we have thus learned that the NMTO procedure for constructing a minimal basis set, specifically a set of localized Wannier functions, consists of the following steps: 1) Downfolding to a small set of energy-dependent orbitals and 2) a polynomial approximation of the latter. The resulting NMTO set is not orthonormal in general, but may be symmetrically (Löwdin) orthonormalized in a third step. Wannier functions which are maximally localized, and therefore not symmetry breaking, may be obtained in a fourth step. None of these steps require knowledge of the extended (Bloch) eigenstates. Although of utmost importance for applications, steps (3) and (4) are not specific for the NMTO method and fairly standard. As a consequence, they will not be considered further in this chapter.

3.2.2 NMTOs for Real Systems

For real systems, the NMTO method constructs a set of atom-centered local-orbital basis functions which span the solutions of the one-electron Schrödinger equation for a local potential, written as a superposition,

$\sum_R v_R(|\mathbf{r} - \mathbf{R}|)$, of spherically symmetric, short-ranged potential wells, a so-called overlapping muffin-tin potential. This is done by first solving the radial Schrödinger (or Dirac) equations numerically to find $\varphi_{Rl}(\varepsilon, |\mathbf{r} - \mathbf{R}|)$ for all angular momenta, l , with non-vanishing phase-shifts, for all potential wells, R , and for the chosen set of energies, $\varepsilon = \varepsilon_0, \dots, \varepsilon_N$.

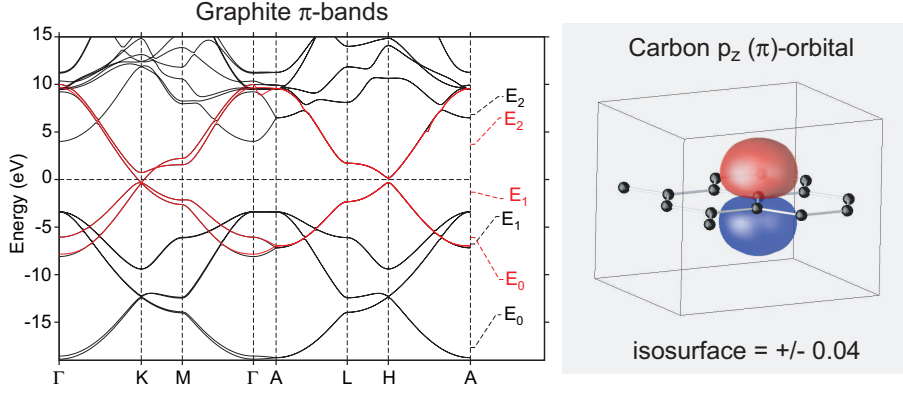


Figure 3.1: The band structure of graphite calculated with a full spd basis is given in black. The red bands have been calculated with a p_z NMTO (shown on the right) on every carbon atom. This corresponds to a π non-bonding basis set. The energy meshes used for each calculation are given to the right of the band structure. In all figures, red denotes a positive and blue a negative isosurface value. For the orbital plots, the isosurface values are given in units of $a_B^{-3/2}$, where a_B is the Bohr radius.

The partial-wave channels, Rlm , are partitioned into *active* (odd, in the benzene example) and *passive* (even). The active ones are those for which one wants to have orbitals in the basis set. For example, the active channels are p_z on all the carbon atoms for the red π -bands in Fig. 3.1, whereas for the black bands, the active channels include all nine s , p , and d -channels on all the carbon atoms.

For each active channel, $\bar{R}\bar{l}\bar{m}$, a *kinked* partial wave, $\phi_{\bar{R}\bar{l}\bar{m}}(\varepsilon, \mathbf{r})$ (Eq. 3.9 in TB theory), is now constructed from *all* the partial waves, $\varphi_{Rl}(\varepsilon, |\mathbf{r} - \mathbf{R}|) Y_{lm}(\widehat{\mathbf{r} - \mathbf{R}})$, inside the potential-spheres, and from *one* solution, $\psi_{\bar{R}\bar{l}\bar{m}}(\varepsilon, \mathbf{r})$, of the wave-equation in the interstitial, a so-called screened spherical wave. The construction is such that the kinked partial wave is a solution of Schrödinger's equation at energy ε in all space, except at some hard screening-spheres –which are concentric with the potential-spheres, but have no overlap– where it is allowed to have radial *kinks* in the *active* channels. In passive channels, the matching is smooth.

It is now clear that if we can form a linear combination of such kinked partial waves with the property that all kinks cancel, we have found a solution of Schrödinger's equation with energy ε . In fact, this kink-cancellation condition (Eqs. 3.10 and 3.3 in TB theory) leads to the classical

method of Korringa, Kohn, and Rostoker^{35,36} (KKR), but in a screened representation and valid for overlapping MT potentials to leading order in the potential overlap.

Whereas the screened spherical wave must join *smoothly* onto all *passive* partial waves, we can require that it *vanishes* at the hard spheres for all the *active* channels except the eigenchannel. This confinement is what makes the screened spherical wave *localized*, provided that localized solutions exist for the actual potential, energy, hard spheres, and chosen partition into active and passive channels. Since the screened spherical wave is required to vanish merely in the *other* active channels, but not in the eigenchannel, it is an impurity solution for the hard-sphere solid and is given by Eq. 3.9 in TB theory.

Finally, the set of NMTOs is formed as a superposition of the kinked-partial-wave sets for the energies, $\epsilon_1, \dots, \epsilon_N$:

$$\chi_{\mathbf{R}l\mathbf{m}}^{(N)}(\mathbf{r}) = \sum_{n=0}^N \sum_{\bar{R}\bar{l}\bar{m}} \phi_{\bar{R}\bar{l}\bar{m}}(\epsilon_n, \mathbf{r}) L_{n; \bar{R}\bar{l}\bar{m}, \mathbf{R}l\mathbf{m}}^{(N)}. \quad (3.16)$$

Note that the size of this NMTO basis set is given by the number of active channels and is independent of the number, $N + 1$, of energy points. The coefficient matrices, $L_n^{(N)}$, in Eq. 3.16 are determined by the condition that the set of NMTOs span the solutions, $\Psi_i(\epsilon_i, \mathbf{r})$, of Schrödinger's equation with an error

$$\begin{aligned} \Psi_i^{(N)}(\mathbf{r}) - \Psi_i(\epsilon_i, \mathbf{r}) &= c^{(N)}(\epsilon_i - \epsilon_0)(\epsilon_i - \epsilon_1) \dots (\epsilon_i - \epsilon_N) \\ &+ o((\epsilon_i - \epsilon_0)(\epsilon_i - \epsilon_1) \dots (\epsilon_i - \epsilon_N)). \end{aligned} \quad (3.17)$$

This condition leads to Eq. 3.11 and the NMTO set is a polynomial approximation for the Hilbert space of Schrödinger solutions, with $L_n^{(N)}$ being the coefficients in the corresponding Lagrange interpolation formula. Eq. 3.12 is for $N=1$. An NMTO with $N=0$ is a kinked partial wave, but an NMTO with $N > 0$ has no kinks, but merely discontinuities in the $(2N + 1)^{st}$ radial derivatives at the hard spheres for the active channels. The prefactor, $c^{(N)}$, in Eq. 3.17 is related to this,²⁵ and it decreases with the size of the set, ie. with the number of active channels.

A basis set which contains as many orbitals as there are bands to be described, we shall call *truly minimal*. For an isolated set of bands, the truly minimal NMTO basis converges to the exact Hilbert space as the energy mesh which spans the range of the bands becomes finer and finer. Symmetrical orthonormalization of the converged NMTO set therefore yields a set of atom-centered Wannier functions which are localized by construction. The localization depends on the system *and* on the choice of downfolding. Had we, for instance for benzene, chosen instead of the odd sites, sites 1, 2 and 3 as active, the corresponding NMTO Wannier functions would have been less localized, the Hilbert space spanned by them would have needed a larger N for convergence, and the construction from this set of the maximally localized Wannier functions would have required a larger cluster. Nevertheless, the calculation could have been

done. Similarly, in real systems the choice of active channels and their hard-sphere radii –their number and main characters being fixed by the nature of the band to be described– influences the properties of the individual *N*MTOs, but not the Hilbert space they converge to.

3.3 Computational Methods

Graphite has a hexagonal unit cell. The space group is $P6_3/mmc$ (194) and the two basis carbon atoms are located in the 2b and 2c Wyckoff positions. The lattice constants, a and c were taken from experimental data³⁷ as being 2.4642 Å and 6.7114 Å, respectively. In addition to the atoms on the two crystallographic positions, it was necessary to insert two interstitial spheres to represent the potential in the calculation. Boron nitride is also found with space group $P6_3/mmc$ (194), with the boron atom located in the 2c and the nitrogen atom in the 2d Wyckoff positions. The lattice constants, a and c were taken from experimental data³⁸ as being 2.50399 Å and 6.6612 Å, respectively. It was only necessary to insert one interstitial sphere.

All of the TB-LMTO calculations³⁹ were performed using the Vosko-Wilk-Nusair (VWN) LDA⁴⁰ along with the Perdew-Wang GGA.⁴¹ Scalar relativistic effects were included. For graphite and boron nitride a basis set consisting of spd LMTOs on the carbon, boron and nitrogen atoms with sp LMTOs on the empty spheres, was used. The calculations utilized 1953 irreducible points in the tetrahedron k -space integrations.⁴²

The present version of the *N*MTO program is not self-consistent and requires the output of the self-consistent potential from the TB-LMTO program. The downfolded band structures are compared with bands computed employing a full *N*MTO basis set; *not* with those obtained using the TB-LMTO program. In all cases, the default values for the hard-sphere radii, a_R , were used. Thus, all of the hard spheres were slightly smaller than touching. However in general, the a_R should be taken as 0.9 times the tabulated covalent, atomic or ionic radii. In the calculations all partial-waves on the empty spheres were downfolded. The other downfolding schemes and energy meshes employed for particular calculations are given in the results and discussion section of the chapter. More details about the *N*MTO formalism can be found in Refs. 17, 26, 27 and references within.

3.4 Results and Discussion

3.4.1 Graphite: A Semi-Metal

The bonding in graphite is understood: within a single graphene sheet the s , p_x and p_y orbitals on the two carbon atoms per primitive cell hybridize to form a set of sp^2 σ -bonding bands which are occupied, and a set of σ -anti-bonding bands which are empty. There are two sheets

per cell.

The p_z orbitals form a group of bonding and anti-bonding π -bands which just touch at the Fermi level, making graphite a semi-metal. In order to describe the set of π -bands, we would need to construct two equivalent N MTOs per sheet, each centered on a single carbon atom. We leave it to the method to shape the orbitals, subject to the aforementioned boundary conditions for the screened spherical waves. The energy mesh must be chosen in such a way so that it spans the energy range of the π -bands and excludes the energy range where the π -bands hybridize with other bands.

In Fig. 3.1 the band structure of graphite calculated with a full spd basis set on each carbon atom is given in black. It is in excellent agreement with previous calculations.⁴³ The red bands have been calculated with a basis set comprised of a p_z non-bonding N MTO on every carbon. The energy meshes used for both calculations are given to the right of the band structures. The two sets of bands are almost identical, on the scale of the figure, with the exception of a small bump at the top of the red bands, where hybridization with other bands occurs. Thus, it is possible to describe the set of occupied and unoccupied π -bands in graphite via just one orbital on every carbon atom, shown to the right of the band structure. The orbital is localized because it is not allowed to have p_z character on any of the other carbons. It *is* allowed to have other orbital characters, (e.g. s, p_x, d_{xy}), on the other symmetry-equivalent carbons, but such characters are hardly visible in the figure.

It is even possible to generate orbitals for just the occupied or unoccupied π -bands in graphite. In this case we only want to pick half of the bands, and therefore we need a basis with, say, a p_z orbital on *every second* carbon atom with all other partial waves being *down-folded*, ie. passive. Moreover, an energy mesh spanning the bonding (anti-bonding) bands must be used in order to obtain the bonding (anti-bonding) π -orbital for graphite. Thus, the choice of the energy mesh determines which set, bonding or anti-bonding, is chosen. In Figs. 3.2 and 3.3 the orbital on the central carbon atom is shown, along with the band structures computed with a full spd basis (in black) and those with the *truly minimal* basis set we have just specified (in red). The agreement between the two sets of bands is excellent, with only minor deviations in the upper regions of the downfolded band structure of the anti-bonding bands where hybridization with the next higher bands occurs. Inspection of the π -bonding and anti-bonding orbitals shows that they spread out onto the first nearest neighbour carbon atoms (passive), but they are confined not to have any p_z character on those carbon atoms, e.g. the second nearest neighbours, where the basis set has orbitals (active partial waves). The third nearest neighbour atoms also have all partial waves downfolded and some p_z character may be seen. Clearly, this choice of orbitals breaks the symmetry; the same Hilbert space would have been obtained had the orbitals been placed on the other half of the carbon atoms.

It is also possible to describe the sp^2 -bonding bands in graphite by placing an s, p_x and p_y

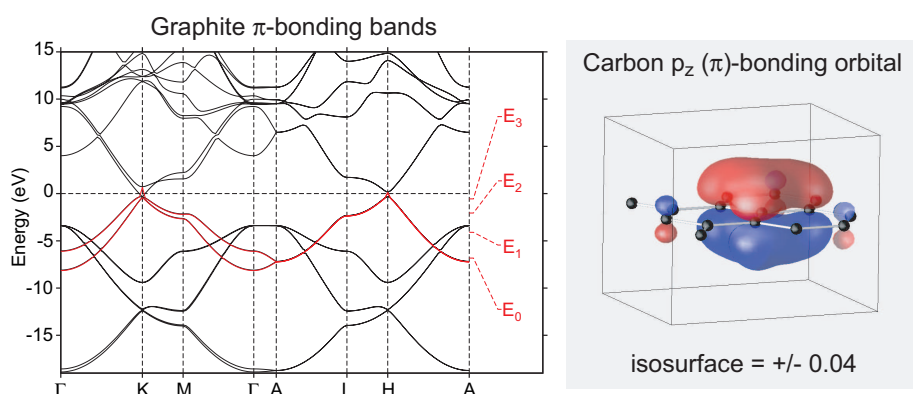


Figure 3.2: As in the previous figure, but the red bands have now been calculated with a p_z N MTO (shown on the right) on *every second* atom within a single graphene sheet. The energy mesh is chosen within the occupied part of the π -band, which is therefore selected. We shall refer to this as a π -bonding basis.

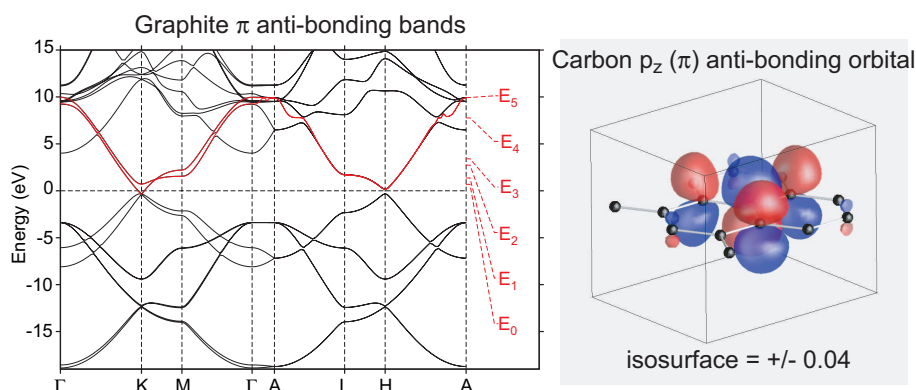


Figure 3.3: As in the previous figure, but the energy mesh is now in the *empty* part of the π -band. We shall refer to this as a π^* anti-bonding basis.

orbital on *every second* carbon atom, downfolding all other channels and using an energy mesh which spans the energy range of the bands of interest. The band structure obtained with this basis is given in red in Fig. 3.4 and is identical, on the scale of the figure, to the black bands which have been calculated using a full sp^2 basis set on every carbon atom. The orbitals may spread out onto the nearest neighbour carbons, however are confined not to have any s , p_x or p_y character on the second nearest neighbours. Symmetrical orthonormalization of these three orbitals gives the well known bond orbital, the carbon sp^2 N MTO, also shown in the figure.

The above examples show that it is possible to describe a chosen band, or set of bands, with a truly minimal basis set consisting of one N MTO per band. Moreover, the N MTOs obtained

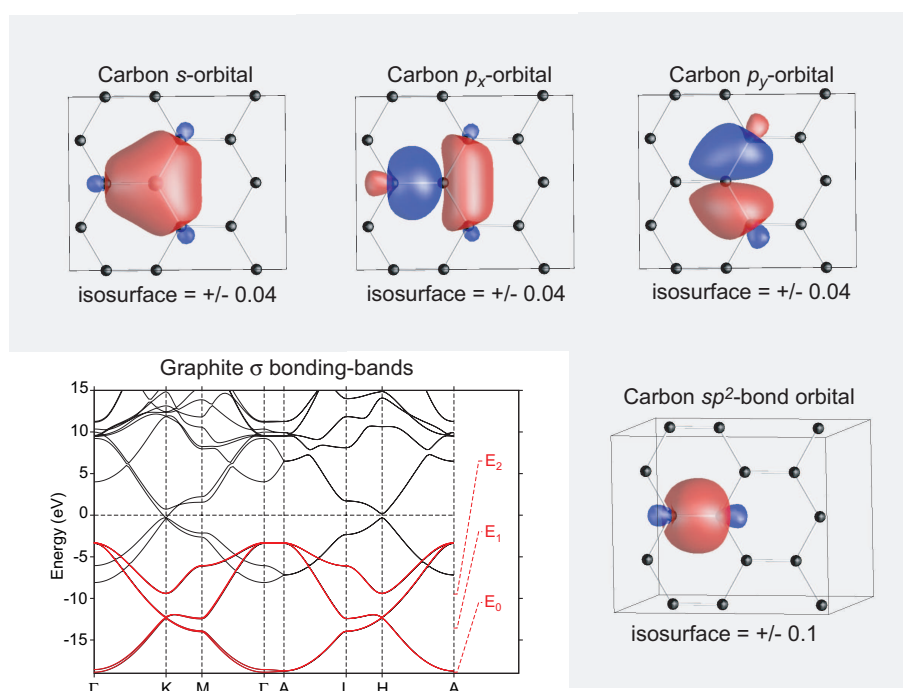


Figure 3.4: As in the previous figures, but the red bands have now been calculated with a σ -bonding basis comprised of an s , p_x and p_y NMTO on *every second* carbon atom (shown above the band structure). Also shown is one of the three congruent sp^2 -bond orbitals which arise by symmetrical orthonormalization of the s , p_x and p_y orbitals.

from our method are in-line with an intuitive chemical picture of bonding in the solid state, except that they may break the symmetry. This arbitrariness originating in the constraint that the NMTOs be atom-centered can be removed by forming linear combinations to maximally localize the Wannier functions. Hence, NMTOs should be useful not only, for example, as basis sets in linear scaling methods, but also in gaining a chemical understanding of periodic systems.

3.4.2 Boron Nitride: An Insulator

The bonding in boron nitride is similar to that in graphite: within a single layer the s , p_x and p_y boron and nitrogen orbitals hybridize to form sp^2 σ -bonding and anti-bonding bands. The alternation, however, makes the system insulating with a band gap between the bonding and anti-bonding π -bands. In order to describe the occupied bands, it is possible to generate either boron or nitrogen centered NMTOs. It can be expected that the electron density, and hence the orbital at a given isosurface, should have a maximum closer to the more electronegative

element, nitrogen. The method needs to do less ‘work’ if the orbitals are placed initially where the electrons are thought to be. Thus, we first place all of the orbitals on nitrogen, and let the method shape them accordingly. This choice of atom-centered orbitals corresponds to the extreme ionic limit, a $B^{3+}N^{3-}$ configuration. The bonding σ and π -bands and their respective *N*MTOs are shown in the top and bottom part of Fig. 3.5, respectively. The s , p_x and p_y *N*MTOs are not shown, since they are very similar to those obtained for graphite. The full band structure is in excellent agreement with previous calculations.⁴⁴

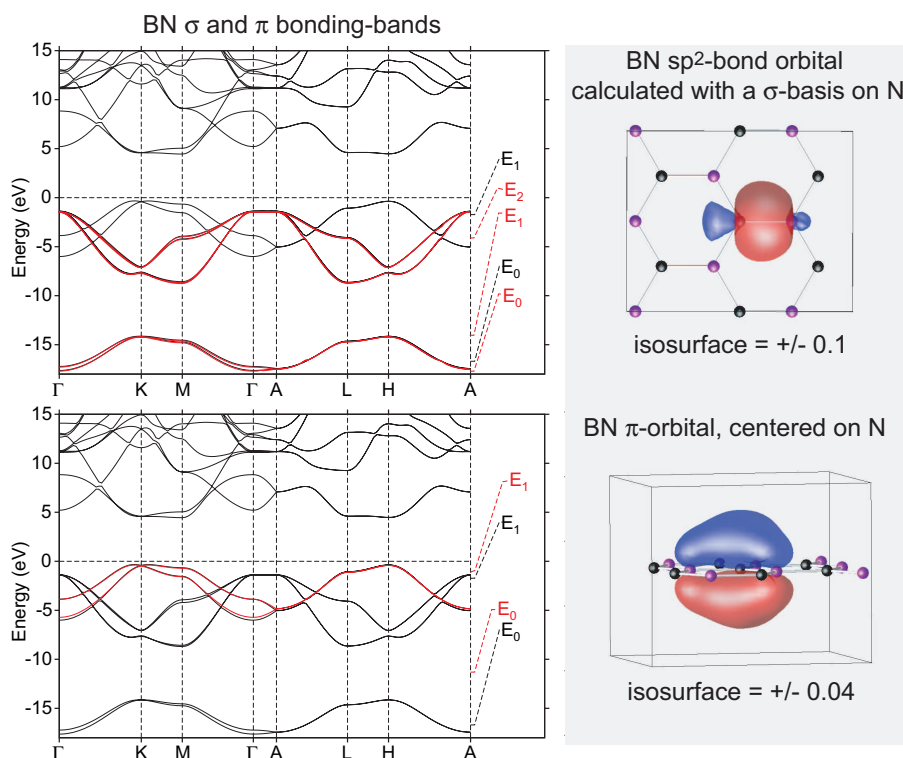


Figure 3.5: The band structure of boron nitride calculated with a full *spd* basis is given in black. The red bands in the upper panel have been calculated with a σ -bonding basis composed of an s , p_x and p_y *N*MTO on all nitrogen atoms. The red bands in the bottom panel have been calculated with a π -bonding basis composed of a p_z orbital on all nitrogen atoms. Also given is one of the three equivalent sp^2 -bond orbitals and the p_z *N*MTO. Boron atoms are purple, nitrogen black.

In new materials where the bonding is not well understood, it may be difficult to decide where the orbitals should be placed. In the following we will show that *N*MTOs are forgiving: even a bad starting guess can yield the correct bands and Hilbert space. Placing all the orbitals on the boron atoms (a $B^{5-}N^{5+}$ configuration) yields the bands and orbitals shown in Fig. 3.6.

The sp^2 -bond orbital looks identical to the one shown in Fig. 3.5, as it should be when the energy mesh is converged. For the π -bands, more energy points are necessary since the orbital has to spread out from a central boron onto three neighbouring nitrogens. Inspection of the boron (nitrogen) centered π -NMTOs makes it plausible that when squared and summed over all boron (nitrogen) sites, they give the same electron density, with maxima shifted towards nitrogen.

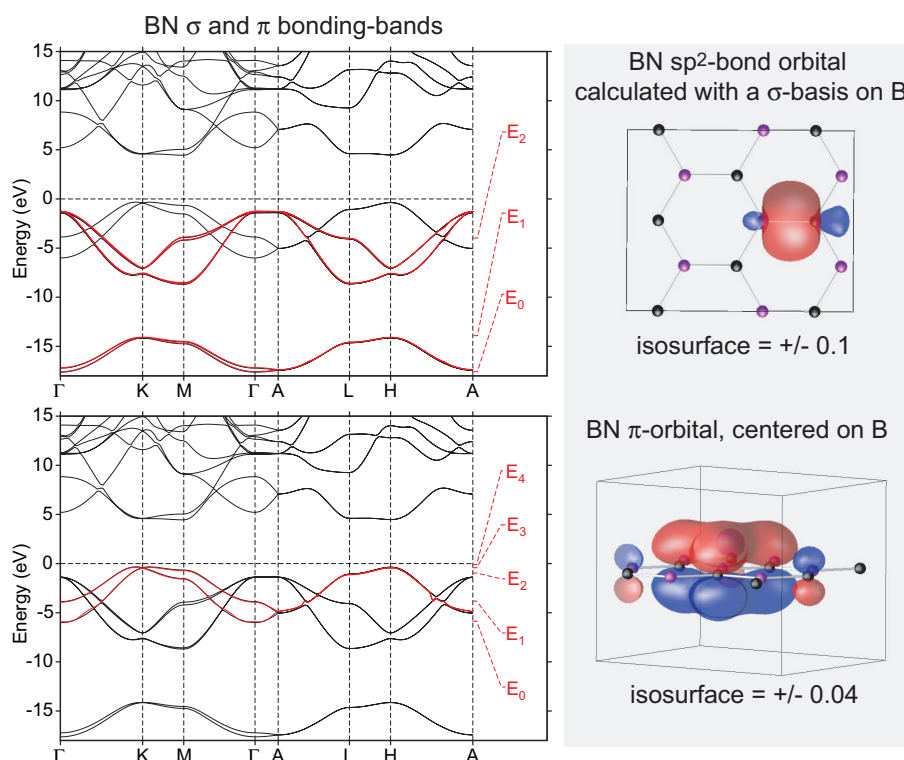


Figure 3.6: As in the previous figure, but with boron-centered σ and π basis sets.

3.5 Summary and Conclusions

Within this chapter we have shown that the 3rd generation MTO method can be used to design a basis set of atom-centered localized orbitals, which span the wave functions in a given energy range. For an isolated set of bands, arbitrary accuracy may be obtained, with only one basis function per electron pair (or single electron, in the case of spin-polarized calculations), simply by increasing the density of the energy mesh which spans the energy range of the band in question. This method may be applied to insulating and even semi-metallic systems to generate Wannier-like functions which are in-line with a chemical understanding of bonding in the solid-

state. It should therefore be a useful analysis tool in, for example, explaining experimental trends for a given set of compounds via orbital based arguments; clarifying the bonding in novel or even amorphous materials; visualizing pressure-driven electronic transitions.

3rd generation MTOs may also be useful in generating *truly minimal* basis sets for order-*N* methods and in constructing many-electron wave functions which can be applied to study strongly correlated systems realistically. In our implementation, *N*MTOs are generated using the self-consistent potential from an LMTO calculation. However, our method may be interfaced with the results of any other program, provided that the potential can be expressed in terms of a superposition of spherically symmetric potential wells with radial overlaps of up to ~60 percent.

Chapter 4

Theoretical Studies of High Pressure Cesium

4.1 Introduction

Under pressure, cesium undergoes a variety of interesting structural phase transitions. At 2.3 GPa Cs-I (bcc cesium) transforms to an fcc phase.⁴⁵ Until recently, it was believed that Cs-II undergoes an isostructural transition to Cs-III (which is found in a very narrow pressure range between ~ 4.2 and ~ 4.3 GPa). However, experiments have shown that Cs-III has a very complicated structure which is orthorhombic (space group $C222_1$ with 84 atoms per unit cell).⁴⁶ At ~ 4.3 GPa Cs-III transforms to the non-close-packed tetragonal Cs-IV⁴⁷ which undergoes a transition to orthorhombic Cs-V⁴⁸ at ~ 12 GPa and finally to the double hexagonal close packed Cs-VI at ~ 70 GPa.⁴⁹ It is also remarkable that when cesium is compressed to about 26% of its normal volume, in the vicinity of the Cs-IV \rightarrow Cs-V transition, it becomes superconducting.⁵⁰ The aforementioned structures are shown in Fig. 4.1. In contrast to the conventional picture that increasing pressure yields closer packed structures, the nearest neighbour coordination number first increases from 8 (bcc) to 12 (fcc), then decreases to about 10 (Cs-III), 8 (Cs-IV) and finally increases again to 10/11 (Cs-V) and 12 (Cs-VI). These structural transitions are believed to be driven by the pressure-induced $s \rightarrow d$ valence electronic transition which causes the interatomic distances to become smaller compared to the ranges of the wavefunction.⁵¹

Many theoretical investigations on cesium have been performed. Full potential linear muffin tin orbital (FP-LMTO) calculations have reproduced the observed crystal structure sequence fcc \rightarrow Cs-IV \rightarrow Cs-V \rightarrow Cs-VI.⁵⁴ Due to the fact that Cs-V and Si-VI have the same space group and nearly identical axial ratios and axial coordinates, the bonding within these two systems was compared. While Si-VI was determined to be nearly free-electron-like, Cs-V was found to exhibit multi-center d -electron bonding.⁵³ Near the Cs-IV to Cs-V transition the d orbital occupation was calculated as being approximately 0.8.⁵⁵⁻⁵⁷ For Cs-VI it was found that the

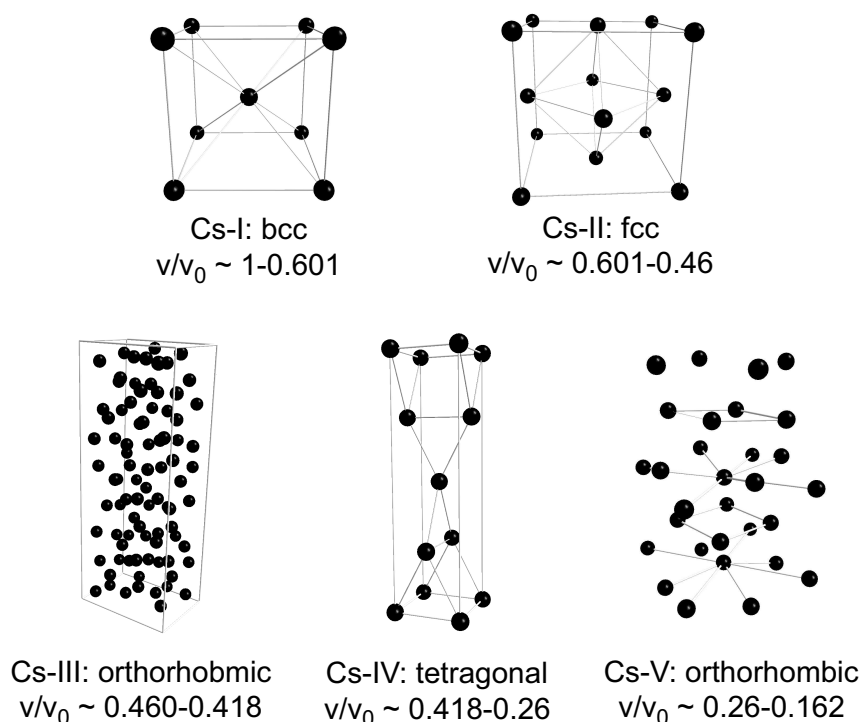


Figure 4.1: The unit cells of Cs-I, Cs-II, Cs-III, Cs-IV and Cs-V along with the relative volume range within which each structure is found.^{47, 52, 53}

$s \rightarrow d$ electronic transition is already complete and core-core repulsion as well as $p - d$ hybridization with the semicore $5p$ states become important.^{49, 57} Before the recent determination of the structure of Cs-III,⁴⁶ *ab initio* calculations indicated that an isostructural transition is not possible.^{58, 59} In particular, it was speculated that fcc Cs-III would become unstable against a soft phonon which could result in a superstructure prior to the transition to Cs-IV.⁶⁰

The recent determination of the crystal structure of Cs-III⁴⁶ has sparked new theoretical work in this field. FP-LMTO calculations have confirmed the experimental results, and the calculated transition pressures for $\text{fcc} \rightarrow \text{Cs-III} \rightarrow \text{Cs-IV}$ were determined to be in very good agreement with experiment.⁶¹ Moreover, it was postulated that a d -orbital occupation of about 0.52 electrons is necessary in order for the Cs-III structure to be stable. A mechanism describing the displacement of atoms leading to the formation of Cs-III from Cs-II was proposed.⁶² It was also indicated that the participation of the d electrons in bonding modifies the shape of the electronic shells, which become nonspherical and that the packing of such ellipsoidal atomic shells is 5-8% closer than the corresponding packing of hard spheres in Cs-IV. Calculations of the electron density and the electron localization function (ELF) for different structures have been performed.⁶³ For Cs-II, it was found that at low density the electrons are localized around the atomic positions, whereas for high density they are more localized in the interstitial sites.

Thus, the “covalent bond” was postulated to be between second nearest neighbour cesiums with the “bonding electrons” localized on a 2D plane forming a square net. It was pointed out that the electron density of Cs-IV can be reconstructed from that of Cs-II by periodic displacements of the 2D square nets.

Within this chapter we will first of all use a simple argument to illustrate why the bottom of the d bands in cesium are lowered and the bottom of the s bands are raised in energy with increasing pressure. Next, we analyze the band structures of Cs-I, Cs-II and Cs-IV at different volumes. We will in particular focus on how the band structure changes near the experimentally established volume of a structural phase transition. The phonon spectra and electron phonon coupling for fcc Cs at different v/v_0 will be given. Next, we will show that it is possible to obtain Wannier-like functions for only the occupied states in a metallic system by calculating NMTOs for Cs-I, Cs-II, Cs-II under pressure and Cs-IV. Finally, we will analyze the bonding in Cs-IV and provide an explanation for the stability of this structure.

4.2 Computational Details

Computations were performed on Cs-I (bcc), Cs-II (fcc) and Cs-IV, which has the space group $I4_1/amd$ with 2 atoms per unit cell.⁴⁷ The experimental lattice parameter of 6.048 \AA ⁶⁴ for cesium at ambient conditions was used. Both Cs-I and Cs-II are close-packed so it was not necessary to insert any interstitial spheres. However, four such spheres were needed to represent the charge density in Cs-IV. All of the TB-LMTO calculations³⁹ were performed using the Vosko-Wilk-Nusair (VWN) local density approximation (LDA)⁴⁰ along with the Perdew-Wang generalized gradient approximation (GGA).⁴¹ Scalar relativistic effects were included and the basis consisted of sd LMTOs with pf LMTOs being downfolded. The calculations utilized 1661 and 897 irreducible points in the tetrahedron k -space integrations⁴² for cesium in the bcc and fcc structures with one atom per unit cell, respectively, and 693 points were used in the calculation for Cs-IV.

The downfolded band structures are compared with those computed employing a full NMTO basis set. In all cases, the default values for the hard-sphere radii, a_R , were used. The downfolding schemes and energy meshes employed for particular calculations are given in the results and discussion section of the chapter.

The phonon spectrum and electron phonon coupling of fcc Cs were obtained from linear response calculations as implemented in Savrasov’s FP-LMTO code.^{18,19} Following the computations performed by Kong *et al.*,⁶⁰ we have employed the VWN exchange-correlation potential⁴⁰ along with the GGA-96⁶⁵ correction. The dynamical matrix for fcc Cs was calculated for a set of irreducible q -points in an (8,8,8) reciprocal-lattice grid. A 3κ -spd LMTO basis set was used and the one-center expansions inside the non-overlapping muffin-tin spheres were

performed up to $l_{max} = 6$. The s , p and d basis functions were expanded in plane waves in the interstitial region. The $5s$ semicore states were treated as valence states in a separate energy window. The induced screened potentials and charge densities were represented inside the muffin tin spheres by spherical harmonics up to $l_{max} = 6$ and by plane waves with a cut-off ranging from 142.0 Ry. for $v/v_0 = 0.47$ to 158.1 Ry for $v/v_0 = 0.40$ (9984 plane waves) in the interstitial region. The k -space integration was performed over a (16,16,16) grid, however the integration weights were calculated from a (32,32,32) grid, resulting in a more accurate representation of the Fermi surface using a smaller number of k -points. The phonon spectra along the high symmetry lines were calculated in a denser q -mesh fitting with the (16,16,16) k -grid.

4.3 Results and Discussion

4.3.1 Energy Bands of Cesium Under Pressure

Within this section we will show that for an elemental solid within the atomic spheres approximation (ASA), increasing pressure raises and lowers the energy of a free and tunneling electron, respectively, at the bottom of a band. Moreover, increasing pressure always raises the energy of an electron at the top of a band. In the specific case of cesium, the free electrons are the s and the tunneling electrons are the d . This gives a simple explanation for the $s \rightarrow d$ valence electronic transition for cesium under pressure.

Neglecting the zero-point motion of the nuclei the pressure, $P(V)$, for a volume V , is given as the change of the total energy with uniform compression as

$$P(V) = -dE_{tot}/dV. \quad (4.1)$$

From this, the equilibrium atomic volume V_0 , may be estimated via

$$P(V_0) = 0. \quad (4.2)$$

It can be shown that for an elemental solid in the ASA, the pressure can be calculated by the following equivalent expressions⁶

$$3PV \equiv -dE_{tot}/d \ln s = - \sum_j^{occ} \delta E_j / \delta \ln s, \quad (4.3)$$

$$3PV = - \sum_l \int^{E_F} [\delta E_l / \delta \ln s] N_l(E) dE \equiv \sum_l 3P_l V. \quad (4.4)$$

In the above, s is the atomic sphere radius, E_j are the one electron energies, l is the angular momentum and N_l the density of states.

If v is the value of the potential at some radius r and $v_l \equiv v + l(l + 1)r^{-2}$ is the potential including the centrifugal term, then the radial wave function as given by the radial Schrödinger equation can be written as

$$-[r\varphi_l(E, r)]'' = [E - v(r) - l(l + 1)r^{-2}]r\varphi_l(E, r) \equiv [E - v_l(r)]r\varphi_l(E, r). \quad (4.5)$$

In order to evaluate the pressure, the potential should be frozen and only the atomic sphere radius should change. Thus, the radial Schrödinger equation (4.5) remains unchanged and only the radius s at which the boundary condition, $D_l(E, s) \equiv s\varphi_l'(s)/\varphi_l(s)$, is implemented varies.

The radial Schrödinger equation can be rewritten as a first order differential equation for $D_l(E, s)$ and therefore for the energy, $E_l(D_l, s)$,⁶ as in the following

$$-\partial E_l(D_l, s)/\partial \ln s = [D_l(D_l + 1) + (E - v_l)s^2]s\varphi_l(E, s)^2. \quad (4.6)$$

For a bonding electron at the bottom of the band, $D_l = 0$, and therefore the sign of the partial pressure is dependent only upon the value of $(E - v_l)$. A free electron which is classically allowed to leave the atomic sphere has $(E - v_l) > 0$ and from Eqs. 4.6 and 4.4 we see that the pressure is positive (repulsive). An electron which can only escape the atomic sphere by tunneling has $(E - v_l) < 0$ and therefore yields a negative (attractive) pressure. Examination of Eq. 4.5 reveals that $\varphi_l(E, s)$ has a negative curvature for a free electron and a positive curvature for a tunneling one. This is illustrated in Fig. 4.2. Since φ_l'/φ_l is a decreasing function of

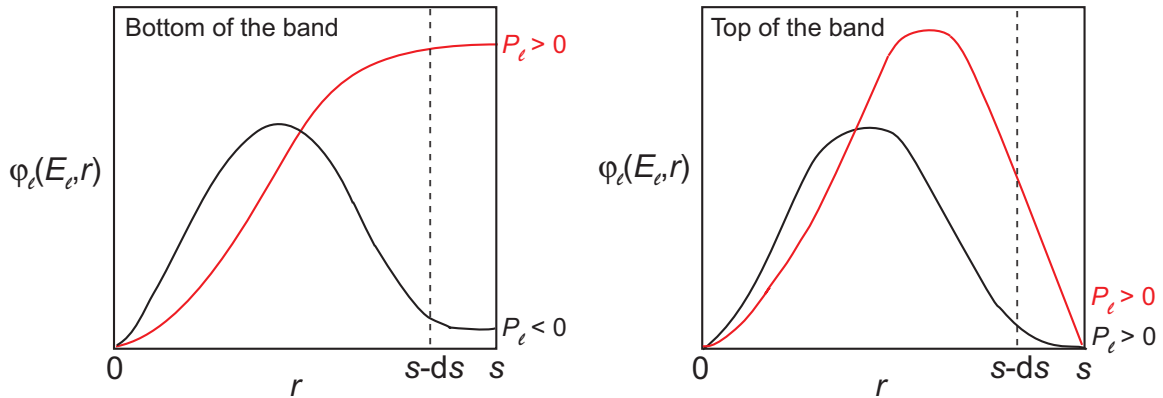


Figure 4.2: The radial wavefunctions, φ_l , at the bottom and top of the band. The red lines are for the free, and the black lines for the tunneling electrons. The sign of the partial pressure is indicated on the right.

energy, increasing pressure raises the energy of the free electrons and lowers the energy of the tunneling ones at the bottom of the band. Inspection of the figure indicates that under compression $\varphi_l(E, s)$ must be raised and lowered for a free and tunneling electron, respectively, in order to restore the bonding condition $\varphi_l' = 0$.

For an anti-bonding electron at the top of the band D_l diverges. Therefore $(E - v_l)$ in Eq. 4.6 may be ignored and $D_l(D_l + 1)$ always yields a positive term. Thus, irrespective of whether we consider a free or a tunneling electron, the pressure is always positive. This behaviour is also shown in Fig. 4.2 and closer inspection indicates that in order to restore the boundary condition $\varphi_l(E, s) = 0$ under compression, φ'_l must become more negative. Once again, since φ'_l/φ_l is a decreasing function of energy, the pressure always raises the energy of an electron at the top of the band.

The above argument shows that for cesium the bottom of the band for the free s and tunneling d electrons increase and decrease in energy, respectively, with increasing pressure. Thus, for sufficiently small volumes the bottom of the d band falls below the bottom of the s band and starts to become populated. Upon increasing pressure, the electronic $s \rightarrow d$ transition progresses further until cesium basically becomes a d^1 metal. Smaller volumes even lead to $d - p$ hybridization with the $5p$ semicore states.

4.3.2 Band Structure of Cesium

In Fig. 4.3 the TB-LMTO band structure of bcc Cs at ambient volume is decorated with eigenvectors in an orthogonal representation (fat bands). Despite the fact that the occupied bands are primarily s -like, some t_{2g} and d_{z^2} character is found below the Fermi level near the N -point. Upon increasing pressure, the energy of the e_g bands is lowered and around $v/v_0 = 0.6$ they cross the Fermi level around the H -point, causing a change in the topology of the Fermi surface (Lifshitz transition). It is interesting to note that it is exactly at this volume that the transformation between Cs-I and Cs-II is found to occur experimentally.

In Fig. 4.4 the TB-LMTO fat bands for fcc Cs at $v/v_0 = 0.6$ are shown. Around the L -point the occupied band still has primarily s -character, however some degree of hybridization with the t_{2g} bands is also apparent. Around the X -point, the band under the Fermi level is mostly e_g -like, with a small amount of s -character. The $s \rightarrow d$ electronic transition is evident, and comparison with Cs-I shows that a greater amount of the occupied bands have d -character. The transition from Cs-II to Cs-III occurs around $v/v_0 = 0.46$, whereas around $v/v_0 = 0.43$ the LMTO bands show two Lifshitz transitions, with the e_g bands touching the Fermi level near the X -point and another set of bands crossing it near the K -point. It should be noted that the Lifshitz transition was calculated to occur around $v/v_0 = 0.46/0.47$ with FP-LMTO, which is inherently more accurate than LMTO. In the next section we will further examine the conjecture that the structural transition from Cs-II to Cs-III is a result of this Lifshitz transition.

The unit cell of Cs-III contains 84 atoms, with 11 different atom types. Since the band structure is quite complicated, an analysis of the fat bands does not reveal easily understandable information and will not be attempted here.

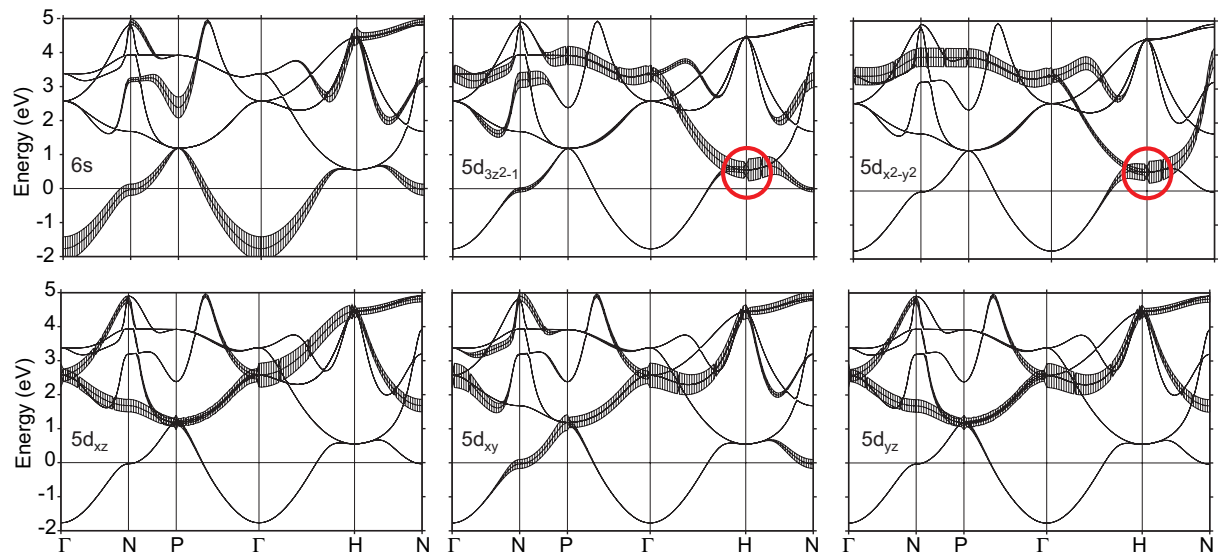


Figure 4.3: Energy bands of bcc Cs at $v/v_0 = 1$ with orthogonal LMTO characters (fat bands). Around $v/v_0 = 0.6$, the e_g bands, circled in red, cross the Fermi level near the H -point.

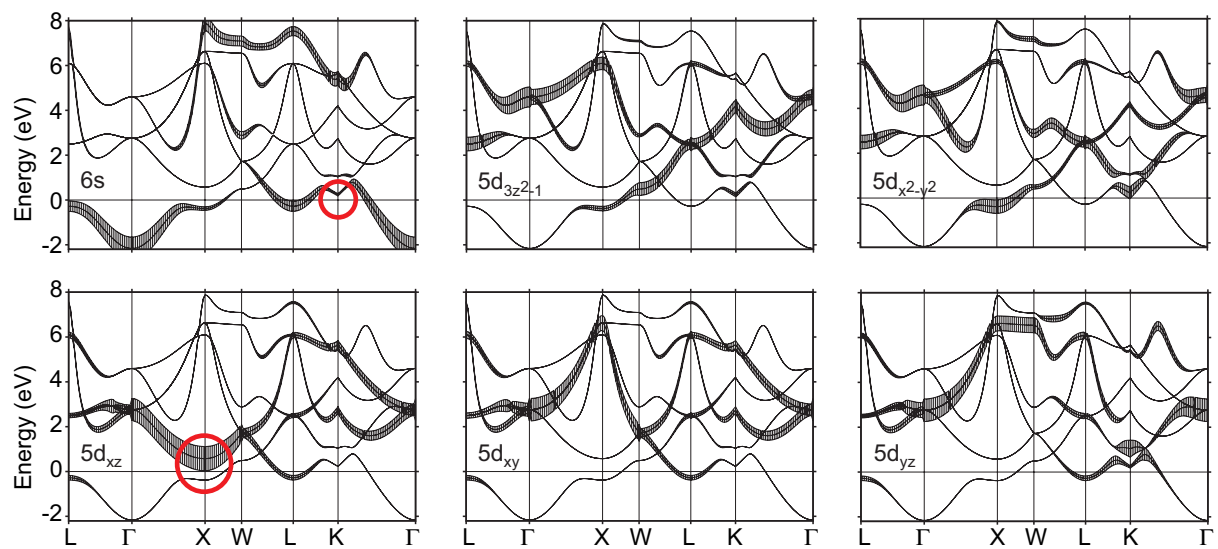


Figure 4.4: Energy bands of fcc Cs at $v/v_0 = 0.6$ with orthogonal LMTO characters (fat bands). Around $v/v_0 = 0.43$, the t_{2g} bands, circled in red, cross the Fermi level near the X -point and another band, also circled in red, crosses the Fermi level near the K -point.

In Fig. 4.5 the TB-LMTO fat bands for Cs-IV at $v/v_0 = 0.4$ are shown. Here, the $s \rightarrow d$ transition is evident and the occupied bands display a large amount of t_{2g} character. We will analyze this band structure and the stability of Cs-IV in a latter section. Upon increasing pressure a few Lifshitz transitions occur. At $v/v_0 = 0.3$ the xz/yz band, circled in red in Fig. 4.5 crosses the Fermi level between the N and P points. Then at around $v/v_0 = 0.25$, another xz/yz band dips below, and the lower s band rises above, the Fermi level between the P and Γ and Γ and Z points, respectively.

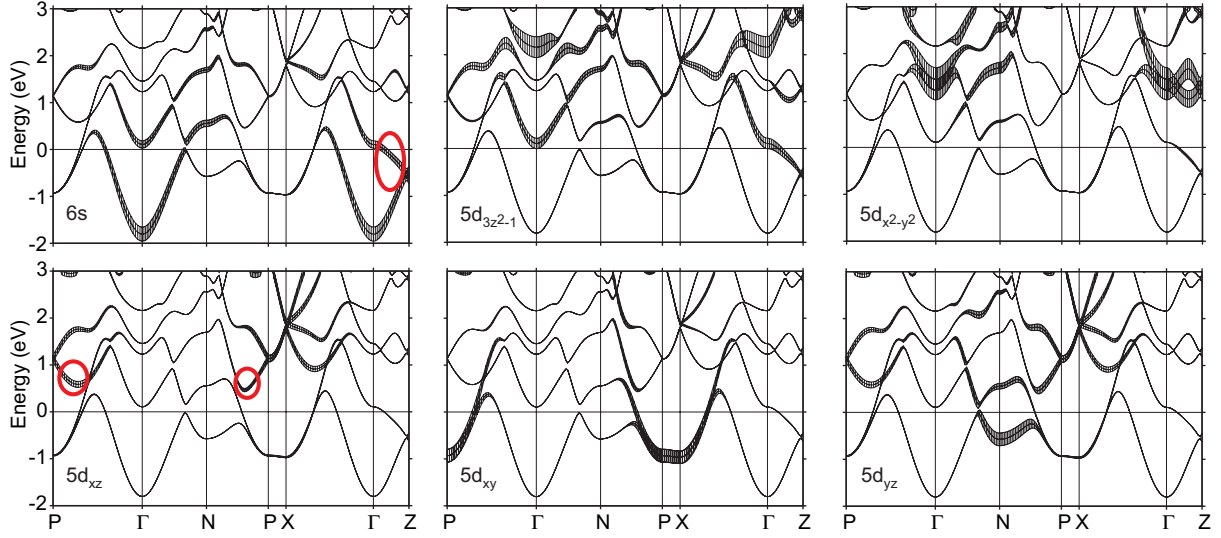


Figure 4.5: Energy bands of Cs-IV at $v/v_0 = 0.4$ with orthogonal LMTO characters (fat bands). A number of bands, circled in red, cross the Fermi level around $v/v_0 = 0.3$ and $v/v_0 = 0.25$.

4.3.3 Phonon Spectra and Electron Phonon Coupling in Cs-II

The density functional linear-response LMTO method was previously used to calculate the phonon spectra of fcc Cs for volumes between $0.44v_0$ and $0.37v_0$.⁶⁰ At the time, the experimental evidence for the complex crystal structure of Cs-III had not yet been published and despite some theoretical evidence pointing to the contrary, it was generally believed that Cs-II undergoes an isostructural phase transition to Cs-III. Kong *et al.* found that around volumes of $v/v_0 = 0.41$ and 0.40 the $T_{[1\bar{1}0]}[\xi\xi 0]$ phonon frequencies become imaginary around $\xi = 1/3$. They concluded that the soft phonon mode should lead to the formation of superstructures prior to the tetragonal Cs-IV transition. The resulting superstructure arising from a $T_{[1\bar{1}0]}[\frac{1}{4}\frac{1}{4}0]$ phonon mode was found to contain triangular prisms, which are also present in the Cs-IV structure. The soft mode leads to an instability in the fcc structure. However, it was concluded that

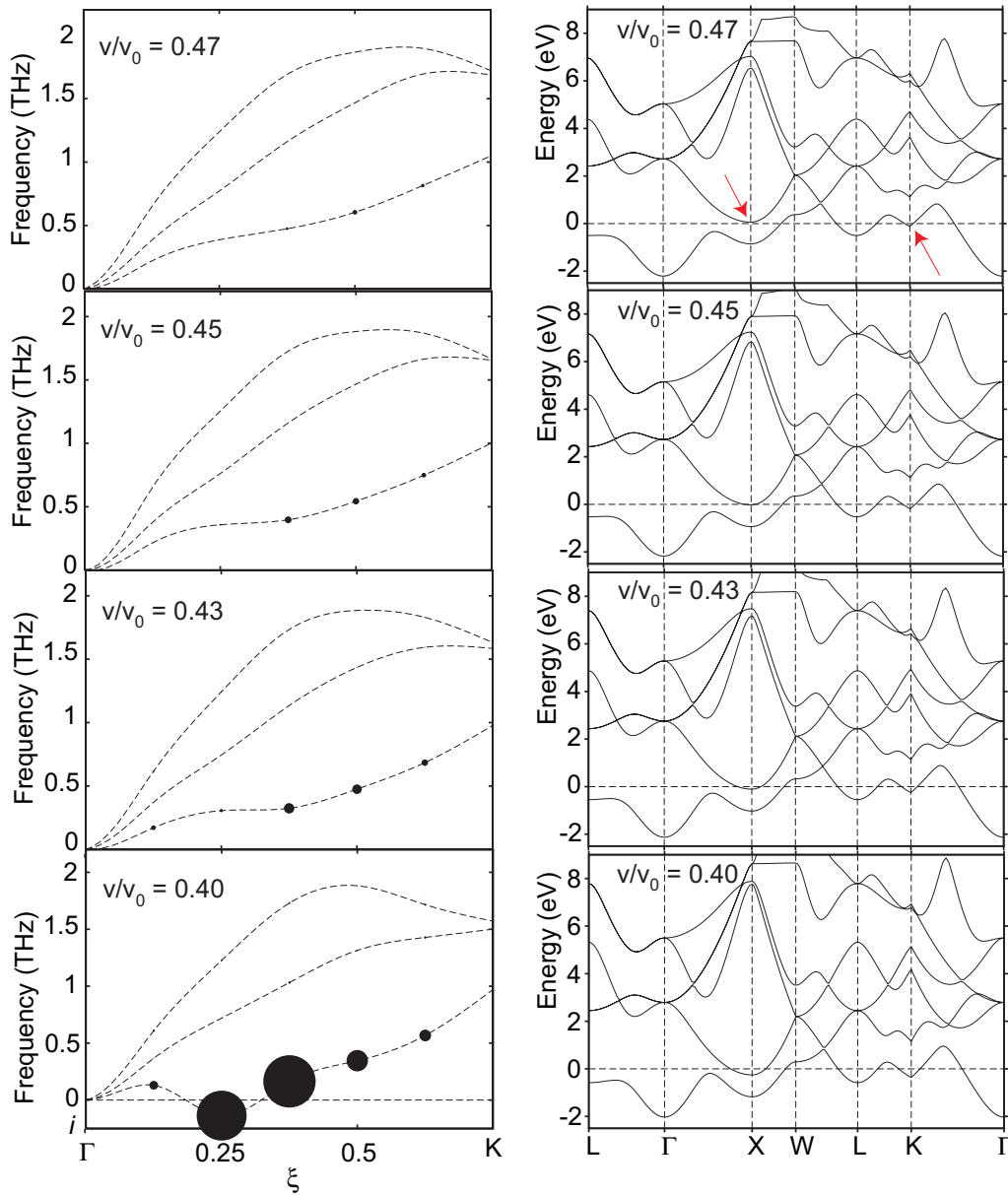


Figure 4.6: Calculated $T_{[1\bar{1}0]}[\xi\xi0]$ phonon dispersion curves for fcc Cs at $v/v_0 = 0.47, 0.45, 0.43$ and 0.40 . The area of each circle is proportional to the electron phonon coupling. Also shown are the FP-LMTO energy bands calculated for the given volumes. At about $v/v_0 = 0.47$ and $v/v_0 = 0.46$ the bands indicated by a red arrow cross the Fermi energy at the K and X points, respectively. As the volume decreases, they fall further below the Fermi level.

the $s \rightarrow d$ transition is also important in the transformation from fcc Cs to Cs-IV. Within this section we will examine this conjecture in more detail.

In Fig 4.6 we show the calculated phonon dispersions for different volumes, along with the FP-LMTO energy bands. The area of the circle is proportional to the electron phonon coupling. Comparison of the phonon dispersions with those of Ref. 60 reveals the same general trends. The phonon mode softens with increasing pressure and at $v/v_0 = 0.40$ the phonon frequency becomes imaginary at $\xi = 1/4$. The slight discrepancies for $v/v_0 = 0.40$ can probably be explained by the fact that in our calculations we used a higher charge density convergence criterion compared to that of Ref. 60. The band structures indicate that at around $v/v_0 = 0.47$ and $v/v_0 = 0.46$ a Lifshitz transition occurs with bands falling below the Fermi energy around the K and X points, respectively. Comparison with the fat bands from Sec. 4.3.2 reveals that the first band has e_g , t_{2g} and s character, whereas the second has only t_{2g} character. As the energy of these bands decreases, the electron phonon coupling increases and at $v/v_0 = 0.40$ the largest interaction is found for $\xi = 0.375$ and $\xi = 0.25$. This suggests that the two bands which cross the Fermi level lead not only to the softening of the phonon mode, but moreover to electron phonon coupling along it.

The LMTO Fermi surface of fcc Cs at $v/v_0 = 0.40$ colored by the electron velocity and the percentage of d -character of the band is shown in Fig. 4.7. The FP-LMTO Fermi surfaces are similar to those calculated with LMTO, the main difference being that in the former the bulge arising from the Lifshitz transition around the K and X points has a larger diameter for a given volume. This can be explained by the fact that in the FP-LMTO calculations the Lifshitz transition occurred at a slightly larger volume than in those performed by LMTO. The LMTO bands are given since the coloring of the Fermi surface by the percentage of d -character has not yet been implemented in the FP-LMTO code. We show two areas where Fermi surface nesting can occur by a shift of approximately $1/3$ along the high symmetry line connecting the Γ and K points. The first is between the pocket which appears around X from the t_{2g} bands crossing the Fermi level and a pocket around the U point. This latter pocket is the result of another Lifshitz transition which occurs at approximately the same volume as that around the K point. The band also contains mixed s and d -character, as can be seen in Fig. 4.7(b). Nesting is also evident between the pocket around the K -point and that around the X -point in the neighbouring Brillouin zone. Once again, both are a result of bands crossing the Fermi level upon increasing pressure. The pocket around X is seen to have a relatively small Fermi velocity and it can be shown that the nesting function becomes large if one of the Fermi velocities involved in the nesting becomes small.⁶⁶ However, in order to verify this, further calculations in the manner of Ref. 66 should be performed. Moreover, in both cases the nesting is between a pocket which is purely d -like and those containing both s and d -character. Thus, fcc Cs becomes unstable under increasing pressure due to the changing Fermi surface topology. Nesting occurs between

pockets in the Fermi surface which arise from the Lifshitz transition. This creates a lattice instability. Moreover, these pockets are responsible for the softening of the $T_{[1\bar{1}0]}[\xi\xi0]$ phonon mode and the strong electron-phonon coupling along it at $\xi = 0.25$ and $\xi = 0.375$.

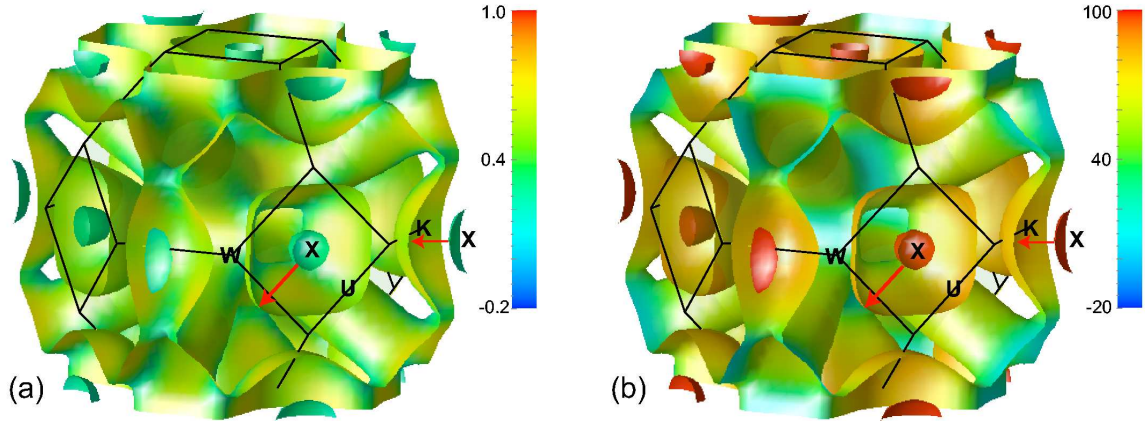


Figure 4.7: LMTO Fermi surface of Cs-II at $v/v_0 = 0.40$ colored by (a) the electron velocity and (b) percentage of d -character. The red arrow denotes a displacement of approximately $[1/4, 1/4, 0]$.

4.3.4 Wannier-like Functions of Cesium

Within this section we will demonstrate that it is possible to generate Wannier-like functions that span only the occupied bands of a metal. We shall first look at the convergence of the bands and the orbital with respect to the size of the supercell used. Whereas we can only hope to reproduce the long-ranged Friedel oscillations for supercells so large that the facets of the folded-in Brillouin zone resemble those of the Fermi surface, much smaller cells turn out to reproduce the rough shape of the occupied orbital. This is a manifestation of what Walter Kohn named the “nearsightedness” of the electronic structure of matter.⁶⁷

The band structure of cesium at ambient conditions (Cs-I) calculated with a full sd basis set on every atom is given in Fig. 4.8 in black. Superimposed on it in red is the band calculated with one s orbital on *every second* cesium atom, obtained specifically by breaking the symmetry and treating Cs metal as CsCl-structured Cs^+Cs^- . In most regions of the Brillouin zone the agreement between the two is good, except it is obvious that with this supercell it is not possible to describe the occupied part of the upper band along $X - \Gamma$. Nonetheless, the orbital can be plotted and is shown in Fig. 4.8.

The result obtained by doubling the cell in all three directions is shown in Fig. 4.9. Now the occupied band structure has improved considerably, but is not yet perfect. The body of the

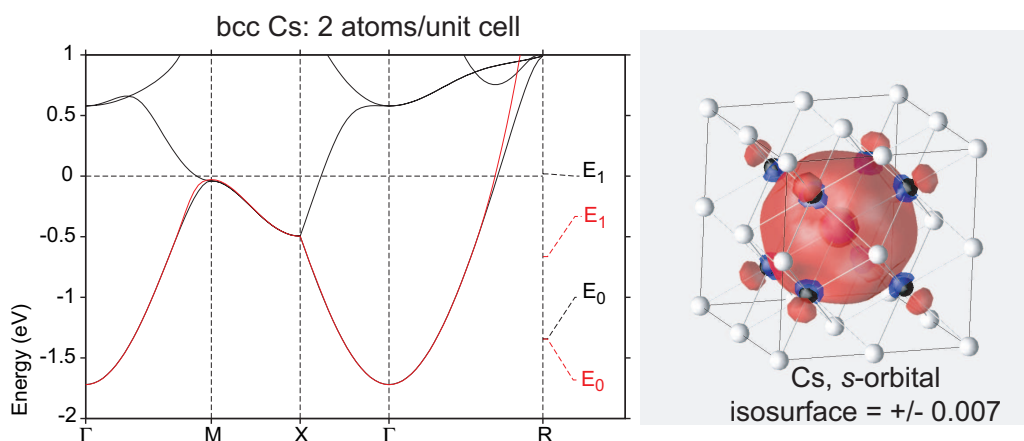


Figure 4.8: Band structure of bcc cesium folded into the 2 atom/cell (CsCl) simple cubic Brillouin zone. The black bands were calculated with a full sd basis on all atoms. The red bands were calculated with an s NMTO on *every second* cesium atom, which is also shown. The white atoms have an s orbital placed on them (active), whereas on the black atoms all partial waves are downfolded (passive).

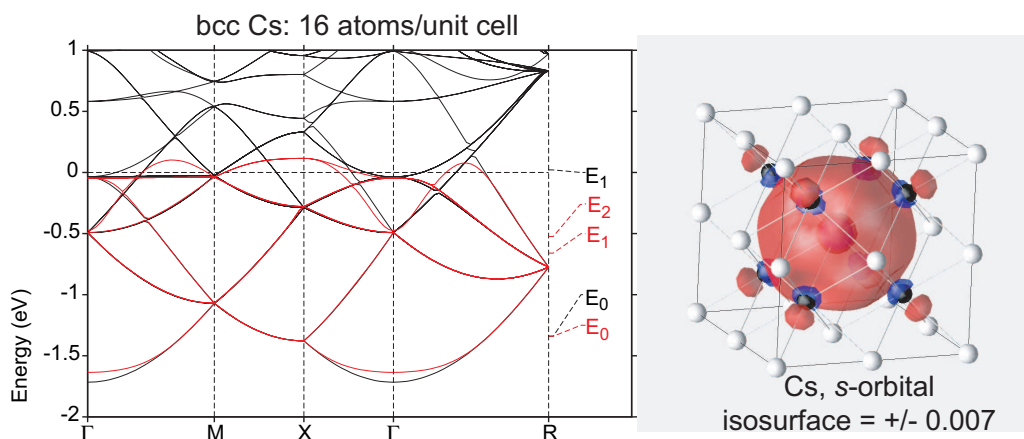


Figure 4.9: As in the previous figure, but for a 16-atom supercell.

orbital obtained from this calculation is, however, very similar to the one generated from the CsCl supercell. The long-ranged tail we do not monitor with the contour chosen in the figures. Already, this orbital at low isosurfaces shows the onset of sd -hybridization. At high isosurfaces (not shown), the orbital is completely s -like. The hybridization is evident in the d_{z^2} character found on the nearest neighbour atoms which have all partial waves downfolded, and therefore can possess any orbital character. It is a result of the fact that even though the occupied band has primarily s character, near the Fermi level some regions with t_{2g} and d_{z^2} character can be found

as shown in Fig. 4.3.

The occupied bands for Cs-II with $v/v_0 = 0.6$ are still primarily s -like, however a fair amount of e_g -character can also be found (Fig. 4.4). The bands and orbital obtained for this structure in a 32-atom supercell are shown in Fig. 4.10. At high contours this orbital is already no longer spherically symmetrical, with four distinct d -like lobes. We have also used the same supercell and downfolding to compute the bands and orbital at $v/v_0 = 0.4$, past the calculated volume of the Lifshitz transition. The downfolded bands, and therefore the orbital, shown in Fig. 4.11, pick up the contribution from this t_{2g} band which has just crossed the Fermi level. At high isosurfaces, this orbital is also no longer s -like and comparison with Fig. 4.10 shows that the effect of increasing pressure is to raise two and lower two of the d -like lobes.

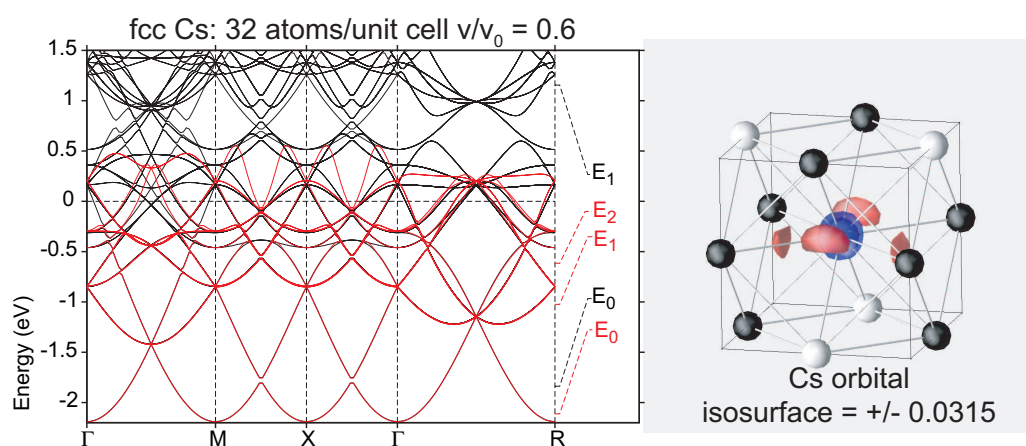


Figure 4.10: As in the previous figure, but for fcc cesium with $v/v_0 = 0.6$, and a 32-atom supercell.

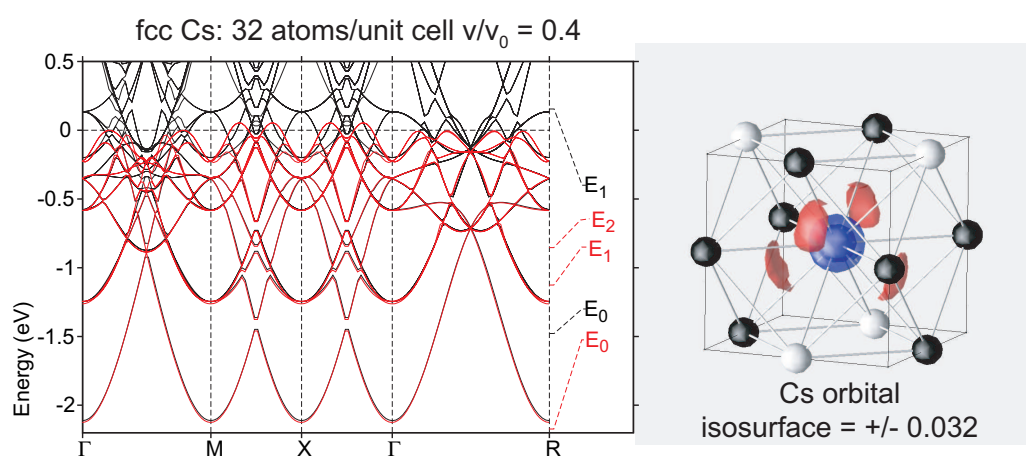


Figure 4.11: As in the previous figure, but for $v/v_0 = 0.4$.

Cs-IV with each cesium atom having a coordination of 8 is no longer a close-packed structure. It can be viewed as a stacking of prisms with a ninety degree rotation from layer to layer in the c -direction. The TB-LMTO calculated charge density (Fig. 4.14) shows maxima in the interstitial regions, in the center of these prisms. The N MTO obtained by placing one s -orbital on every second cesium atom and downfolding all other partial waves is given in Fig. 4.14 and the downfolded bands are compared to those calculated with a full basis set in Fig. 4.12. Clearly this orbital can be obtained from that shown in Fig. 4.11 by raising two and lowering two of the lobes even further. Despite the fact that the downfolded bands do not accurately describe just the occupied bands, placing the Cs-IV Wannier-like function on all of the active sites and squaring it yields a charge density which is almost identical to that calculated with TB-LMTO,³⁹ giving further validation that our method works. At first it may appear unintuitive that the maximum of charge density occurs where the lobes of two different orbitals meet, however Fig. 4.13 reveals that this is indeed the case. Thus, we have shown that N MTOs may be used to give a chemical picture of the pressure induced electronic phase transition in cesium yielding results which are in-line with those obtained from standard electronic structure calculations.

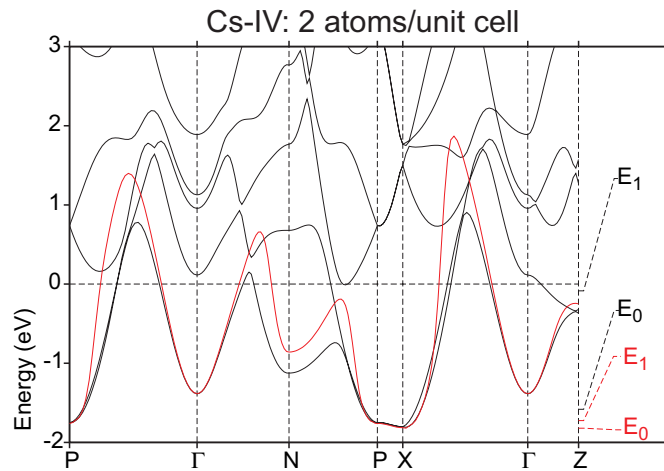


Figure 4.12: As in the previous figure, but for Cs-IV with $v/v_0 = 0.316$, and 2 atoms per unit cell.

4.3.5 Bonding in Cs-IV

Fig. 4.5 illustrates that a substantial amount of the occupied bands in Cs-IV have primarily d -character in agreement with previous theoretical results indicating a valence occupation of $s^{0.2}d^{0.8}$.⁵⁵⁻⁵⁷ The fat bands near the N -point show that the xz and yz bands split yielding one occupied and one unoccupied band. In fact, the stability of the Cs-IV structure is due to the splitting of these bands and within this section we will analyze the bonding between the xz/yz orbitals at the N -point. Fig. 4.15 displays the Bloch sums of these orbitals for both the lower

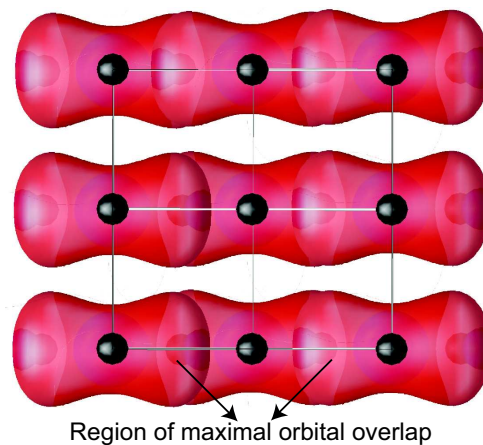


Figure 4.13: One of the lobes of the Cs-IV NMTO placed on nine cesium atoms in a single plane. The lobe which points in the other direction and lies in a different plane has been omitted for clarity. The maximum electron density occurs where the orbitals overlap, in the center of the prisms.

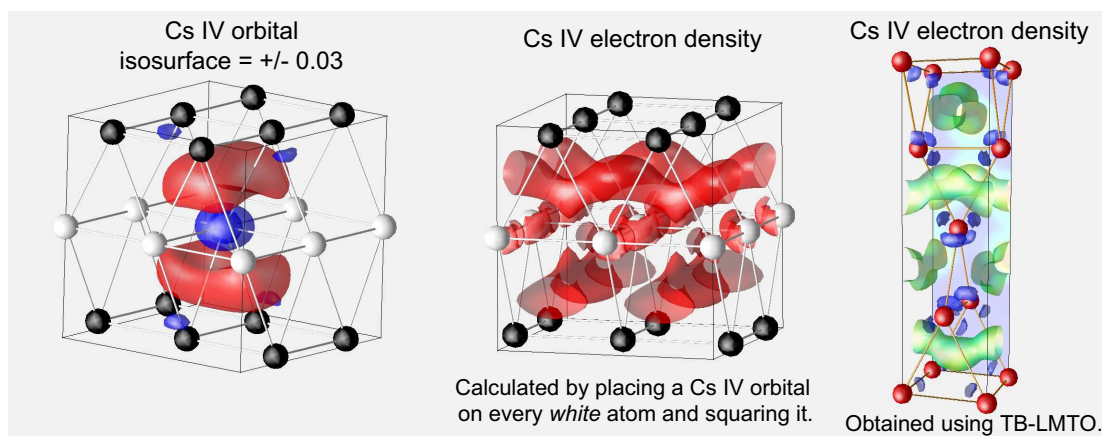


Figure 4.14: The NMTO obtained for Cs-IV ($v/v_0 = 0.316$) with 2 atoms per unit cell. An s orbital was placed on all of the white atoms (active), whereas the partial waves on the black atoms were downfolded (passive). Also shown is the charge density obtained by placing the NMTO on every white atom and squaring it, along with the charge density obtained from a TB-LMTO calculation. The latter charge density is colored by the ELF. The isosurface taken is $0.0063 a_B^{-3}$.

and upper band. The black cesium atoms and solid bonds are within the plane of the page. The dashed bonds point towards the brown cesium atoms which are in the next layer, behind the plane of the page. The charge density displayed a maximum in the interstitial regions where the white circles, corresponding to center of the prisms are located (Fig. 4.14). For both the upper and lower band, $dd\pi$ -bonding between neighbouring cesium atoms within a single xz or yz plane is found. Moreover $dd\sigma$ -bonding and anti-bonding interactions between cesium atoms within a given plane forming the face of a single prism is evident. However, since both bonding and anti-bonding interactions are present, this does not raise or lower the energy of the band. The main difference between the upper and lower bands is that the former display a $dd\delta\pi$ -bonding (something in between a δ and a π bond) and the latter $dd\delta\pi$ -anti-bonding interactions between cesium atoms found within two different layers. Note that the maxima in the charge density run along the direction of these $dd\delta\pi$ -bonds. It is also interesting to note that the lobes of the Wannier-like orbital shown in Fig. 4.14 point in the same direction as the lobes of the xz/yz orbitals which undergo $dd\delta\pi$ and $dd\pi$ -bonding (see Fig. 4.15(c)) and not in the direction where $dd\sigma$ -bonding and anti-bonding interactions are found. Thus, the splitting of the xz/yz bands near the N -point is due to $dd\delta\pi$ -bonding/anti-bonding along the zig-zag regions displaying maximum electron density.

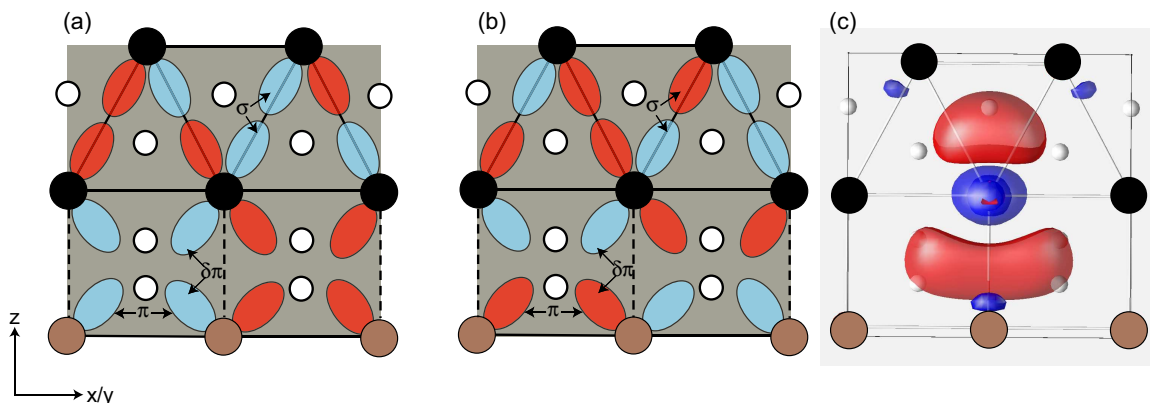


Figure 4.15: The xz/yz orbitals in Cs-IV at the N -point for the (a) lower and (b) upper band. The black and brown Cs atoms are located in and behind the plane of the page, respectively. The white circles correspond to the center of the prisms. (c) The Cs-IV NMTO on the central cesium atom.

4.4 Summary and Conclusions

The structural phase transitions for Cs-I→Cs-II, Cs-II→Cs-III and Cs-IV→Cs-V are experimentally found near volumes where a Lifshitz transition is calculated to occur. For Cs-II, it was shown that the transition brings about the softening of the $T_{[1\bar{1}0]}[\xi\xi 0]$ phonon mode which becomes imaginary at $\xi = 0.25$ around $v/v_0 = 0.40$. For this volume, a large electron phonon coupling was calculated at $\xi = 0.375$ and 0.25 . Fermi surface nesting between purely d -like pockets and those containing sd character was found to occur. The nesting was between regions of the Fermi surface which arose due to the Lifshitz transition and the vector connecting the two nested regions corresponded to the $q = T_{[1\bar{1}0]}[1/4, 1/4, 0]$ soft phonon mode. The pocket around the X -point had a relatively small Fermi velocity, implying that the nesting function might be quite large. However, further calculations are necessary in order to validate this conjecture. Thus, the instability of Cs-II arises due to a purely d -like and an sd band crossing the Fermi level. These regions of the Fermi surface nest onto each other, yielding a soft phonon mode. Possible future work could be to determine if the same phenomena is observed for the other structural transitions in cesium under pressure.

We have also shown that it is possible to generate Wannier-like functions for just the occupied bands in a metal and applied the method to study the electronic $s \rightarrow d$ transition in high pressure cesium. In order to do this, it was first necessary to find an appropriate supercell so that cusps just touch the Fermi level. In practice, it was found that smaller unit cells can reproduce the rough shape of the orbital and are sufficiently accurate to give results in-line with standard electronic structure calculations. The orbitals for Cs-I, Cs-II ($v/v_0 = 0.6, 0.4$) and Cs-IV have been calculated and the latter was shown to yield an electron density which reproduces that obtained from standard electronic structure calculations. At high isosurfaces the Cs-I orbital was found to be completely s -like, whereas for lower values it showed the onset of sd -hybridization. An obvious progression between the orbitals at high isosurface values for the different structures was evident. The completely spherical orbital (bcc Cs) turns into four lobes (fcc Cs, $0.60v_0$) two of which are lowered and two of which are raised at higher pressures ($0.40v_0$). The orbital for Cs-IV can be constructed by a further lowering and raising of the lobes so that they touch.

The stability of Cs-IV was analyzed and attributed to the splitting of the xz/yz bands near the N -point. For the occupied band, these orbitals lead to $dd\delta\pi$ -bonding along the direction of the regions of high electron density in the structure. Moreover, it was noted that the lobes of the calculated Wannier-like orbital point in the same direction as the lobes which undergo $dd\delta\pi$ -bonding.

Chapter 5

The Electronic Structure of α -ThSi₂ and β -ThSi₂

5.1 Introduction

ThSi₂ is dimorphic and can exist in one of two structures, depending upon the temperature of preparation.^{68,69} In the low temperature allotrope, α -ThSi₂ shown in Fig. 5.1(a), the silicon sublattice forms a three-dimensional connected net, with a set of zig-zag chains running in the x -direction (Si₁ and Si₃) and a set running in the y -direction (Si₂ and Si₄). The two sets are connected by bonds along the z -direction. The high temperature allotrope, β -ThSi₂, has the AlB₂ structure and is shown in Fig. 5.1(b). Here, the silicon sublattice forms a graphite-like, honeycomb structure with the thorium atoms in a triangular lattice halfway between the silicon layers. In both cases, silicon is found to be threefold coordinate. The transformation between the two structures occurs when α -ThSi₂ is heated above 1400 °C.⁶⁸

The aforementioned structures are both superconducting with a T_c of 3.16 K and 2.41 K for α -ThSi₂ and β -ThSi₂, respectively.⁷⁰ Substitution of silicon by iridium,^{71,72} rhodium,⁷² and cobalt, nickel and platinum⁷³ has led to the preparation of other superconducting materials. X-ray photoemission spectroscopy (XPS) on α -ThSi₂ has been performed (see Fig. 5.11).⁷¹ The Fermi level (set to 0 eV) was shown to have predominantly thorium 6*d* character. A peak appearing at ≈ -2.5 eV was attributed to thorium 6*d* and silicon 3*p* bonding states, whereas a peak located at ≈ -6 eV was found to be a mixture of silicon 3*s* and 3*p*. Finally, at ≈ -8 eV a peak corresponding to almost pure silicon 3*s* was found. The results were also thought to indicate charge transfer from thorium to silicon. To the best of our knowledge, there have not been any XPS studies on β -ThSi₂.

Previous theoretical work has focused on calculating the band structure of the α -ThSi₂ silicon sublattice and comparing it with that of a graphite-like silicon sheet.⁷⁴ The π interaction between p orbitals of adjacent silicon atoms was found to be weaker for the connected net. As a

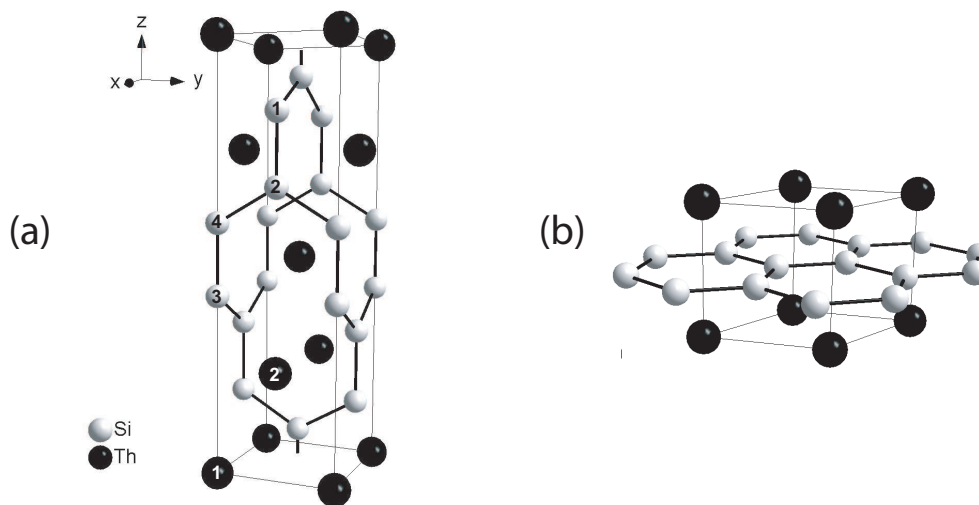


Figure 5.1: The unit cells of (a) α -ThSi₂ and (b) β -ThSi₂.

consequence, the energy of the π^* level was also lowered. This led to the conclusion that when there are more than 4.5 electrons per silicon (filling of the π^* -band is underway), the α -ThSi₂ sublattice should be stabilized over the β -ThSi₂ sublattice.

The interesting pressure induced structural transitions which occur in cesium have been previously outlined in Chapter 4. It has been noted that some of these high pressure structures are similar to those found in other solids, leading to the idea that perhaps the bonding within different systems is of a similar nature. For example, Cs-V and Si-VI have the same space group and nearly identical axial ratios and axial coordinates. However, theoretical investigations have shown that Si-VI is nearly free-electron-like, whereas Cs-V was found to exhibit multi-center *d*-electron bonding.⁵³ As can be seen from Fig. 5.2, the thoriums in α -ThSi₂ are located in the same positions as the atoms in Cs-IV. Curiously, band structure calculations revealed that the maximum of electron density for both structures is found along the zig-zag chains, see Fig. 5.2, which correspond to the region along the electronegative silicon atoms in α -ThSi₂. However, there are no atoms located in the regions of maximum electron density in Cs-IV. This was first pointed out by von Schnering and Nesper, who suggested that Cs-IV should therefore be viewed as a cesium electride, Cs⁺e⁻, where one electron occupies the position of two silicon atoms in α -ThSi₂.⁷⁵

In this chapter we calculate the band structure of α -ThSi₂ and β -ThSi₂ using the linear muffin-tin orbital (LMTO) method^{7,39} and newly developed NMTO methods (MTOs of order *N*).^{17,27} The main goal of this investigation is to gain an understanding of the chemical bonding

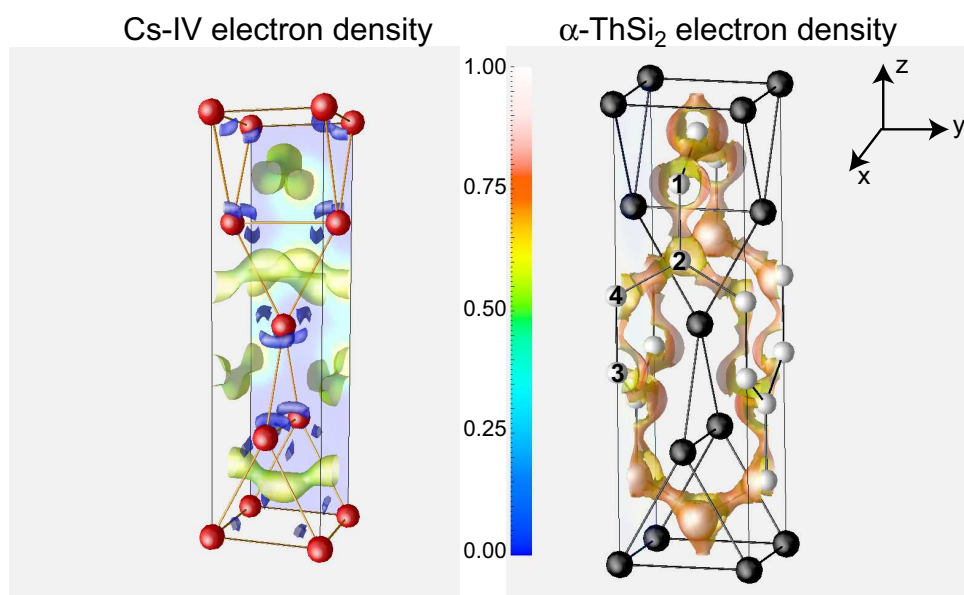


Figure 5.2: TB-LMTO three-dimensional occupied valence electron density surface for Cs-IV and α -ThSi₂ colored by the value of the electron localization function (ELF). The isosurfaces were taken as $0.0063 a_B^{-3}$ and $0.06 a_B^{-3}$, and the number of valence electrons are one and twelve per formula unit for Cs-IV and α -ThSi₂, respectively. Cesium atoms are red, thorium atoms are black, silicon atoms are white.

in α -ThSi₂ and β -ThSi₂ and to present how the NMTO method may be used to this end. In particular, we will show that a complex bonding situation can be analyzed by using an appropriate NMTO minimal basis set to pick out groups of bands and that the orbitals obtained from this minimal basis can be used to visualize chemical bonding in the solid state. We will first consider β -ThSi₂ since it has a simpler structure. Next, it will be shown that a similar analysis can be used to understand the bonding in α -ThSi₂. Finally, we will provide an alternative interpretation for α -ThSi₂, based upon the analysis for Cs-IV presented in Chapter 4.

5.2 Computational Details

Structure of α -ThSi₂ and Cs-IV

Both Cs-IV and α -ThSi₂ have the space group $I4_1/amd$ (141), with the thorium, cesium and silicon atoms located in the 4a, 4a and 8e Wyckoff positions, respectively. The primitive cell contains two formula units and has dimension $a \times a \times c/2$. Further computational details for Cs-IV can be found in Sec. 4.2. For α -ThSi₂, the lattice constants a and c were taken from experimental data as being 4.126 Å and 14.346 Å.⁷⁶ Expressed in Cartesian coordinates, the prim-

itive translation vectors are: $\mathbf{T}_1=(a, 0, 0)$, $\mathbf{T}_2=(0, a, 0)$ and $\mathbf{T}_3=(a/2, a/2, c/2)$. The primitive reciprocal lattice vectors are $\mathbf{G}_1=(2\pi/a, 0, 2\pi/c)$, $\mathbf{G}_2=(0, 2\pi/a, 2\pi/c)$ and $\mathbf{G}_3=(0, 0, 4\pi/c)$. Fig. 5.3(a) shows the high symmetry points in the Brillouin zone (primitive cell of reciprocal lattice): $\Gamma = (0, 0, 0)$, $Z = (\mathbf{G}_3/2) = (0, 0, 2\pi/c)$, $N = (\mathbf{G}_1/2) = (\pi/a, 0, \pi/c)$, $P = (2\mathbf{G}_1+2\mathbf{G}_2-\mathbf{G}_3)/4 = (\pi/a, \pi/a, \pi/c)$ and $X = (\mathbf{G}_1+\mathbf{G}_2-\mathbf{G}_3)/2 = (\pi/a, \pi/a, 0)$.

Structure of β -ThSi₂

The β -ThSi₂ structure is hexagonal and has the space group P6/mmm (191) with thorium and silicon located in the 1a and 2d Wyckoff positions. Its primitive cell contains one formula unit and has dimensions $\sqrt{3}a/2 \times a \times c$. The lattice constants a and c were obtained from experimental data⁶⁸ as being 3.985 Å and 4.220 Å, respectively. The primitive translation vectors, expressed in Cartesian coordinates are: $\mathbf{T}_1=(a, 0, 0)$, $\mathbf{T}_2=(-a/2, \sqrt{3}a/2, 0)$, $\mathbf{T}_3=(0, 0, c)$. The primitive reciprocal lattice vectors are $\mathbf{G}_1=(2\pi/a, 2\pi/\sqrt{3}a, 0)$, $\mathbf{G}_2=(0, 4\pi/\sqrt{3}a, 0)$ and $\mathbf{G}_3=(0, 0, 2\pi/c)$. Fig. 5.3(b) shows the high symmetry points in the Brillouin zone: $\Gamma = (0, 0, 0)$, $A = (\mathbf{G}_3/2) = (0, 0, \pi/c)$, $M = (\mathbf{G}_2/2) = (0, 2\pi/\sqrt{3}a, 0)$, $L = (\mathbf{G}_2+\mathbf{G}_3)/2 = (0, 2\pi/\sqrt{3}a, \pi/c)$, $K = (\mathbf{G}_1+\mathbf{G}_2)/3 = (2\pi/3a, 2\pi/\sqrt{3}a, 0)$ and $H = (2\mathbf{G}_1+2\mathbf{G}_2+3\mathbf{G}_3)/6 = (2\pi/3a, 2\pi/\sqrt{3}a, \pi/c)$.

LMTO Calculations

The Vosko-Wilk-Nusair (VWN)⁴⁰ local exchange correlation potential (LDA) was used along with Perdew-Wang⁴¹ generalized gradient approximation (GGA). Scalar relativistic effects were included. In order to gain a chemical understanding of the bonding in α -ThSi₂ and β -ThSi₂, it was not necessary to take spin-orbit coupling into account, since its effect was found only to split degenerate bands by an amount not exceeding ≈ 0.2 eV. The basis set consisted of spd LMTOs on silicon and sd LMTOs on thorium, with p and f LMTOs downfolded. Inclusion of the thorium f orbitals in the basis was found to have a negligible effect on the band structure. For silicon and thorium, the sphere radii employed were 131.0 pm and 216.0 pm in the case of

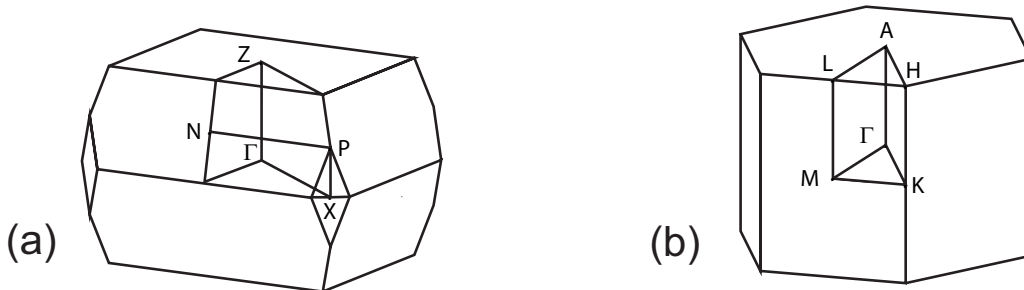


Figure 5.3: The Brillouin zones of (a) α -ThSi₂, Cs-IV and (b) β -ThSi₂.

α -ThSi₂ and 125.4 pm and 214.8 pm in the case of β -ThSi₂. In both cases, it was not necessary to insert empty interstitial spheres. The calculations utilized 961 and 980 irreducible points in the tetrahedron k -space integrations⁴² for α -ThSi₂ and β -ThSi₂, respectively. For α -ThSi₂ and β -ThSi₂ 3101 and 3501 points were used to generate the density of states.

NMTO Calculations

The present version of the NMTO program is not self-consistent and requires the output files of the self-consistent potential from the TB-LMTO program. The screening radii, a_R , were chosen to be as large as possible and non-overlapping. Therefore defining $\sigma = a_R/s_R$ where s_R is the potential sphere radius, led to a choice of $\sigma = 0.7$ for silicon and $\sigma = 0.8$ for thorium. In general, the a_R should be taken as 0.9 times the tabulated covalent, atomic or ionic radii. Our choice of σ gives $a_{Si}=121.5$ pm, $a_{Th}=138.8$ pm for α -ThSi₂ and $a_{Si}=119.1$ pm, $a_{Th}=136.1$ pm for β -ThSi₂. In comparison, the covalent radii for silicon and thorium are 117 pm and 165 pm. The calculations showed a transfer of electrons from thorium to silicon, hence the screening radii should be compared with the ionic radii for Si⁻/Th²⁺ or Si²⁻/Th⁴⁺. Data for these particular ionic radii were not available, but for silicon the value should be larger than the covalent radius, whereas for thorium it should be smaller. Thus, the screening radii used are appropriate for negatively charged Si and positively charged Th atoms. The downfolding schemes and energy meshes employed for particular calculations will be stated in the results and discussion section of this chapter.

5.3 Results and Discussion

5.3.1 Gross Features of the Band Structure of β -ThSi₂

Silicon and thorium have a [Ne]3s²3p² and [Rn]6d²7s² electronic configuration, yielding 12 valence electrons per unit cell in β -ThSi₂. The total and projected density of states is given in Fig. 5.4. A line crossing the right hand side of the y -axis corresponds to the integrated density of states at the Fermi energy. The projected density of states for silicon 3d, thorium 7p and thorium 5f have been summed and given the label 'Downfolded'. Experimental XPS data for β -ThSi₂ could not be found, however the calculated density of states compares reasonably well to that reported for α -ThSi₂.⁷¹ The region between -12 to -8 eV has primarily Si s character; that between -6 eV and -4 eV consists mostly of Si p; between -4 eV to -2 eV the major contributions arise from Si p and Th d states. Later on we will show that the features in the calculated density of states for α -ThSi₂ are very similar to those for β -ThSi₂, giving an indication that the chemical bonding within these two structures is similar in origin.

Fig. 5.5 shows the band structure of β -ThSi₂ decorated with eigenvectors in an orthogonal

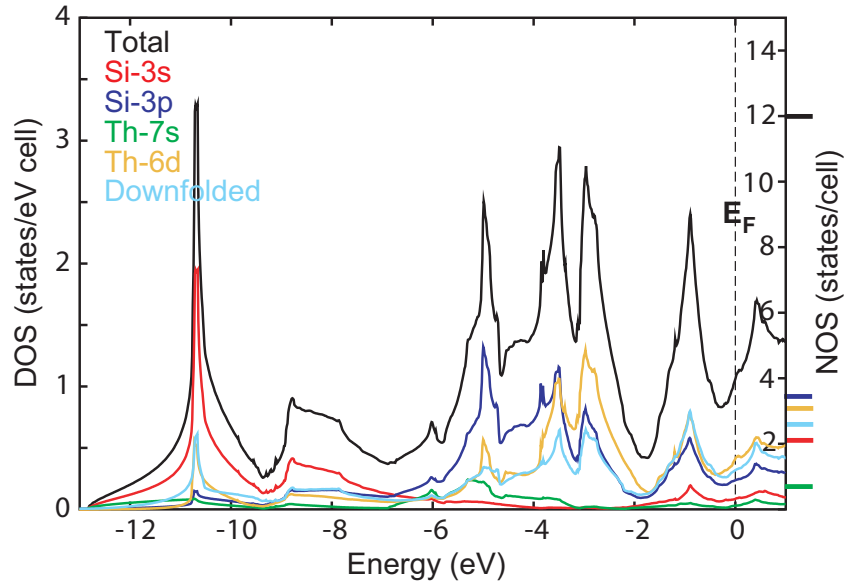


Figure 5.4: Calculated projected and total density of states for β -ThSi₂. The integrated density of states at the Fermi energy is given by a tick on the right hand side of the y -axis.

representation (fat bands). The lowest three bands display primarily σ -bonding character, in-line with the observation that the angle between adjacent silicon atoms is exactly 120° , suggesting sp^2 -hybridization. Some of the sp^2 anti-bonding states are also occupied and they hybridize with thorium d -orbitals near the Fermi level, for example along $A - L$ and $M - K - \Gamma$. The π orbitals are the p_z on each silicon atom and the π and π^* bands are almost full, except for a pocket around Γ . Despite the fact that character from thorium s and all five thorium d orbitals may be found under the Fermi level, that arising from s and d_{z^2} appears to be predominant, hybridizing with the silicon π bands along $\Gamma - A - L$. Within the next section we will employ the $NMTO$ method to create a truly minimal basis set which accurately describes most of the occupied bands. The Wannier-like functions obtained from this basis will prove to be useful in understanding and visualizing the chemical bonding within the system.

5.3.2 $NMTO$ Wannier-like Functions for β -ThSi₂

In Sec. 3.4.1 we have shown that it is possible to generate Wannier-like functions for only the occupied σ -bonding bands in graphite by placing an sp^2 basis on *every second* carbon atom, choosing an appropriate energy mesh, and letting the method shape the orbitals accordingly. This same procedure may be followed to obtain a basis set which describes the three lowest sp^2 bands in β -ThSi₂. Thus, the three $NMTO$ s which span the Hilbert space of the three σ -

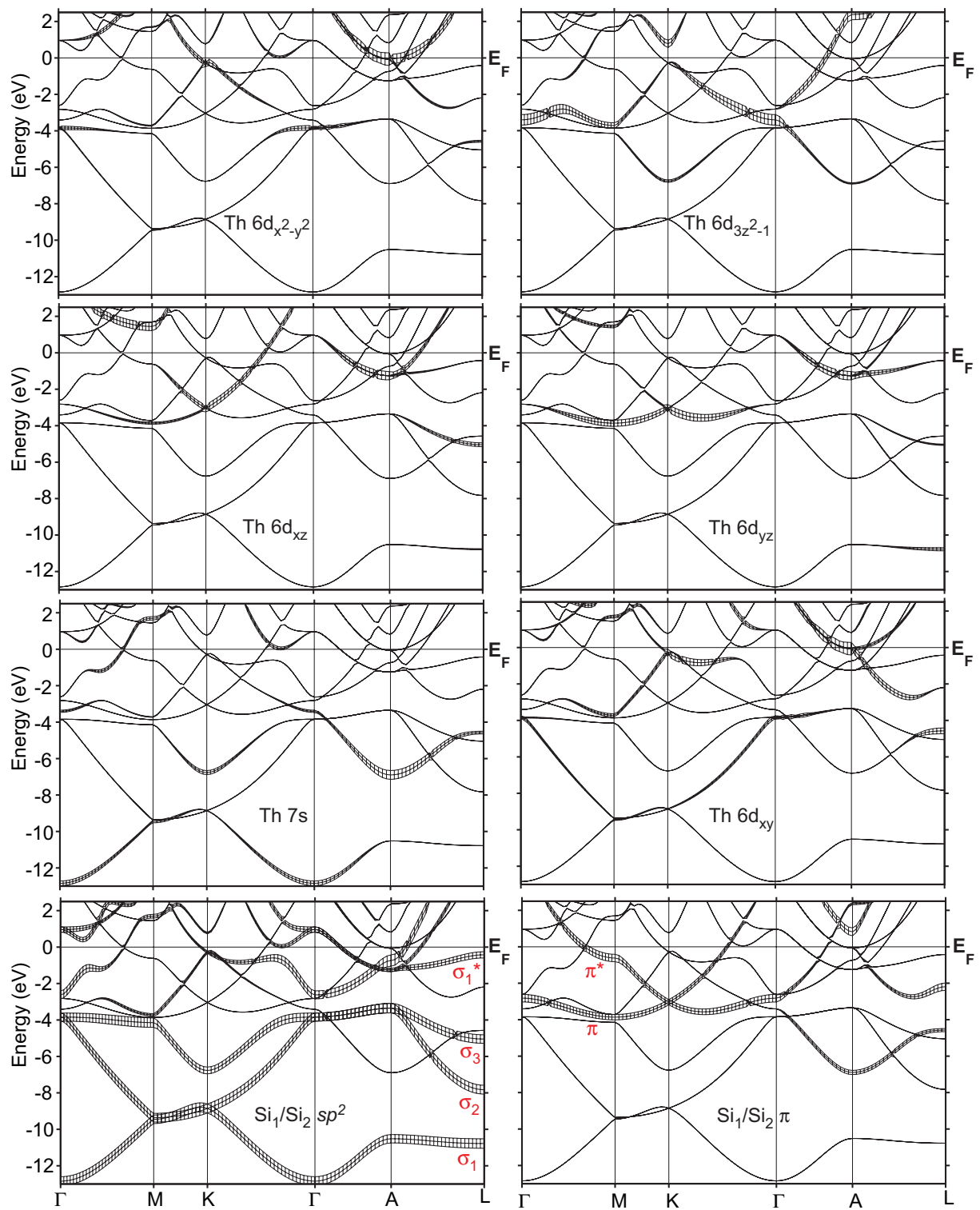


Figure 5.5: Energy bands of β -ThSi₂ with orthogonal LMTO characters (fat bands).

bonds are simply the s , p_x and p_y NMTOs on every second silicon. The partial waves on all other atoms, the other silicons in particular, are downfolded into the tails of these orbitals. Symmetrical orthogonalization of these orbitals yields three congruent σ -bonding orbitals. In Fig. 5.6 we show the calculated band structure of β -ThSi₂ obtained using this minimal basis in red, along with the bands obtained from a full (spd on silicon and sd on thorium) basis set in black. The two are almost identical on the scale of the figure. It should be noted that the energies of the NMTO bands do not correspond exactly to those of the LMTO bands shown in Fig. 5.5 due to the fact that the former are inherently more accurate and therefore lower in energy (variational principle).

Fig. 5.6 also gives the s , p_x and p_y Wannier-like functions for silicon, along with one of the three congruent σ -bonding orbitals. The boundary conditions imply that the orbitals may

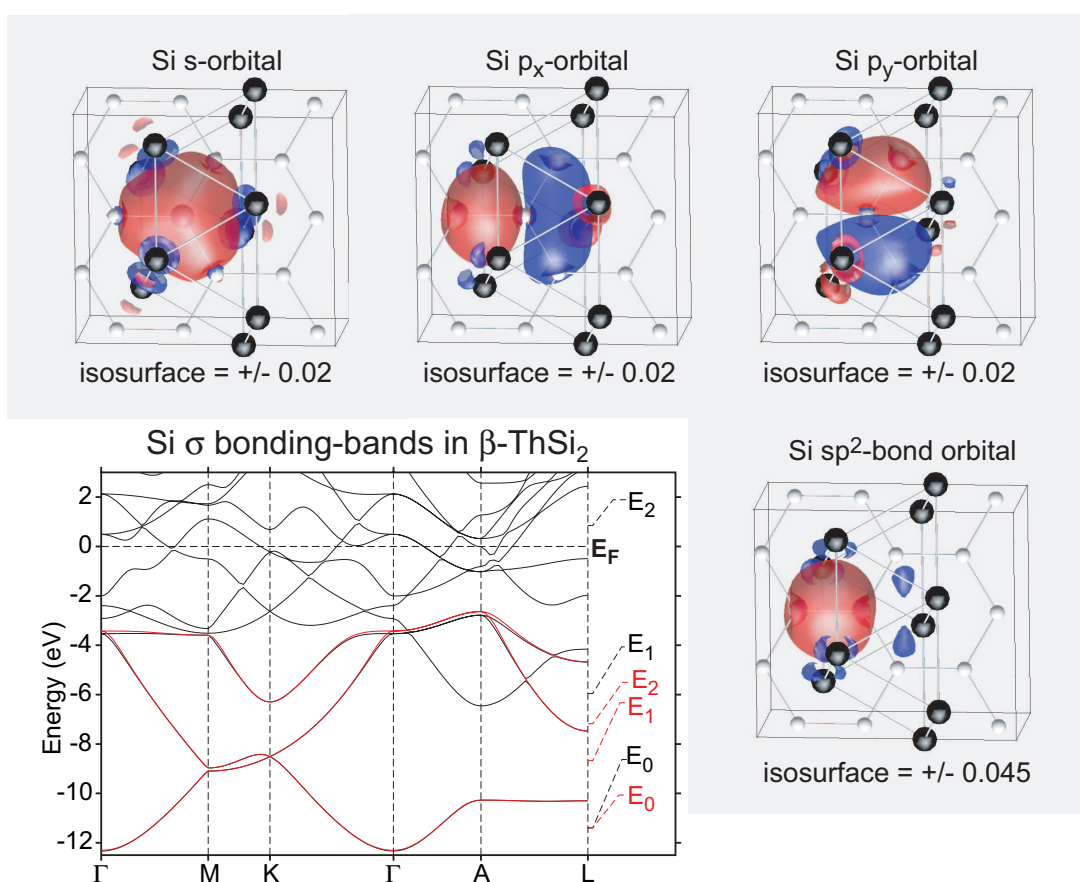


Figure 5.6: The band structure of β -ThSi₂ calculated with a full (spd on Si, sd on Th) basis set in black. The red bands have been calculated with a σ -bonding basis set (s , p_x and p_y NMTO on every second silicon atom). Also shown are the three NMTOs along with one of the three congruent sp^2 -bond orbitals. The energy meshes used for each calculation are given to the right of the band structure.

spread out onto their nearest neighbour silicon atoms but are confined not to have any s , p_x or p_y character on the second nearest neighbours, where orbitals have been placed. They may have any character on the thorium atoms and examination reveals s and d -like tails in-line with the fat bands which showed that the σ -bonding bands also contain some thorium character. They are comparable, but not identical, to the sp^2 orbitals obtained for graphite in Fig. 3.4. Thus, the lowest three bands arise primarily due to σ -bonding between adjacent atoms in the silicon sublattice. A small amount of hybridization between the sp^2 -orbitals and the thorium s and d orbitals is found to occur.

It is also possible to calculate a Wannier-like function which just describes the lower bonding π -band in β -ThSi₂, in the same manner as was done for graphite in Sec. 3.4.1. Here, we place a p_z orbital on every second silicon atom and choose an energy mesh which spans the energy range of the bonding band. The downfolded band structure, given in red in Fig. 5.7, agrees well with that obtained using a full basis set, the only deviation being along the $A-L$ high symmetry line. The π -bonding NMTO spreads out onto the adjacent silicon atoms where orbitals have not been placed. It is very similar to that obtained for graphite in Fig. 3.2, except that it has sd -like tails on the six neighbouring thorium atoms. This is in agreement with the fat bands in Fig. 5.5 which show hybridization between the silicon π and thorium orbitals, for example the Th d_{z^2} and Th s along $\Gamma-A-L$ and Th d_{yz} along $\Gamma-M-K-\Gamma$. Hence, it can be concluded that the Si π -bonding band is full and that it hybridizes with the s and d orbitals on the nearest neighbour thorium atoms.

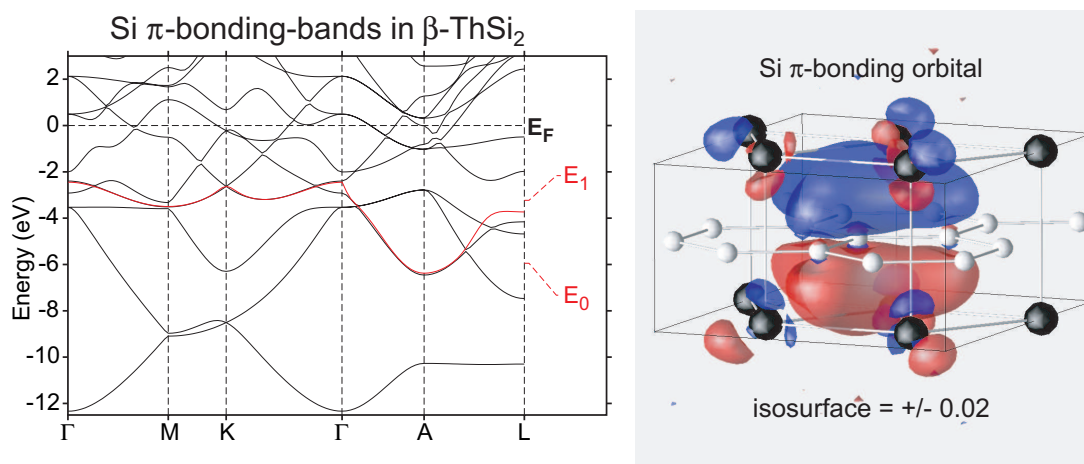


Figure 5.7: The black bands are the same as in Fig. 5.6. The red bands have been calculated with a π -bonding basis set (p_z NMTO on every second silicon atom, which is also shown).

So far we have constructed Wannier-like functions for three σ -bonding and one π -bonding band in β -ThSi₂. In order to obtain a truly minimal basis set, that is one with as many orbitals

as occupied bands, it is necessary to add two more orbitals per ThSi₂ unit to the basis. Since β -ThSi₂ is an inter-metallic compound, some regions of the Brillouin zone do not contain exactly six occupied bands. Therefore, unless a supercell approach is used, as was done for cesium in Sec. 4.3.4, complete agreement between the two band structures cannot be obtained. However, the band structure of β -ThSi₂ contains many cusps where the bands cross the Fermi level and therefore it should be possible to generate a truly minimal basis which describes most of the occupied bands accurately. The two highest occupied bands contain primarily Si π^*/σ^* and Th d_{z^2} character, suggesting that two of these five orbitals might be an appropriate choice. The bands obtained with an s and p_z basis on every second silicon atom using an energy mesh which lies just below the Fermi level are given in Fig. 5.8. They agree reasonably well to those calculated with a full basis, except for a few regions. Further examination reveals that the bands which are not fully reproduced are those containing Th d_{z^2} character, for example along $\Gamma - M$ and $K - \Gamma$. At these points they jump and try to reproduce those bands having primarily Si s character. These orbitals hybridize yielding two $s^*\pi^*$ NMTOs, one which points towards the lower and the other towards the upper triangular thorium sublattice. The Wannier-like orbital in Fig. 5.8 shows substantial hybridization with the d_{z^2} orbitals on the three nearest neighbour thoriums.

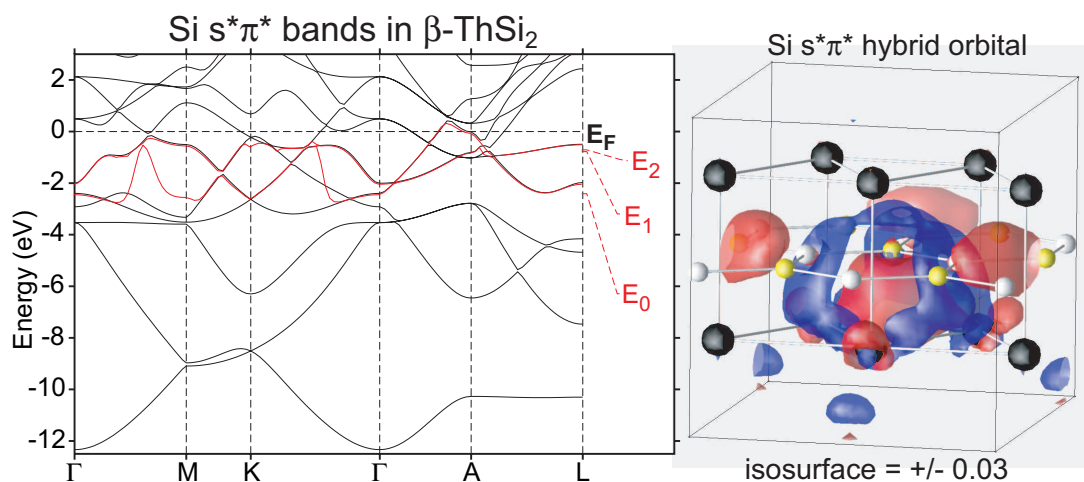


Figure 5.8: The black bands are the same as in Fig. 5.6. The red bands have been calculated with a π^* , s^* basis set (s , p_z NMTO on every second silicon atom). Also shown is one of the two congruent $s^*\pi^*$ hybrid orbitals.

This analysis suggests that the Si σ , π , π^* and s^* orbitals may be able to yield a truly minimal basis for β -ThSi₂. The bands calculated in this manner do a good job of describing the bands under the Fermi level, see Fig. 5.9. Surprisingly, even the bands which were not so well reproduced in Fig. 5.8 are now in good agreement with the full band structure. The reason

for this might be that a larger basis is more flexible than a smaller one. Another possibility is that in Fig 5.9 it was possible to use an energy mesh which did not span the uppermost bands, contrary to Fig. 5.8. In the latter case the method may not know which bands to “pick” since many of the bands display the same orbital character.

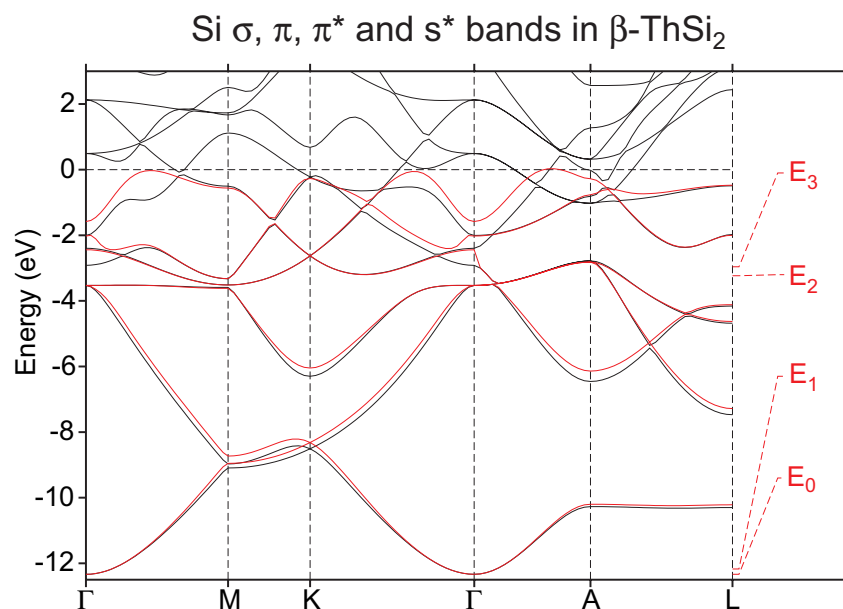


Figure 5.9: The black bands are the same as in Fig. 5.6. The red bands have been calculated with a σ, π, π^*, s^* basis set (s, p_z NMTO on every silicon atom and a p_x and p_y NMTO on every second silicon atom).

This truly minimal basis yields orbitals which are somewhat different from those presented previously. Comparison of the s, p_x, p_y NMTOs and the σ -bonding orbital in Fig. 5.6 with that given in Fig. 5.10 shows that for the same isosurface the latter display larger tails on the neighbouring silicon atoms. Moreover, they are no longer symmetrical with respect to the crystal lattice since we have specifically broken the symmetry in our choice of the basis. As was shown in Sec. 3.2.1, Wannier functions which are maximally localized and not symmetry breaking can be obtained in a further step. This however is currently not implemented within the program and is an area which should be worked on in the future. We also show the two $s^*\pi^*$ hybrids obtained from this basis. Both of their lobes point between one of the triangular faces of the thorium sublattice which lie below or above the plane of the silicons. Clearly, the larger lobe displays a substantial amount of d_{z^2} character on the neighbouring three thoriums. The smaller lobe is seen to also contain contributions from orbitals on the Th atoms since it is no longer almost completely spherical, like the π non-bonding orbital, but rather triangular in shape. It thus becomes obvious why the red bands in Fig. 5.9 were able to reproduce even those bands which showed primarily Th d_{z^2} character: the Th d_{z^2} orbitals point towards the silicons

and bond with the $s^*\pi^*$ hybrids. The most notable difference between the orbitals obtained using the truly minimal basis and those which describe only a single band or group of bands is that a π non-bonding orbital on each silicon is obtained since both the π and π^* orbitals are included within the basis. This also affects the appearance of the $s^*\pi^*$ hybrid which is now localized around a single Si.

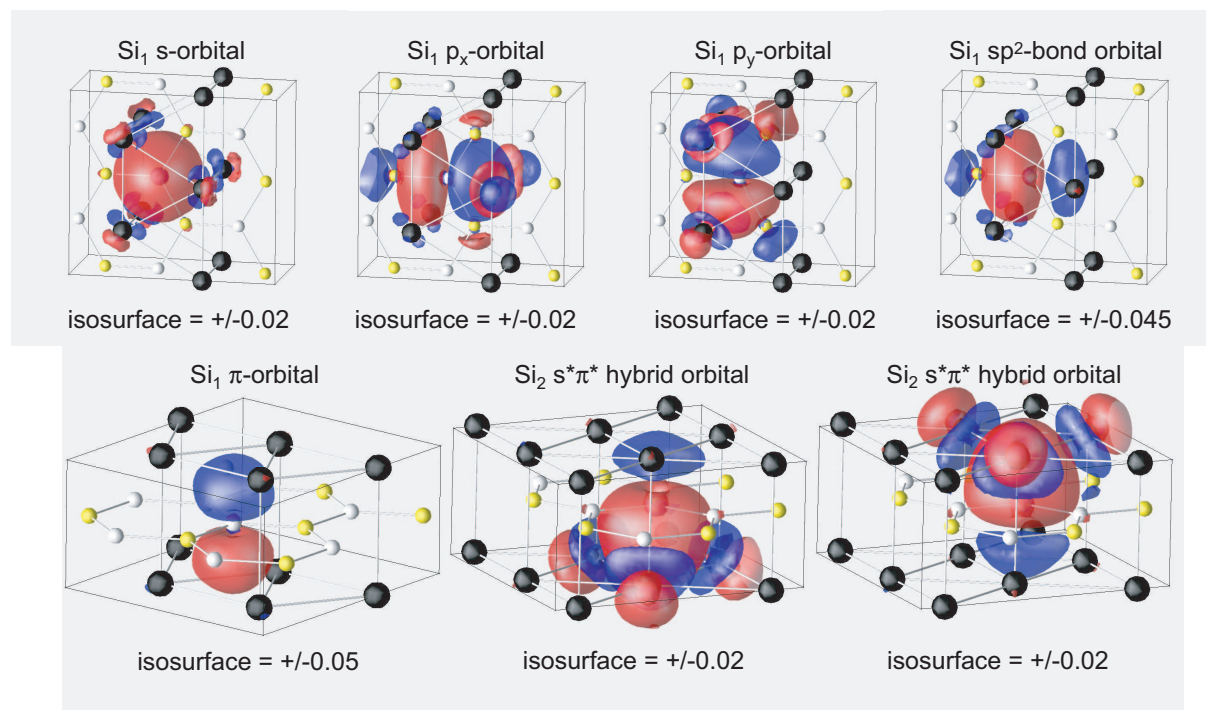


Figure 5.10: The s , p_x and p_y NMTOs, along with one of the three congruent σ -bonding orbitals obtained from the downfolded (red) band structure in Fig. 5.9. Also shown is the π non-bonding orbital and the two congruent $s^*\pi^*$ hybrids. A σ/π and a s^*/π^* basis was placed on the white and yellow silicon atoms, respectively.

In conclusion, we have used the newly developed NMTO method to analyze a complex bonding situation in an inter-metallic compound, β -ThSi₂. We have shown that three of the bands, which contain six electrons, arise from sp^2 σ -bonding within the silicon sublattice. Another band (two electrons) can be described by a Si π -bonding orbital. These NMTOs hybridize slightly with Th s and d states. The remaining two bands (four valence electrons) can be constructed from Si $s^*\pi^*$ anti-bonding NMTOs which hybridize strongly with the neighbouring thorium atoms, in particular with the d_{z^2} orbitals. The Wannier-like functions show a bonding interaction between the $s^*\pi^*$ hybrids and the thorium atoms lying in a triangular lattice above and below the plane of the graphite-like silicon sheet.

5.3.3 Gross Features of the Band Structure of α -ThSi₂

Each primitive unit cell of α -ThSi₂ contains two ThSi₂ formula units and therefore 24 valence electrons. The total and projected density of states in Fig. 5.11 is similar to that presented previously for β -ThSi₂ in Fig. 5.4 and agrees well with the experimental XPS data.⁷¹ In particular, the region between -12 to -8 eV has primarily Si *s* character; that between -8 to -5 eV consists mostly of Si *s* and *p*; from -5 to 0 eV the major contributions arise from Si *p* and Th *d*.

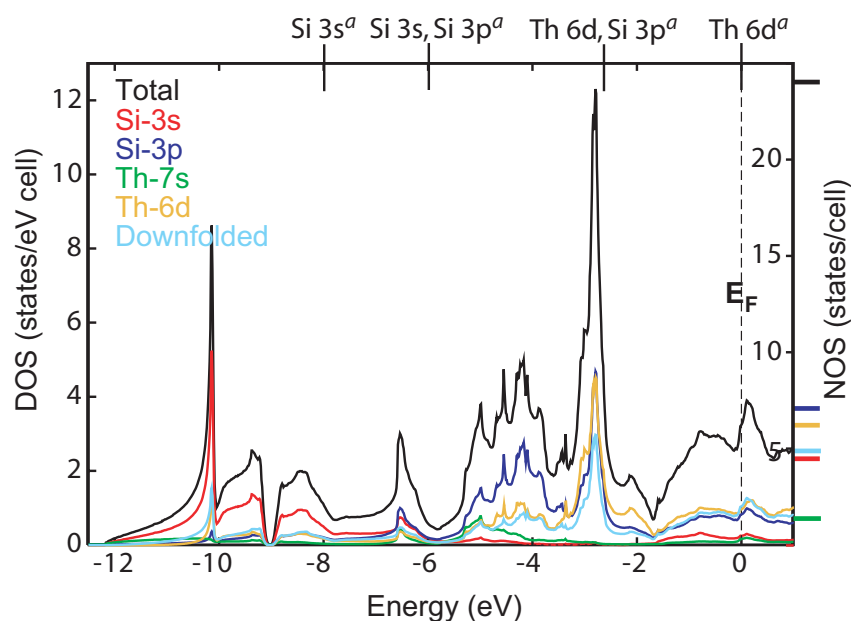


Figure 5.11: Calculated projected and total density of states for α -ThSi₂. The integrated density of states at the Fermi energy is given by a tick on the right hand side of the *y*-axis. ^aPosition and assignment of the peaks in the experimental XPS data of Ref. 71

Fig. 5.12 displays the TB-LMTO band structure for α -ThSi₂ decorated with eigenvectors in an orthogonal representation. The fat bands are identical for Th₁ and Th₂, Si₁ and Si₃, Si₂ and Si₄. The only difference between Si₁/Si₃ and Si₂/Si₄ is that the features in the *x* and *y* directions are interchanged due to the fact that the zig-zag chains in the silicon sublattice run in the *x*-direction for Si₁/Si₃ and in the *y*-direction for Si₂/Si₄. Each atom in the silicon sublattice is found in a trigonal planar environment and the bond angles between adjacent silicons are 119.99° and 120.01°, suggesting *sp*²-hybridization along the zig-zag chains. The lowest six bands are primarily *sp*² σ -bonding and one distinct doubly degenerate σ^* band sits slightly above the Fermi energy along *P* – *X*. In other regions of the Brillouin zone, the σ^* band crosses below the Fermi level where it hybridizes with other bands, in particular the Si π^*

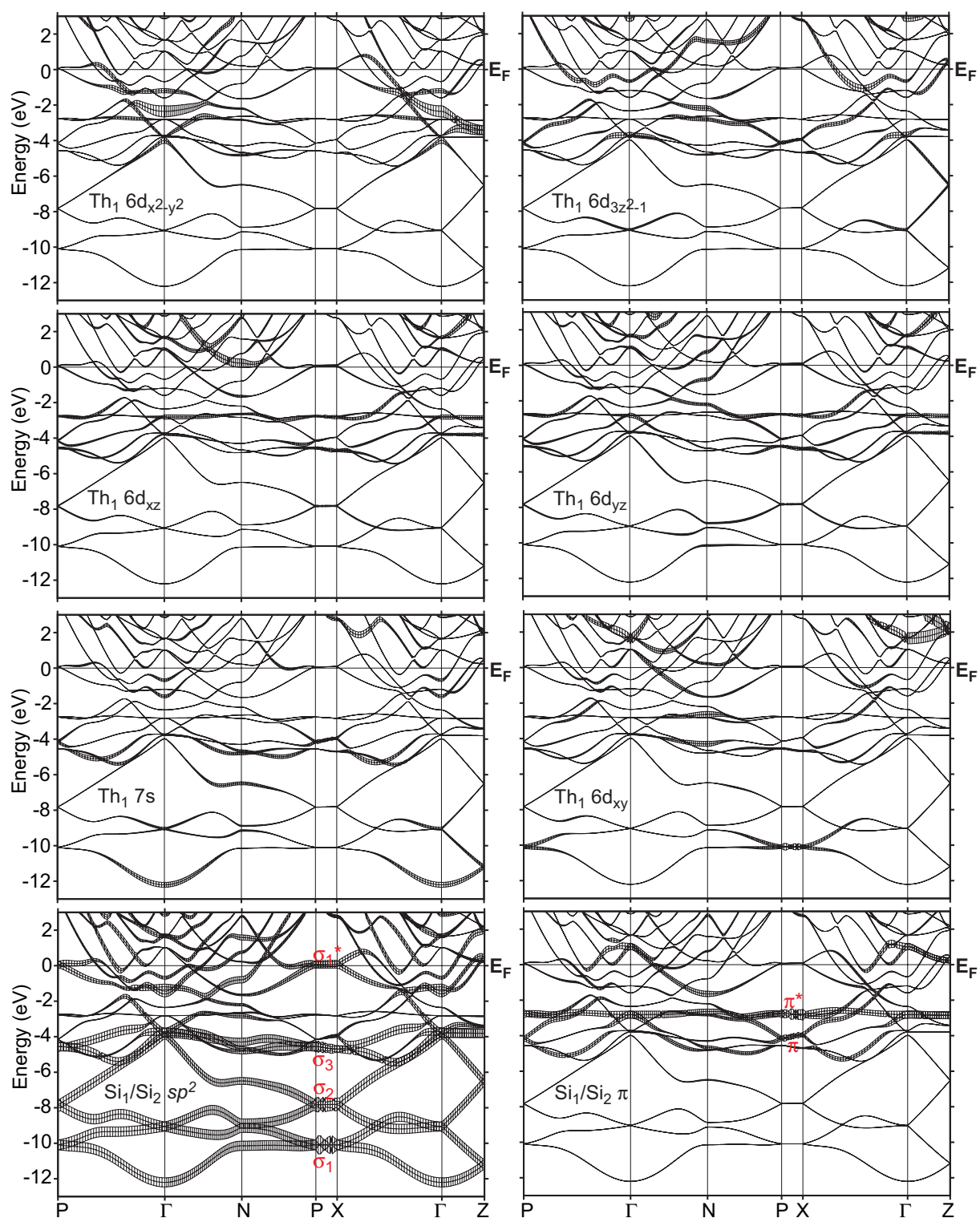


Figure 5.12: Energy bands of α -ThSi₂ with orthogonal LMTO characters (fat bands).

and Th d states. Thus, the sp^2 -bonding bands are full, and the sp^2 anti-bonding bands are partially occupied, in complete agreement with what was previously shown for β -ThSi₂. Four distinct silicon π bands lie almost completely under the Fermi level, suggesting that both the π -bonding and anti-bonding bands are almost full. Only a pocket, somewhat smaller than that for β -ThSi₂, around the Γ -point is empty. The occupied bands exhibit character from all five thorium d orbitals, however it appears that $d_{x^2-y^2}$ character is predominant. The similarities in the densities of states and the fat bands for the two allotropes indicates that the chemical bonding in α -ThSi₂ may be understood by a similar analysis as was presented for β -ThSi₂.

5.3.4 NMTO Wannier-like Functions for α -ThSi₂

In Sec. 5.3.2 it was shown that the three σ -bonding bands in β -ThSi₂ were almost perfectly described by an sp^2 basis on every second silicon atom. For α -ThSi₂ the NMTOs which span the six σ -bands are the s and p_z on Si₁ and Si₄, the p_x on Si₁ and the p_y on Si₄. Fig. 5.13 gives a comparison between the bands calculated using this minimal basis (red) with those calculated

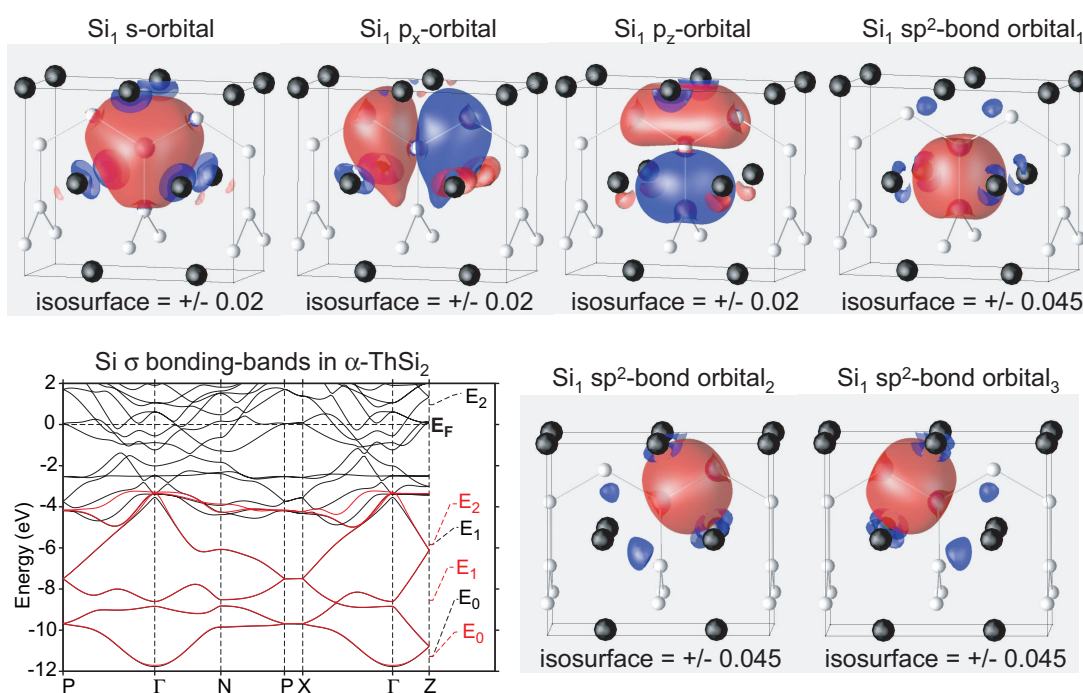


Figure 5.13: The band structure of α -ThSi₂ calculated with a full (spd on Si, sd on Th) basis set in black. The red bands have been obtained with a σ -bonding basis set (s , p_x , p_z NMTO on Si₁ and an s , p_y and p_z NMTO on Si₄). Also shown are the three Si₁-centered NMTOs along with the three sp^2 -bond orbitals. The energy meshes used for each calculation are given to the right of the band structure.

using a full basis. The agreement for the five lowest bands is good, however slight deviations for the highest band, at around -5 eV, may be seen. This is a result of hybridization between the silicon sp^2 and π -bands which occurs due to the z -connections between the zig-zag chains running in the x and y directions. For example, the Si₄ p_y orbital interacts not only with the Si₃ p_y but also with the Si₂ p_y . This is in contrast to the lack of such hybridization in β -ThSi₂. Also given are the three s , p_x and p_y Wannier-like functions on Si₁ along with the three sp^2 bond-orbitals obtained from symmetrical orthonormalization of these NMTOs. The bond orbital pointing in the z -direction is not equivalent to the other two due to the fact that the silicon-silicon bond lengths are not exactly the same. The orbitals display tails on the Th atoms, in-line with the fat bands which revealed that the lowest six bands also contained some thorium s and d character. They are quite similar to those for β -ThSi₂ in Fig. 5.6.

It is not possible to calculate a Wannier-like function which describes only the lower π -bonding band, as was done for β -ThSi₂ in Fig. 5.7, due to the fact that it hybridizes with the uppermost σ -bonding band. It is on the other hand possible to construct a basis for the σ and π -bonding bands, as Fig. 5.14 demonstrates. Now, all six of the lowest sp^2 -bands are identical, on the scale of the figure, to those obtained with a full basis set. Since the π -bands overlap with others, an energy mesh spanning the whole range of the bands could not be used. Therefore, the downfolded π -bands deviate slightly from the black bands in Fig. 5.14. The π -bonding NMTO is very similar to that obtained for β -ThSi₂ in Fig. 5.7. Hybridization with the six nearest neighbour thorium atoms is evident in the d -like tails and is in-line with the fat bands which show regions of hybridization with for example, the Th d_{z^2} band along $P - X - \Gamma$ and

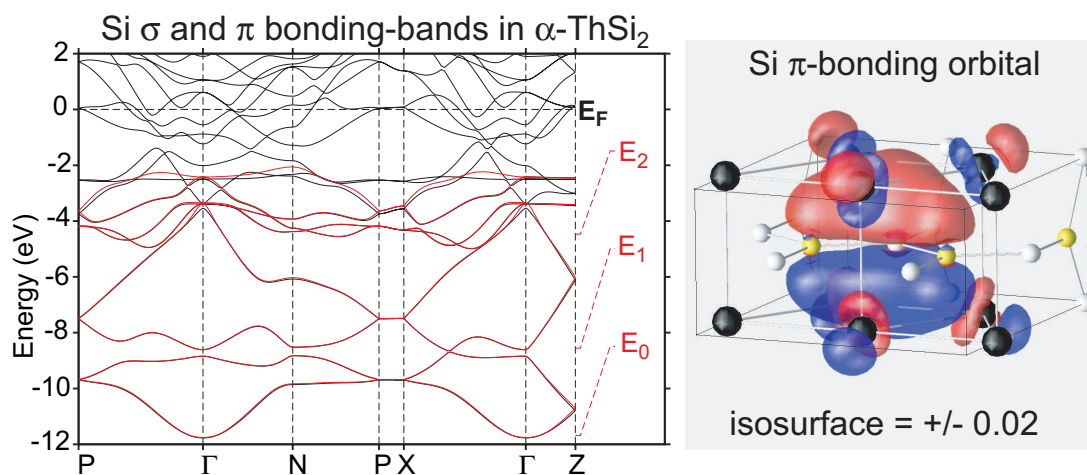


Figure 5.14: The black bands are the same as in Fig. 5.13. The red bands have been obtained with a σ and π -bonding basis set (s , p_x , p_y and p_z NMTO on the white silicon atoms, which are Si₁ and Si₄). Also shown is the π -bonding NMTO.

the Th s band along $\Gamma - N - P - X$. Thus, in analogy with β -ThSi₂, it can be shown that the Si π -bonding band is full and that it hybridizes with the s and d orbitals on the nearest neighbour thorium atoms. In contrast to β -ThSi₂, it also hybridizes with the highest lying Si σ -bonding band.

It was not possible to choose an appropriate energy mesh which spanned just the s^*/π^* bands due to the fact that the s^* bands overlap with the π . Thus a calculation similar to that performed for β -ThSi₂ in Fig. 5.8, could not be done. However, in analogy to β -ThSi₂, we have constructed a truly minimal basis consisting of the Si σ and π -bonding and the Si π^* and s^* anti-bonding orbitals for α -ThSi₂. Fig. 5.15 shows that this basis describes most of the occupied bands quite well. Again, it is surprising that even the bands displaying primarily Th $d_{x^2-y^2}$ character are reproduced accurately by a basis which does not contain thorium centered orbitals. Provided that the situation is the same throughout the Brillouin zone, the agreement between the full and downfolded band structures is somewhat worse for α -ThSi₂ than for β -ThSi₂, especially around the Γ -point where the truly minimal basis picks the π^* bands above, and does not adequately describe the σ^* bands below, the Fermi level. It is not clear whether a supercell approach would improve agreement between the two band structures, since the π^* bands are degenerate and the σ^* bands are non-degenerate at Γ .

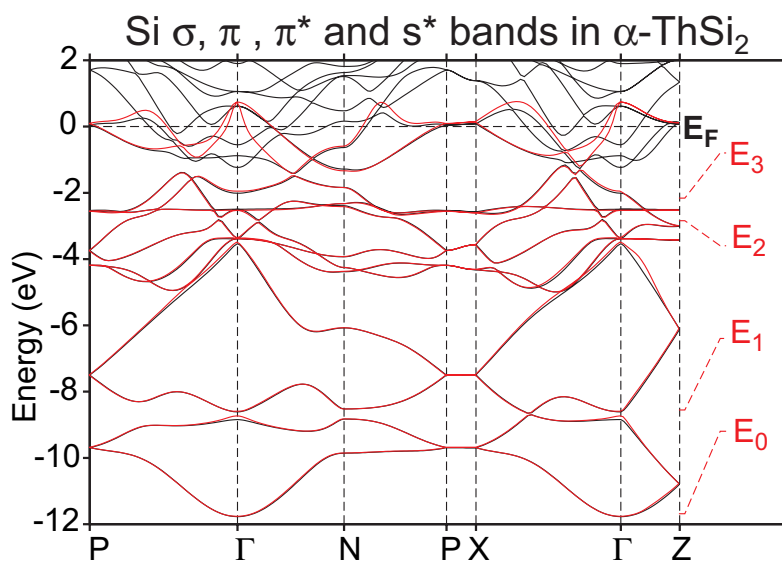


Figure 5.15: The black bands are the same as in Fig. 5.13. The red bands have been calculated with a σ , π , π^* , s^* basis set (s , p_x , p_y and p_z orbitals on Si₁ and Si₄, s , p_x orbital on Si₂ and an s , p_y orbital on Si₃).

In complete agreement with the results for β -ThSi₂, the individual sp^2 orbitals and the σ -bonding NMTOs calculated with the truly minimal basis (Fig. 5.16) display larger tails on

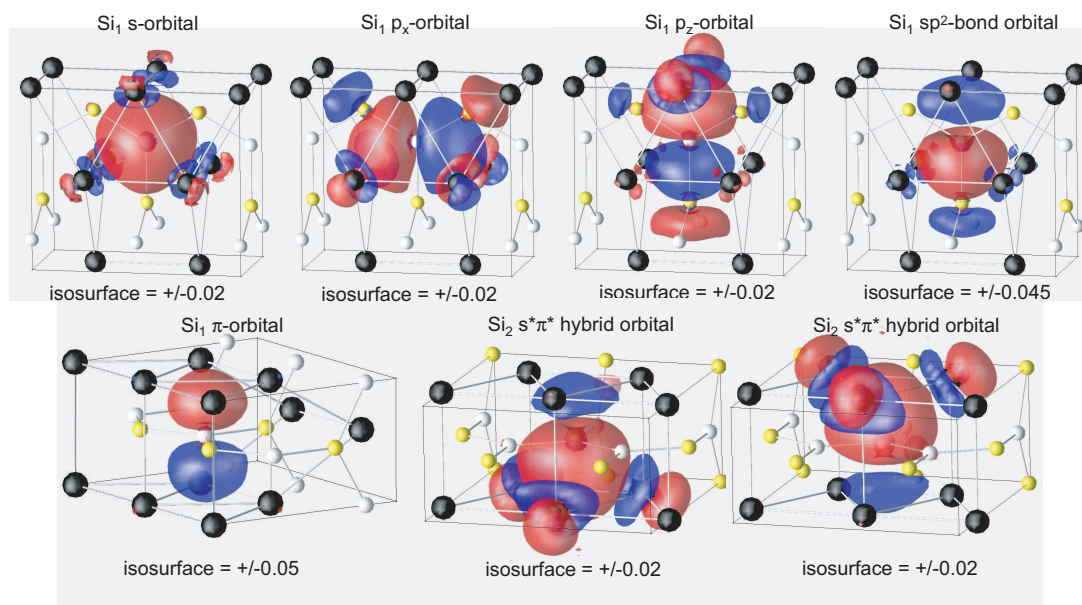


Figure 5.16: The s , p_x and p_z NMTOs, along with one of the three σ -bonding orbitals, the π non-bonding orbital and the two congruent $s^*\pi^*$ hybrids obtained from the downfolded (red) band structure in Fig. 5.15. A σ/π and a s^*/π^* basis was placed on the white and yellow silicon atoms, respectively.

the neighbouring silicon atoms than those obtained using only a σ basis (Fig. 5.13). In fact, they appear very similar to those for β -ThSi₂ in Fig. 5.10. The same holds true for the two $s^*\pi^*$ hybrids which point between the triangular faces in the thorium sublattice. For α -ThSi₂ these faces lie in the yz and xz plane, whereas for β -ThSi₂ they are found in the xy plane. It thus becomes clear why the major thorium contribution to the fat bands is the $d_{x^2-y^2}$ and d_{z^2} orbitals for α -ThSi₂ and β -ThSi₂, respectively. In both cases, Th d_{z^2} -like orbitals point towards the silicons and bond with the larger lobe of the $s^*\pi^*$ hybrids, however they are located along different axes for the two structures.

In conclusion, we have used the NMTO method to show that the bonding in α -ThSi₂ and β -ThSi₂ can be understood in the same manner. The lowest bands arise due to σ -bonding between atoms in the silicon sublattice and the Si π bands are full. The highest bands result from Si $s^*\pi^*$ hybrid orbitals which bond strongly to Th d_{z^2} orbitals lying on the triangular faces above and below the silicon atoms. Within the next section we will consider an alternative interpretation of the bonding in α -ThSi₂, based upon its structural similarity with Cs-IV.

5.3.5 Comparison of α -ThSi₂ and Cs-IV

Cs-IV and α -ThSi₂ have the same space group, with the thorium and cesium atoms located in equivalent positions. Band structure calculations have revealed that for both structures the maximum of electron density is found along the zig-zag chains which correspond to the positions of the silicon atoms in α -ThSi₂. The analysis presented in Sec. 5.3.4 shows that the bonding in α -ThSi₂ can be explained in the same fashion as that in β -ThSi₂, however it does not display any obvious connection to Cs-IV. In Sec. 4.3.4, we have constructed a truly minimal basis for Cs-IV by placing an s NMTO on every second cesium atom, and letting the method shape the orbital accordingly. Examination of the orbital, given in Fig. 4.14, revealed a high degree of sd -hybridization. It consisted primarily of two lobes which pointed towards the regions of maximum electron density and yielded a density in-line with that obtained from standard LMTO calculations. The fat bands for α -ThSi₂ also show a mixture of Th s and d character, suggesting that perhaps a similar approach may be used.

From the analysis presented in Sec. 5.3.4 it is obvious that the six σ -bonding bands in α -ThSi₂ are full and the four π -bands (bonding and anti-bonding) are almost full. This yields ten bands which may be filled with twenty valence electrons. Placing an s orbital on every thorium atom leads to a Th $6s^2$ Si $3s^2 3p^3$ (Si⁻/Th²⁺) electronic configuration. This basis differs from that used for Cs-IV since now an s -like orbital is centered on *every* thorium atom. The band structure calculated using a Si σ , π/π^* , Th s/s^* basis, along with the thorium s -like orbital is shown in Fig. 5.17. Provided that the situation is similar throughout the whole Brillouin zone, it does only a slightly worse job in describing just the occupied bands than the truly minimal basis in Fig. 5.15. Previously it was shown that the shape of the orbital is more robust than the bands. For example, for bcc Cs, even small supercells were found to reproduce the rough shape of the orbital obtained from large ones, see Sec. 4.3.4. Thus, we do not expect that better agreement between the two sets of bands will affect the orbital nor the interpretation substantially.

The basis yields three Si σ -bonding NMTOs, very similar to those shown in Fig. 5.13, however they are once again not completely symmetric with respect to the crystal lattice since our choice of orbitals has specifically broken the symmetry of the system. It also yields a π non-bonding orbital, similar to that shown for graphite in Fig. 3.1, on every silicon atom. Finally, a thorium s -like non-bonding orbital on every thorium atom, shown in Fig. 5.17, is obtained. It spreads out onto those nearest neighbour silicons where the sp^2 -orbitals have been downfolded and is symmetry breaking and not maximally localized. As we have shown in Sec. 3.2.1, it is possible to achieve maximal localization and to restore the symmetry of the system, however this feature is currently not implemented in the present version of the program. Future work should focus on this issue, since it will help to distinguish if the results obtained have a chemical significance or if they are just artifacts of the calculation. Clearly, the orbital shows sd hybridization and appears to be similar to half of the Cs-IV Wannier-like function in Fig.

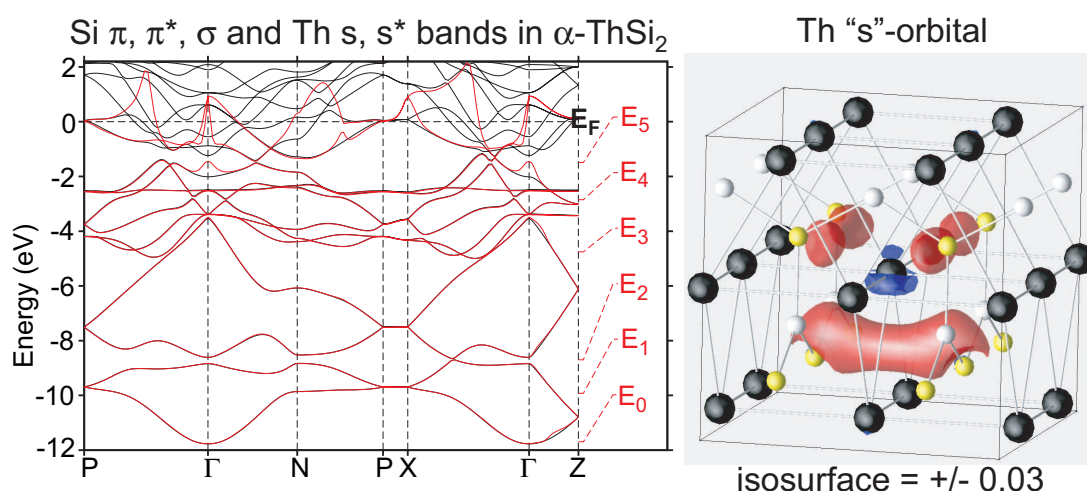


Figure 5.17: The black bands are the same as in Fig. 5.13. The red bands have been calculated with a Si σ , π , π^* , and Th s , s^* basis (s , p_x , p_y , p_z orbitals on Si₁ and Si₄, p_x orbital on Si₂, p_y orbital on Si₃ and an s orbital on every Th atom). The sp^2 -orbitals were placed on the white silicon atoms. Also shown is the s -like orbital on the central thorium atom.

4.14. It contains one and not two lobes which are directed along the center of the prisms and point towards the silicons. However, now we have two electrons per Th whereas previously we had one electron per Cs.

Fig. 5.18 illustrates the charge density of α -ThSi₂ decomposed into contributions arising from the different sets of NMTOs obtained using the truly minimal basis in Fig. 5.17. Clearly, the density obtained from the σ -bonding orbitals is not symmetric with respect to the silicons, since those atoms on which an sp^2 basis has been placed (white) have a greater charge density directly surrounding the atom as compared to those where the σ -orbitals have been downfolded (yellow). The π non-bonding orbitals yield a density which is almost identical for the two types of silicon atoms, however at the isosurface chosen the lobes on two white atoms separated by a translation in the x or y direction just touch, whereas those of the yellow silicons do not. Interestingly, the density obtained from the thorium s -like non-bonding orbital has a maximum around the yellow silicons and very little density surrounding the thoriums. Moreover, the regions of high electron density are perpendicular to those in Fig. 4.14 for Cs-IV. This excess of charge around the silicons where the sp^2 -orbitals have been downfolded, compensates for the deficiency of charge which was seen in the density arising from the σ -bonding orbitals, so that when all of the contributions are summed, the density is nearly symmetric with respect to the crystal lattice. The dissymmetry in the densities shown in Fig. 5.18 (a)-(d) does not have any chemical significance and is an artifact of the method which arises due to breaking the

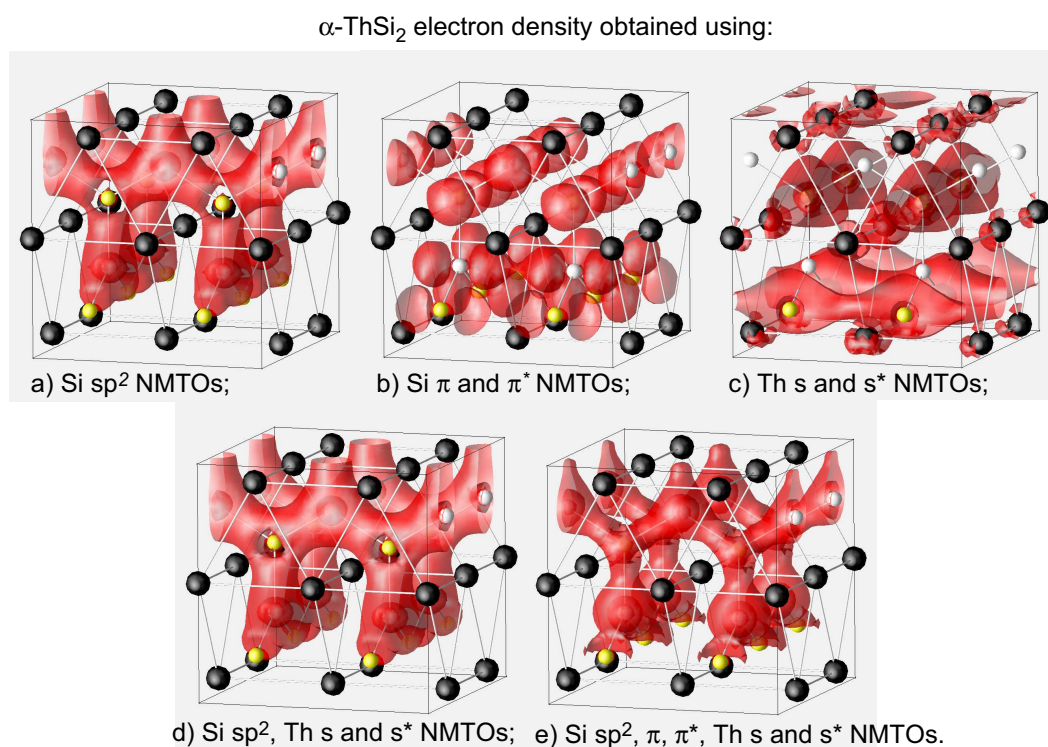


Figure 5.18: The charge density of α -ThSi₂ obtained by: (a) placing the σ -bonding orbitals on each white silicon atom and squaring them; (b) placing a π non-bonding orbital on each silicon atom and squaring it; (c) placing a thorium s -like non-bonding orbital on each thorium atom and squaring it; (d) sum of (a) and (c); (e) sum of (a), (b) and (c). The orbitals used were obtained from the truly minimal basis employed in Fig. 5.17. The isosurfaces were taken as 0.014, 0.007, 0.002, 0.014 and $0.023 a_B^{-3}$, respectively. The corresponding TB-LMTO charge density calculated in the conventional way by summing over all Bloch states is given in Fig. 5.2.

symmetry in the choice of the basis. The total density obtained from the N MTOs is very similar to that calculated by TB-LMTO in Fig. 5.2. Thus, despite the fact that the orbitals obtained may break the symmetry of the system, we have shown that they yield a charge density in-line with that obtained from standard electronic structure calculations.

We have also considered a symmetric basis which is not truly minimal, that is it contains more basis functions than occupied bands. Specifically, it consists of Si σ/σ^* , Si π/π^* and Th s/s^* N MTOs. It differs from that used in Fig. 5.17, since we have added the Si σ^* orbitals to the basis. The bands and orbitals obtained from this calculation are given in Fig. 5.19. The two band structures are identical, on the scale of the figure, up until around 1.5 eV and the

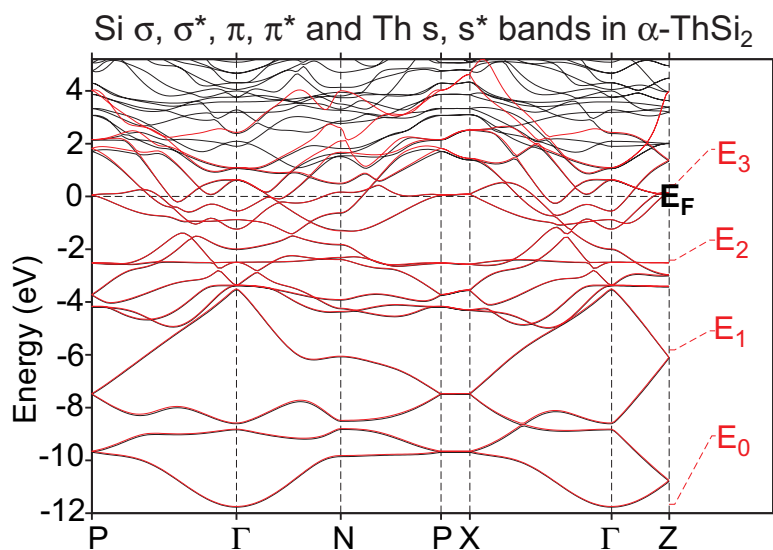
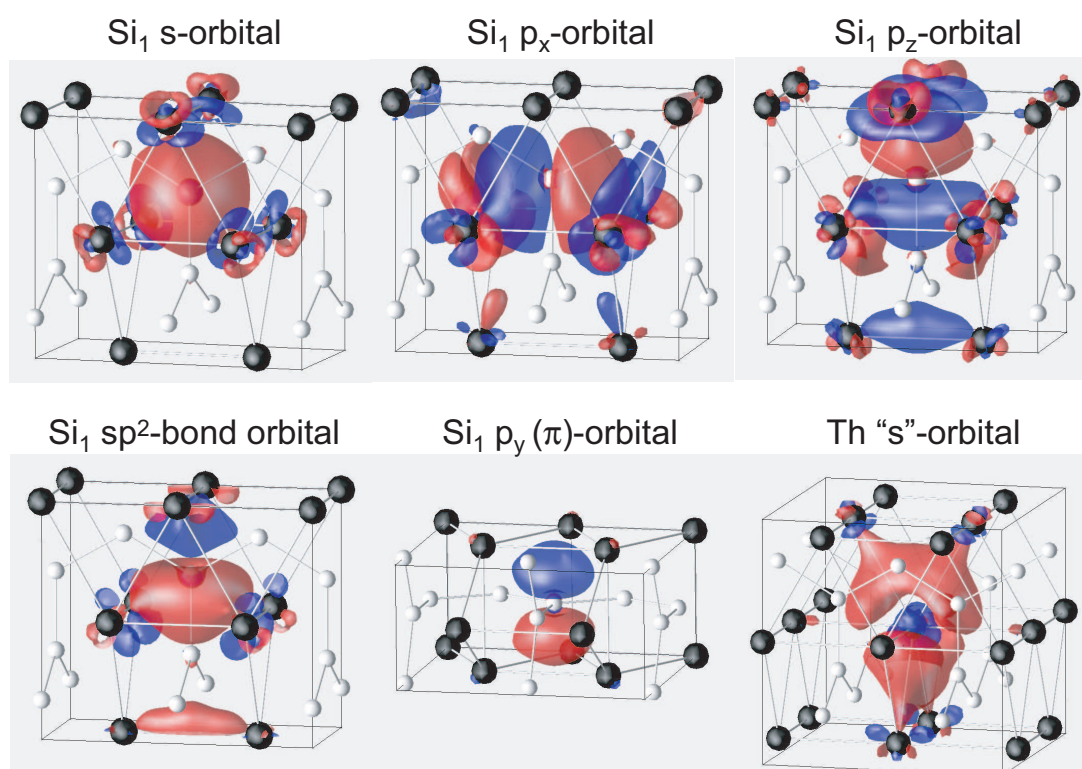


Figure 5.19: The black bands are the same as in Fig. 5.13. The red bands have been calculated with an Si σ , σ^* , π , π^* and Th s , s^* basis (s , p_x , p_y , p_z orbital on every silicon and an s orbital on every thorium atom). This yields a symmetric, minimal basis. The orbitals are shown for the following isosurface values: ± 0.02 (s , p_x , p_z), ± 0.045 (sp^2 -orbital), ± 0.05 (p_y) and ± 0.03 (Th s -like orbital).

downfolded bands reproduce all of the occupied ones accurately. At the isosurface chosen, the π -orbital appears similar to that obtained with the truly minimal basis. However, the σ and thorium s -like orbitals differ from those calculated using the basis in Fig. 5.17, in particular since they now retain the symmetry of the crystal lattice.

The NMTO fat-bands for the Si σ , Si π/π^* , Th s/s^* and the Si σ/σ^* , Si π/π^* , Th s/s^* basis sets have been calculated and are given in Fig. 5.20. The fatness arising from the π -bands is similar for both, in agreement with the observation that the π -orbitals appear to be identical. Moreover, in both calculations the π -bands are nearly full. A comparison of the smaller and larger basis reveals that in the former the fatness from the thorium s -orbital is found

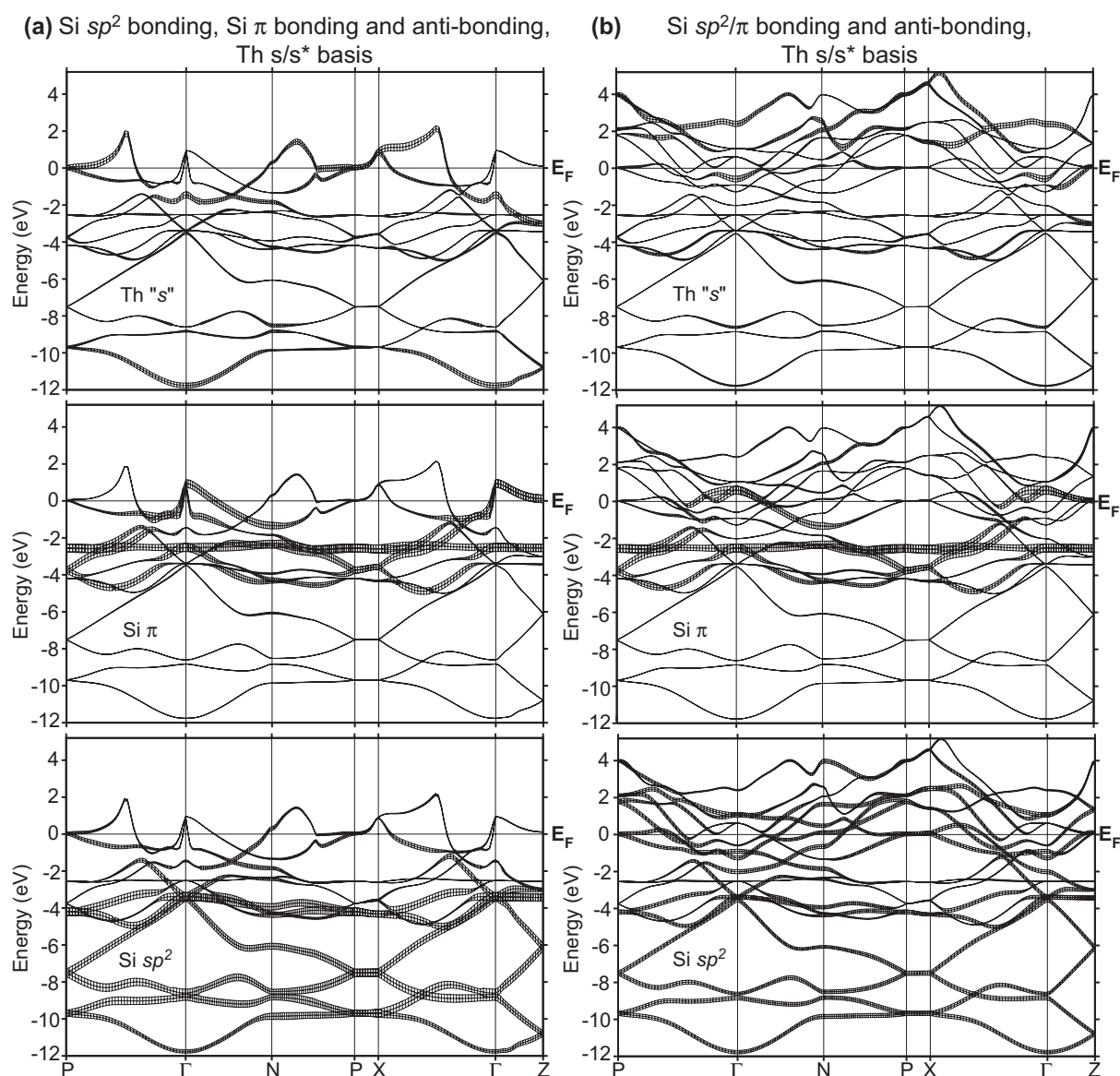


Figure 5.20: Energy bands of α -ThSi₂ with orthogonal NMTO characters (fat bands).

mostly in the occupied bands and in the latter it is situated primarily in the unoccupied bands. This implies that the sp^2 orbitals of the larger basis exhibit character which was attributed to the thorium orbitals in the smaller basis. Along $\Gamma - N$ and $\Gamma - Z$ fatness arising from the thorium s orbital splits into bands below and above the Fermi level for the larger basis. These bands also reveal sp^2 -character indicating that Th s - Si σ^* hybridization is at least partially responsible for the stability of the system. In Sec. 4.3.5 it was shown that the stability of Cs-IV could be attributed to the splitting of the xz/yz bands near the N -point. The Bloch functions at N for the occupied and unoccupied bands differed primarily in that they displayed $dd\delta\pi$ -bonding/anti-bonding interactions, respectively, along the zig-zag regions of maximum electron density (silicon positions in α -ThSi₂).

The bandwidth for the occupied bands in Cs-IV is approximately 1.8 eV, whereas the occupied silicon sp^2 and π bands have a spread of around 13 eV, indicating that the bonding in Cs-IV and the silicon sublattice is very different. However, the bandwidth of the thorium bands is about 3 eV, suggesting a greater similarity with cesium. Indeed, both elements occupy the same positions in the unit cell and for both the fat bands revealed s and d character under the Fermi level. Moreover, it was possible to describe both sets of bands via an s -like NMTO. Since cesium has one valence s electron, this orbital was placed on every second atom in Cs-IV. As we have shown earlier, the thorium atoms in α -ThSi₂ have a valence electronic $6s^2$ configuration so it was necessary to place an orbital on every atom. For the truly minimal basis set describing just the occupied bands, the cesium and thorium NMTOs displayed two and one lobe, respectively, directed along the center of the prisms. Thus, the Th s -like orbital appears to be similar to half of a Cs-IV s -like orbital. However, the former is not symmetrical with respect to the lattice and it is difficult to determine what a maximally-localized NMTO would look like without performing explicit calculations. Perhaps future work could help to clarify this point. The Wannier-like orbital for Cs-IV consisted primarily of two lobes describing two electrons and thus each lobe could be associated with a single electron (a small amount of the orbital was located around the central and nearest neighbour cesium atoms). These lobes were not found in the same positions as the silicon atoms in α -ThSi₂ but instead pointed towards them. From this it can be concluded that Cs-IV is an electrone, however the single electron lies between two planes of cesium atoms and not on the interstitial Wyckoff 8e sites, (positions of the silicon atoms in α -ThSi₂) as was suggested by von Schnering and Nesper.⁷⁵

5.4 Summary and Conclusions

Within this chapter we have shown that the NMTO method can be used to generate Wannier-like functions for a band, or groups of bands. These orbitals can be useful to gain a chemical understanding of bonding in the solid state. It is even possible to apply the method to study a

metallic or inter-metallic system and to generate a truly minimal basis set which describes most of the occupied bands accurately. The current version of the program may yield orbitals which are symmetry breaking and it would be useful to implement a maximal localization scheme which restores the symmetry of the system.

The method has been specifically applied to α -ThSi₂ and β -ThSi₂. The analysis revealed that bonding in both systems can be understood in a similar way. The bands lowest in energy arise from σ -bonding within the silicon sublattice. Since the unit cells consist of one and two formula units for β -ThSi₂ and α -ThSi₂, the σ -bonding bands contain six and twelve electrons, respectively. Another two (β -ThSi₂) and four (α -ThSi₂) electrons are found within the filled π -bonding bands. Both of these sets of orbitals hybridize slightly with the s and d orbitals on the nearest neighbour thorium atoms. The remaining four and eight valence electrons, in β -ThSi₂ and α -ThSi₂, are located within Si $s^*\pi^*$ orbitals which hybridize strongly with the thorium atoms. Specifically, the lobes of the Th d_{z^2} orbitals point towards the silicon atoms and form a bonding interaction with the Si $s^*\pi^*$ hybrids. The occupied bands were quite well reproduced by a Si σ , π , π^* and s^* basis.

Another interpretation of the bonding in α -ThSi₂, based upon the analysis presented for Cs-IV in Sec. 4.3.4, was also considered. A truly minimal basis composed of Si σ , π , π^* and Th s , s^* orbitals gave quite good agreement with the band structure calculated using a full basis set. Comparison of the occupied silicon bands in α -ThSi₂ with the band structure of Cs-IV revealed that the two had very different energy scales. The energy range of the occupied Cs-IV bands was, on the other hand, more similar to that of the thorium bands and the Wannier-like orbitals obtained for both metals also resembled each other showing a high degree of sd hybridization. In particular, the Th s -like orbital contained one lobe pointing along the center of the prisms, whereas the Cs-IV s -like orbital consisted primarily of two such lobes. However the former is not symmetric with respect to the lattice and the generation of a maximally localized, symmetric orbital is necessary in order to make any definite conclusions. The Wannier-like function for Cs-IV indicated that the compound is indeed an electrone with a single electron lying between two planes of cesium atoms, along the center of the prisms.

Part II

Molecules

Chapter 6

The ^{13}C NMR Chemical Shifts in (9,0) Carbon SWNTs

6.1 Introduction

The discovery of carbon nanotubes⁷⁷ has sparked intense research activity within the last decade. These novel materials have a wide range of potential applications ranging from the fields of nano-electronics to nano-scale biotechnology. For example they may be used as molecular field-effect transistors,^{78,79} electron field emitters,^{78,80} artificial muscles^{78,81} or even in DNA-sequencing.⁸² The wide horizon of applications stems from the fact that carbon nanotubes may have a diverse range of weights, electronic structures, helicities, etc. Individual classes of tubes exhibit very different physical and chemical properties. From a molecular design perspective, it is important to understand the experimental conditions necessary to produce tubes with a given subset of properties and considerable effort has been placed into determining the parameters affecting the molecular architecture of the tubes.^{80,83-85} Recently, advances in the separation of metallic and semiconducting tubes,^{86,87} as well as tubes with different diameters,⁸⁷ have been made.

One of the reasons why it is so difficult to control the properties of the synthesized tubes is that there is no stand-alone method available by which they may be fully characterized. The length and diameter of an individual tube may be determined by AFM, STM or TEM. If information about the bulk sample is sought then SEM, X-ray diffraction, optical absorption and Raman scattering may be used. Unfortunately, even a combination of the aforementioned techniques does not fully characterize a given sample.⁷⁸

The large decrease in price-to-performance ratio of modern CPUs, along with the implementation of favorably scaling density functional algorithms has recently made it possible to perform quantum-chemical calculations on the electronic structure of large single-walled nanotube (SWNT) fragments.⁸⁸⁻⁹⁴ Most computational solid-state and quantum-chemical studies

of SWNTs have so far focused on geometric and electronic structure as well as mechanical properties. It is of high importance to study electric and magnetic response properties as well, since they are the observables of some of the most powerful and frequently applied spectroscopic methods used for characterizing molecules. Among those, NMR is of high practical importance. Previous theoretical work proposed that separation of metallic from semiconducting SWNTs may be possible using high resolution ^{13}C NMR, based on a predicted 11 ppm difference in their chemical shifts.^{95,96} However, from the computations it was also concluded that NMR could not resolve the structural properties of SWNTs.⁹⁵ Values for the chemical shifts with respect to a standard reference were not reported in Ref. 95 because of neglected terms in the calculated shielding tensors (which were argued to be the same for different nanotube structures). It was indicated that the dependence of the NMR spectra on tube diameter and helicity might be weak among members of the metallic and semiconducting classes, respectively. So far only a few groups have used NMR to study the properties of nanotubes. The main difficulties arise from the large magnetic inhomogeneity in the samples caused by residual catalyst from the growth process. Before purification and annealing, very broad lines with about 1500 ppm anisotropy are observed.^{96,97} MAS spectra measurements have yielded isotropic shifts of 124 ppm,⁹⁸ 116 ppm⁹⁹ and 126 ppm with side-bands ranging over 300 ppm.^{96,97} Recently, the NMR of functionalized nanotubes in solution have been partially resolved into two overlapping peaks corresponding to semiconducting (128 ppm) and metallic tubes (144 ppm).¹⁰⁰ In all of these experiments, the exact composition of the sample was not determined.

In this chapter, we present the first “molecular” density functional calculations of the ^{13}C NMR chemical shift in SWNTs. We also report the principal components of the shielding tensors and indicate their orientation. Eventually, it will be desirable to perform a systematic study on nanotubes with different diameters, helicities and electronic properties, the results of which could aid experimental characterization of nanotube samples. However, first it is necessary to determine suitable theoretical methods and structural models which must be used in order to obtain meaningful results. We believe that the chemical shift for the (9,0) SWNT reported here might already be useful in order to confirm that the aforementioned experimental estimates for the chemical shifts are within the same range as first-principles theoretical predictions. Within this chapter we will in particular focus on the following two issues:

- Are short SWNT fragments capped with hydrogen atoms good models for the electronic and magnetic response properties of closed SWNTs which are capped with half of a C_{60} fragment?
- How do the the SWNT’s electronic and magnetic properties depend upon the size of the tube? In particular, do these properties converge with increasing tube length, indicating that calculations on finite sized tubes are able to give any insight into a system of infinite length?

6.2 Computational Details

The computations were performed with the Amsterdam Density Functional (ADF) code.^{101,102} In all calculations we have applied the revised Perdew–Burke–Ernzerhof (revPBE) non-hybrid density functional.^{65,103–105} Full geometry optimizations of all SWNT fragments as well as C₆₀ and the NMR reference tetramethylsilane (TMS) were carried out employing a valence triple- ζ Slater-type basis set with polarization functions for all atoms (TZP) from the ADF basis set library. The 1s shells of the carbon atoms were kept frozen for the geometry optimizations. NMR chemical shift calculations were carried out with the all-electron TZP basis set (which is of double- ζ quality for the carbon 1s shells) and the revPBE functional, employing the non-relativistic GIAO (gauge-including atomic orbitals) methodology developed by Schreckenbach and Ziegler^{106–109} as implemented in the “NMR” program of the ADF package. NMR chemical shifts are reported with respect to TMS whose shielding was calculated as being 185.10 ppm at this level. Because of the computational expense for the two largest molecules studied here (the 204 and 222 carbon atom fragments), not all possible chemical shifts from symmetry inequivalent atoms could be calculated. However, a representative subset which includes a number of atoms from the end to the middle of each tube fragment has been considered. We believe that this is sufficient in order to yield conclusions about the trends which are of interest here. For the other systems, the chemical shifts for all symmetry inequivalent carbons were calculated. In order to assess the accuracy of our results, calculations with various basis sets and another functional were performed on a subset of systems studied here. The results of these calculations are discussed in Sec. 6.3.2.

Due to the fact that ADF does not support D_{9h}/D_{9d} symmetry, calculations on the hydrogen-capped tubes were carried out in the D_{3h}/D_{3d} subgroups. This also facilitates comparisons with the C₃₀-capped SWNT fragments. For the C₃₀-capped tubes D_{3h}/D_{3d} symmetry was employed with the exception of one D_3 tube which was considered for comparison. For both the smallest hydrogen and C₃₀-capped SWNT fragments single-point calculations without symmetry constraints were also performed. Within the numerical accuracy of the computations, the results showed identical orbital occupancies, orbital energies and total energies to those using symmetry constraints. However, the calculations without symmetry needed a larger number of SCF cycles in order to reach charge density convergence.

The authors of Ref. 88 have applied a correction to the HOMO–LUMO energy difference when reporting estimated band gaps for the (5,5) and the (9,0) SWNTs. The correction was obtained from considering Koopmans’ theorem for the C₆₀ fullerene, under the assumption that errors of similar magnitudes may be present for the C₃₀-capped SWNTs. The average of available experimental values for the IP of C₆₀ is 7.56 eV,^{110–113} the average of experimentally determined EAs is 2.68 eV.^{114,115} Our calculated orbital energies of 6.05 eV (HOMO) and 4.40 eV (LUMO) are of similar magnitude as the 6.40 and 3.66 eV, respectively, from the DFT

(B3LYP hybrid functional) calculations in Ref. 88. If calculated HOMO–LUMO gaps are to be identified with $\text{IP} - \text{EA}$ and with the band gap of the SWNT it is seen that the calculated value for C_{60} is too large. Correction terms of 1.51 eV and -1.72 eV might therefore be added to the HOMO and LUMO energies, as was done previously in Ref. 88. However, it was noted there that such a correction leads to a clear overestimation of the band gap. For DFT calculations, the HOMO–LUMO gap serves as a zeroth–order estimate of the lowest excitation energy of the system¹¹⁶ rather than $\text{IP} - \text{EA}$ which could explain why the application of the correction term leads to the aforementioned overestimation. For comparison with the results of Ref. 88, in the following both the corrected and uncorrected values are given for the C_{30} –capped SWNTs.

A subset of the graphics were prepared using the XCRYSDEN program.¹¹⁷ The orbital isosurface plots were created with the program MOLEKEL.¹¹⁸ Fig. 6.8 was prepared using MATHEMATICA.

6.3 Results and Discussion

6.3.1 The Electronic Structure of (9,0) SWNTs

A SWNT can be constructed from the rolling of a graphene sheet. It can be uniquely classified by a vector, or more conveniently a pair of numbers (n_1, n_2) , connecting the two points which meet upon rolling. This results in three classes of tubes: armchair, zig-zag and helical (chiral) characterized by (n, n) , $(n, 0)$, (n_1, n_2) , respectively. Early tight-binding calculations on a graphene sheet model showed that SWNTs should exhibit metallic characteristics if and only if:

$$n_1 - n_2 = 3q, \quad (6.1)$$

where q is an integer.^{119,120} However, models which considered hybridization between π -orbitals perpendicular to the tube's surface and sp^2 - σ orbitals, showed that tubes satisfying Eq. (6.1), but for which $n_1 \neq n_2$, were found to be narrow-gap semiconductors.^{119–121} The band gap was predicted to decrease as the diameter of the tube increased, due to the reduction of hybridization.^{119,120} Tubes for which $n_1 = n_2$, were found to be metallic due to symmetry.^{119–122} Hybridization between σ^* and π^* orbitals has also been shown to have an effect on the electronic structure of small-radius nanotubes.¹²³ Low temperature STM investigations revealed band gaps of 0.080 ± 0.005 , 0.042 ± 0.004 and 0.029 ± 0.004 eV for the (9,0), (12,0) and (15,0) SWNTs, respectively.¹²⁴ In a recent paper studying the electronic structure of (9,0) and (5,5) SWNTs capped by half of a fullerene, Cioslowski and co-workers showed that the former have a finite HOMO-LUMO gap which appears to converge well with increasing tube length.⁸⁸ These results have been confirmed by another group.⁹⁰

Due to the absence of periodic boundary conditions in molecular calculations, it is necessary

to saturate the carbon dangling bonds in the nanotube fragments. Often, hydrogen is assumed to be a good choice.^{89,93,94,125} Each ring segment of the (9,0) tube is made up of 18 atoms and therefore such hydrogen-capped tube fragments consisting of N segments contain $18N$ carbon atoms. This results in fragments with D_{9h} or D_{9d} symmetry for even and odd N , respectively. The HOMO-LUMO gaps and difference between HOMO-LUMO gaps for successively larger fragments of the hydrogen-capped tubes are presented in Fig. 6.1(a) and 6.1(b). The number of atoms given along the abscissa also includes the capping hydrogens, thus $N = (\text{number of atoms})/18 - 1$. The symmetry of the tubes changes with increasing N and we have indicated in Fig. 6.1 (b) the differences for each symmetry separately. They are either given by

$$\Delta\Delta E_{D_{9h}} = \Delta E(D_{9h}) - \Delta E(\text{next shorter fragment of } D_{9d} \text{ symmetry}) \quad , \quad (6.2)$$

or by

$$\Delta\Delta E_{D_{9d}} = \Delta E(D_{9d}) - \Delta E(\text{next shorter fragment of } D_{9h} \text{ symmetry}) \quad . \quad (6.3)$$

A hydrogen-capped (9,0) tube is predicted to be metallic starting with $N \approx 6$. This result appears to be well converged with respect to the length of the SWNT studied here. The HOMOs and LUMOs for the H-capped SWNT fragments are found to be of E symmetry and therefore doubly degenerate. This agrees with previous calculations on hydrogen capped $(n, 0)$ tubes showing that $n = 6, 8, 10$ afforded nondegenerate and $n = 7, 9, 11$ yielded doubly degenerate HOMOs and LUMOs.¹²⁵

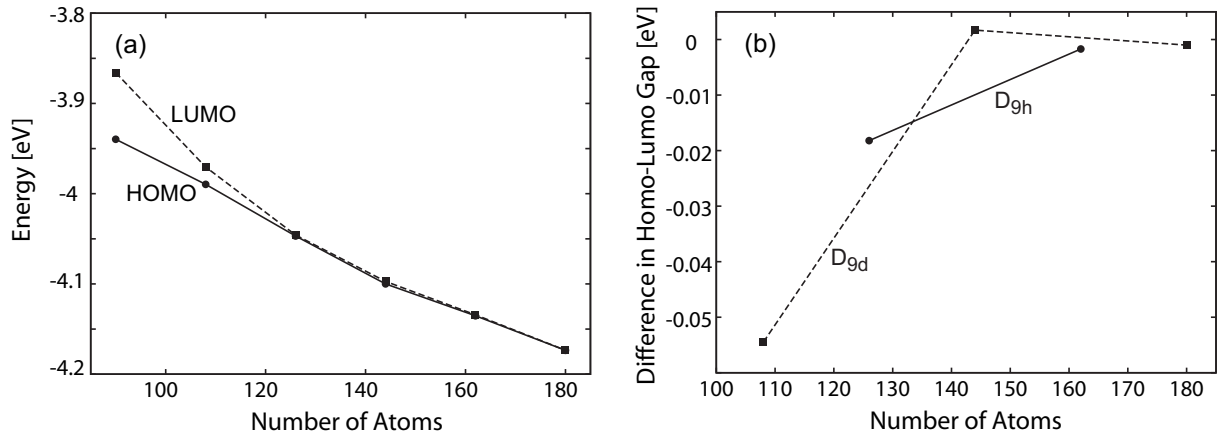


Figure 6.1: (a) The HOMO-LUMO energies, and (b) the difference between successive HOMO-LUMO gaps in hydrogen-capped D_{9h}/D_{9d} (9,0) SWNTs. The lines do not represent a fit to the data but were added to guide the eye. See also Eqs. (6.2), (6.3). The total number of atoms in the tube is given along the abscissa.

It is also possible to cap a (9,0) zig-zag SWNT with half of a C_{60} fullerene, yielding two sets of C_{60+18j} tubes.^{88,126} In the first set even/odd j gives D_{3d}/D_{3h} symmetry. Rotation of one of

the C_{30} caps by 40 degrees produces members from the second set which possess D_3 symmetry. It has previously been shown that the members of the former are energetically more stable and have larger HOMO-LUMO gaps than those of the latter⁸⁸ and therefore the focus of this study is on SWNTs possessing D_{3d}/D_{3h} symmetry. The HOMO-LUMO gaps and difference between HOMO-LUMO gaps for successively larger C_{30} -capped tubes are displayed in Fig. 6.2 (a) and 6.2 (b). The uncorrected HOMO-LUMO gaps are approximately half the size which were previously calculated using the B3LYP functional.^{88,90} The corrected ones are approximately 1.1 times larger than those reported in previous work,⁸⁸ due to the fact that the computational methodology employed here produced a smaller HOMO-LUMO gap for C_{60} and therefore a larger correction was added. These differences are not surprising since it is known that for many compounds containing C, H, N, O, the B3LYP hybrid functional applied in Ref. 88 results in HOMO-LUMO gaps which are larger than those calculated with non-hybrid density functionals such as the one applied here (revPBE). Regardless of the addition of a correction term, the results are seen to converge to a finite HOMO-LUMO gap. This can be seen most clearly in Fig. 6.2 (b) which shows that the difference between successive HOMO-LUMO gaps, $\Delta\Delta E$, approaches zero with increasing length of the tube. The symmetry of the tubes changes with increasing j which leads to an oscillatory behavior of the HOMO-LUMO gap when comparing SWNT fragments of different symmetry. In order to avoid this we have indicated in Fig. 6.2 (b) the differences for each symmetry separately. These $\Delta\Delta E$ values converge rapidly to zero without displaying further oscillatory behavior. A rough estimate of the lengths of the tubes for which $\Delta\Delta E_{D_{3h}}$ and $\Delta\Delta E_{D_{3d}}$ approach zero was obtained through a linear fit of the two sets

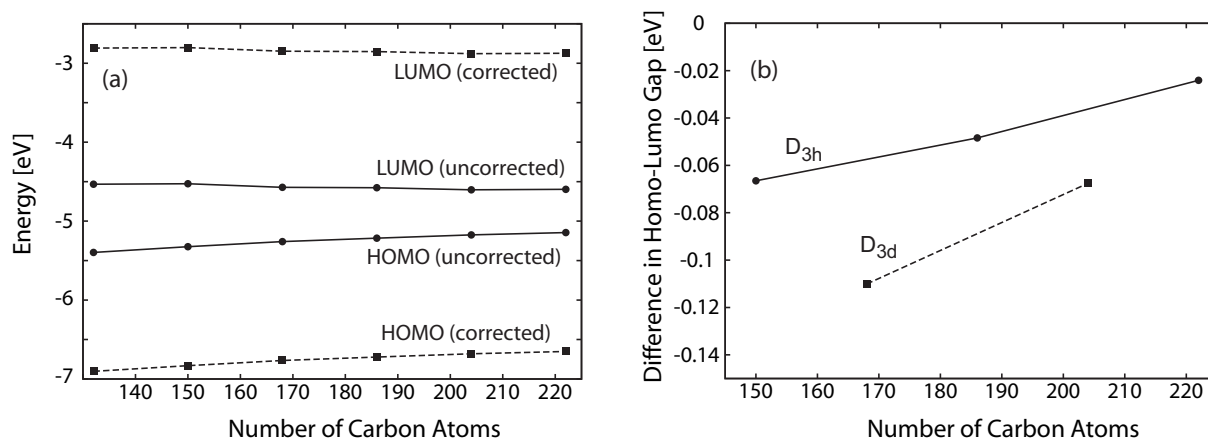


Figure 6.2: (a) The HOMO-LUMO energies, and (b) the difference between successive HOMO-LUMO gaps in C_{30} -capped D_{3h}/D_{3d} (9,0) SWNT fragments. The lines do not represent a fit to the data but were added to guide the eye. See also Eqs. (6.2), (6.3), but with D_{9h}/D_{9d} replaced by D_{3h}/D_{3d} . The total number of atoms in the tube is given along the abscissa.

of $\Delta\Delta E$ s and extrapolation to $\Delta\Delta E = 0$. The first series is predicted to converge at ≈ 276 and the second at ≈ 312 carbon atoms. It must also be noted that the HOMOs and LUMOs of these species are spatially non-degenerate, unlike the frontier orbitals for the H-capped SWNT fragments.

The results indicate that hydrogen-capped (9,0) SWNT fragments are metallic, whereas ones capped with a C_{30} hemisphere are small-gap semiconductors. Moreover, the HOMOs and LUMOs of the former are doubly degenerate whereas those of the latter are non-degenerate. These findings clearly indicate that in this case *a hydrogen-capped tube is not a good model for a C_{30} -capped tube*. It is also not a good model for an infinite tube which is predicted to be a small-gap semiconductor by band structure calculations^{119-121,123} and experimental measurements.¹²⁴

For the D_{3d}/D_{3h} C_{30} -capped tubes the HOMOs are of A_{1u}/A_1'' symmetry and the LUMOs are of A_{2u}/A_2'' symmetry. For the D_{9h} hydrogen-capped tubes which were calculated in D_{3h} symmetry, these frontier orbitals have either E_1' or E_1'' symmetry. For the D_{9d} hydrogen capped tubes which were calculated in D_{3d} symmetry, they are of either E_{1u} or E_{1g} symmetry. Due to the fact that these orbitals are so close in energy, the order of their population is sometimes reversed. Band structure calculations which did not take into account σ - π hybridization and hence predicted metallic behavior for the zig-zag fibers showed that the highest occupied and lowest unoccupied bands were twofold degenerate of E symmetry.¹²⁰

In Figs. 6.3, and 6.4 the HOMOs and LUMOs for the smallest and largest tubes with each capping are presented in the form of isosurface plots. All of these frontier orbitals have carbon π character however in case of the hydrogen-capped SWNTs they are localized at each end of the tube, whereas for the C_{30} -capped SWNTs they are delocalized over the whole fragment. At the same time, it can be seen from Figs. 6.3 (b) and 6.4 (b) that the HOMO-1 of A_{1u} symmetry of the H-capped fragment resembles the HOMO of the C_{30} -capped 222 atom fragment. Since the HOMOs and LUMOs of the H-capped systems are localized at the ends of the fragments it is obvious that they do not represent an occupied orbital of an infinite system. As the length of the fragment increases, these orbitals do not yield a contribution to the electron density along the tube (except at the ends) and must therefore be regarded as artifacts due to treating the finite-sized systems. On the other hand, the HOMOs and LUMOs of the C_{30} -terminated fragments indeed seem to yield a good representation of the infinite systems. We expect that for very long H-capped fragments the HOMO-1 and LUMO+1 shape and energy become similar to the HOMOs and LUMOs of the corresponding C_{30} -capped fragments. It appears that the H-capped SWNTs are not well converged in this respect. Both the (HOMO-1)s and HOMOs of the H-capped fragments have contributions at the tube ends which means that there should be comparatively large Coulomb interactions present between these orbitals which are slowly vanishing with increasing length.

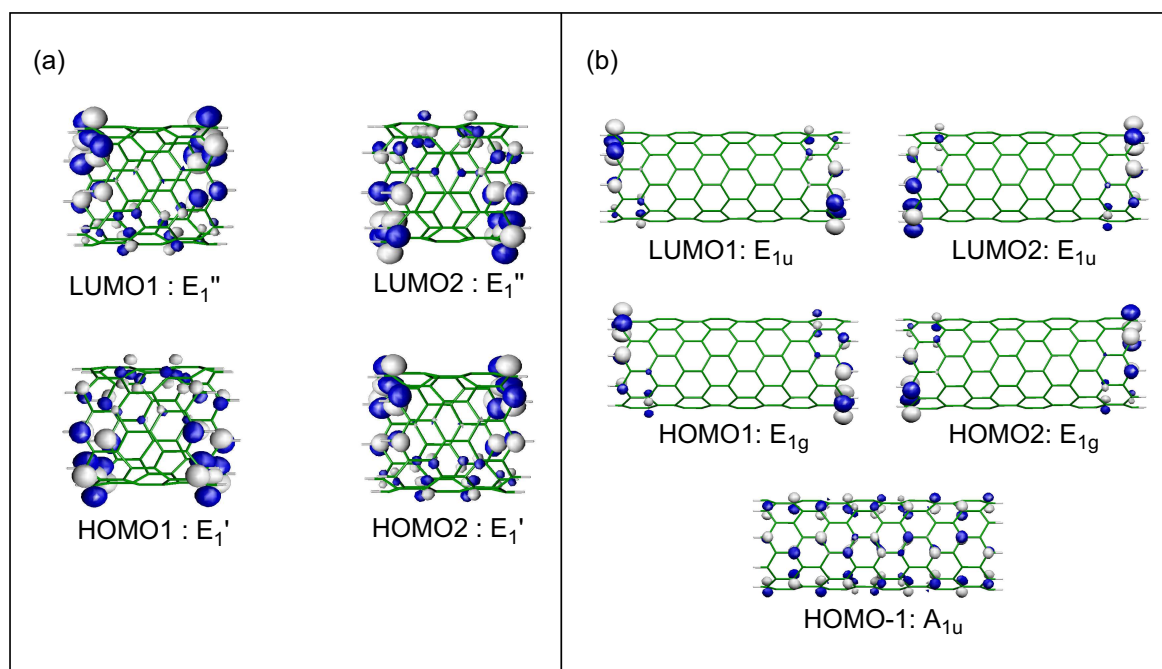


Figure 6.3: The doubly degenerate HOMO and LUMO orbitals for the (a) D_{9h} , 90 atom, and the (b) D_{9d} , 180 atom, hydrogen-capped SWNTs. Also shown is the (HOMO-1) A_{1u} orbital. The isosurfaces are ± 0.03 a.u. for the HOMOs and LUMOs and ± 0.025 a.u. for the (HOMO-1).

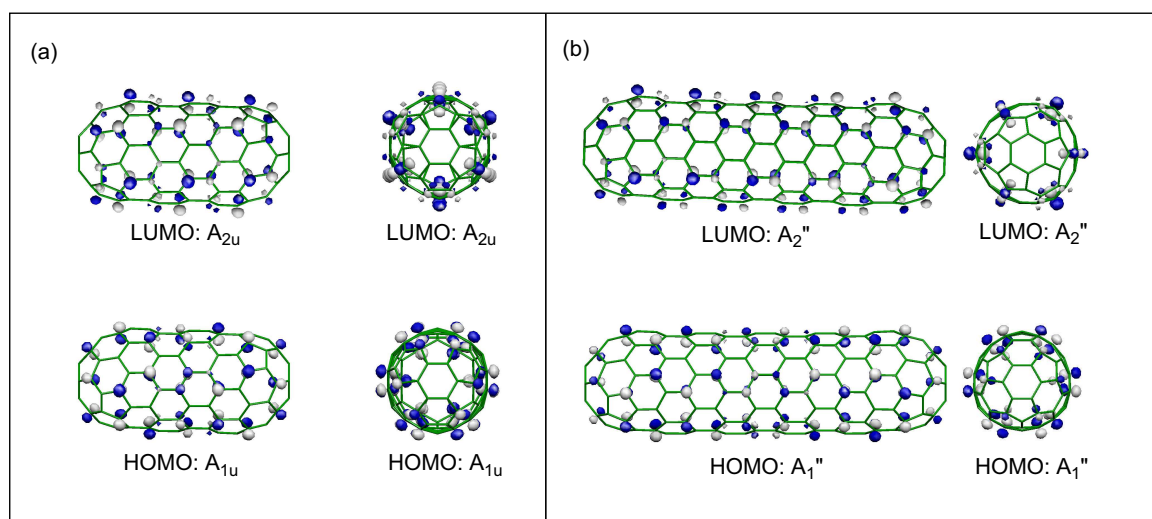


Figure 6.4: The HOMO and LUMO orbitals for the (a) D_{3d} , 132 atom, and the (b) D_{3h} , 222 atom, C_{30} -capped SWNTs. The isosurfaces are ± 0.03 a.u. and ± 0.025 a.u., respectively.

6.3.2 The NMR Chemical Shifts of (9,0) SWNTs

Our calculated value of the ^{13}C NMR chemical shift of C_{60} is 145.84 ppm. It compares well with the experimental value of 142.68 ppm.¹²⁷ In order to assess the dependence of our results on basis set and approximate density functional we have carried out additional calculations for C_{60} and some of the smaller nanotube fragments. The data for C_{60} are collected in Tab. 6.1. As can be seen certain combinations of functionals and basis sets, such as VWN/DZP, offer fortuitous error compensation. For instance, using the more flexible TZP with the VWN functional instead results in a sizeable change of the chemical shift of about 9 ppm away from the experimental value, which is to a large extent compensated when switching to the more accurate revPBE density functional. Compared to TZP, the TZ2P basis includes an additional set of 4f functions for each carbon and is thus prohibitively expensive for the larger systems studied here. The effect of the additional polarization functions on the carbon shift is not completely negligible, but also not expected to be larger than additional correlation effects as well as self-interaction corrections that are not covered by the revPBE functional. The basis set and DFT trends obtained for C_{60} are also found for the nanotube fragments that could be studied with the TZP basis, see tables 6.2, 6.3, 6.4, and 6.5. Also, the trends obtained when using smaller basis sets than TZP are similar for C_{60} , the H-capped, and the C_{30} -capped tubes. Previous experience with NMR calculations shows that other non-hybrid gradient-corrected standard functionals do not offer significantly better results in a systematic fashion. In summary, the revPBE/TZP level offers a reasonably accurate description of the systems covering the main effects from structure and electron correlation, with currently neglected correlation, self-interaction, basis set, vibrational and temperature, and intermolecular interaction effects adding up to acceptable

Table 6.1: Dependence of the ^{13}C nuclear shielding and chemical shift in C_{60} on basis set and density functional.^a

Basis	E_{XC}^b	$\sigma_{\text{C}_{60}}^c$	σ_{TMS}^d	Shift	Basis	E_{XC}^b	$\sigma_{\text{C}_{60}}^c$	σ_{TMS}^d	Shift
DZ	revPBE	57.654	203.96	146.31	DZ	VWN	51.706	202.32	150.61
DZP	revPBE	53.506	192.07	138.56	DZP	VWN	46.950	190.57	143.62
TZP	revPBE	39.265	185.10	145.84	TZP	VWN	29.835	182.71	152.88
TZ2P	revPBE	38.723	185.63	146.91	TZ2P	VWN	29.144	183.28	154.14

^a experimental chemical shift: 142.68 ppm

^b functional

^c calculated shielding constant for C_{60}

^d calculated shielding constant for TMS

deviations between theory and experiment estimated to be about 5 ppm.

Table 6.2: Dependence of the calculated ^{13}C chemical shift in the 90 atom H-capped (9,0) SWNT fragment on the basis set (revPBE functional).

Nucleus ^a	Basis	Shift ^b	Nucleus ^a	Basis	Shift ^b
1	DZ	128.51	3	DZ	136.37
	DZP	121.20		DZP	129.11
	TZP	128.69		TZP	136.87
	TZ2P	130.22		TZ2P	138.16
2	DZ	143.69	4	DZ	136.20
	DZP	137.64		DZP	129.60
	TZP	147.14		TZP	137.99
	TZ2P	148.35		TZ2P	139.28

^a The numbers refer to the numbering scheme chosen in Fig. 6.5

^b With respect to TMS. The calculated ^{13}C shielding constants for TMS are listed in Tab. 6.1

Table 6.3: Dependence of the calculated ^{13}C chemical shift in the 108 atom H-capped (9,0) SWNT fragment on the basis set (revPBE functional).

Nucleus ^a	Basis	Shift ^b	Nucleus ^a	Basis	Shift ^b	Nucleus ^a	Basis	Shift ^b
1	DZ	127.40	3	DZ	133.90	5	DZ	141.32
	DZP	119.84		DZP	127.62		DZP	135.29
	TZP	127.12		TZP	135.50		TZP	144.34
	TZ2P	128.66		TZ2P	136.83		TZ2P	145.61
2	DZ	134.01	4	DZ	133.37			
	DZP	128.00		DZP	126.35			
	TZP	136.38		TZP	133.87			
	TZ2P	137.61		TZ2P	135.10			

^a The numbers refer to the numbering scheme chosen in Fig. 6.5

^b With respect to TMS. The calculated ^{13}C shielding constants for TMS are listed in Tab. 6.1

Table 6.4: Dependence of the calculated ^{13}C chemical shift in the 132 atom C_{30} -capped (9,0) SWNT fragment on the basis set (revPBE functional).

Nucleus ^a	Basis	Shift ^b	Nucleus ^a	Basis	Shift ^b	Nucleus ^a	Basis	Shift ^b
1	DZ	152.18	6	DZ	132.49	11	DZ	132.05
	DZP	146.16		DZP	125.63		DZP	125.15
	TZP	153.77		TZP	133.84		TZP	131.99
2	DZ	151.26	7	DZ	145.03	12	DZ	131.62
	DZP	144.66		DZP	137.40		DZP	124.98
	TZP	152.67		TZP	145.22		TZP	132.48
3	DZ	134.87	8	DZ	147.94	13	DZ	139.71
	DZP	128.40		DZP	140.42		DZP	133.51
	TZP	135.62		TZP	148.20		TZP	140.68
4	DZ	133.85	9	DZ	141.06	14	DZ	147.09
	DZP	126.75		DZP	134.94		DZP	140.05
	TZP	134.57		TZP	142.52		TZP	147.79
5	DZ	129.14	10	DZ	133.05			
	DZP	122.62		DZP	126.46			
	TZP	130.19		TZP	134.31			

^a The numbers refer to the numbering scheme chosen in Fig. 6.6

^b With respect to TMS. The calculated ^{13}C shielding constants for TMS are listed in Tab. 6.1

Table 6.5: Dependence of the calculated ^{13}C chemical shift in the 150 atom C_{30} -capped (9,0) SWNT fragment on the basis set (revPBE functional).

Nucleus ^a	Basis	Shift ^b	Nucleus ^a	Basis	Shift ^b	Nucleus ^a	Basis	Shift ^b
1	DZ	152.64	7	DZ	139.72	13	DZ	129.59
	DZP	146.85		DZP	133.27		DZP	123.16
	TZP	154.65		TZP	140.54		TZP	130.76
2	DZ	151.45	8	DZ	131.89	14	DZ	140.74
	DZP	144.86		DZP	125.40		DZP	134.56
	TZP	152.93		TZP	133.10		TZP	141.92
3	DZ	135.35	9	DZ	133.15	15	DZ	134.38
	DZP	128.86		DZP	126.47		DZP	127.96
	TZP	135.96		TZP	134.12		TZP	135.39
4	DZ	134.18	10	DZ	148.57	16	DZ	129.32
	DZP	127.04		DZP	141.23		DZP	122.61
	TZP	134.76		TZP	149.02		TZP	129.87
5	DZ	129.15	11	DZ	145.29			
	DZP	122.43		DZP	137.88			
	TZP	130.02		TZP	145.65			
6	DZ	146.63	12	DZ	132.31			
	DZP	139.59		DZP	125.50			
	TZP	147.28		TZP	133.21			

^a The numbers refer to the numbering scheme chosen in Fig. 6.6

^b With respect to TMS. The calculated ^{13}C shielding constants for TMS are listed in Tab. 6.1

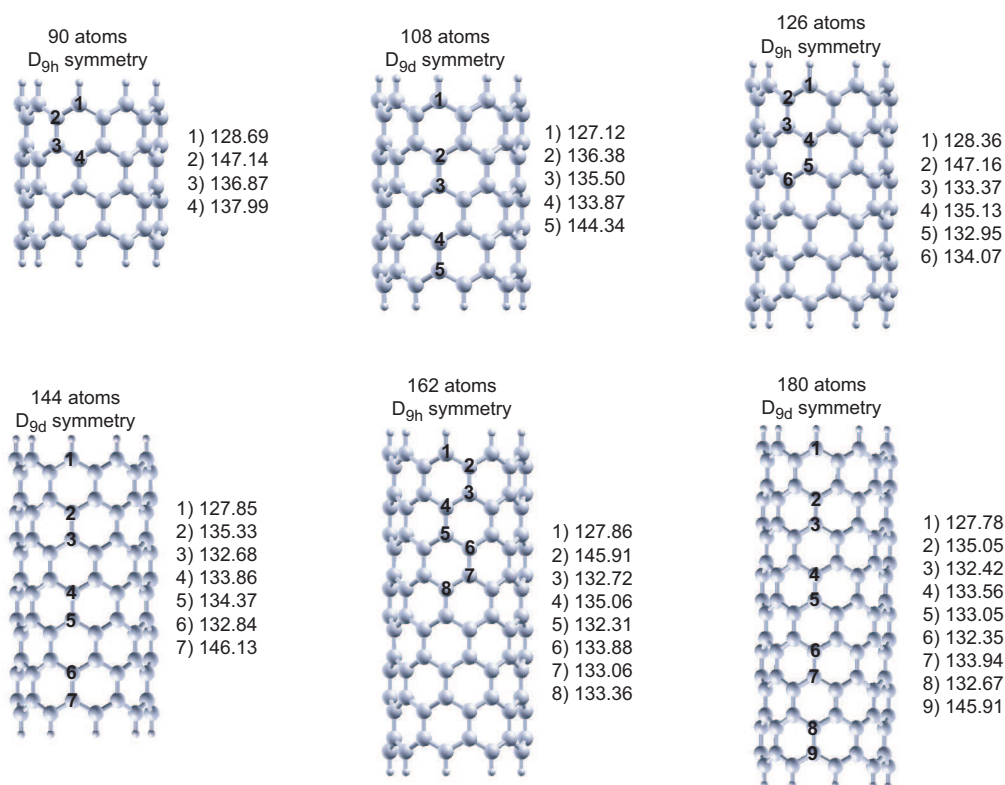


Figure 6.5: The ^{13}C NMR chemical shifts of hydrogen-capped D_{9h}/D_{9d} (9,0) SWNTs, with respect to TMS. revPBE functional, TZP basis.

All computed chemical shifts for the nanotube fragments are listed in Figs. 6.5 and 6.6 besides graphics of the SWNT fragments to allow for an easy comparison of the chemical shifts with the position of the respective carbon atom in the tube.

We note a number of trends: For the H-capped fragments, the chemical shifts at the ends are smaller than in the tube's center if the carbon is directly bound to a hydrogen, otherwise it is larger. The values in the middle of the tube seem to approach a value of about 133 ppm from above for increasing length of the tubes. For the C_{30} -capped fragments, the shifts of the carbons in the middle of a fragment are always smaller than at the end. The carbon shifts in the tips of the caps exceed the one for C_{60} by about 14 ppm for the longest members. The carbon shifts in the middle of the fragments approach a value between 129 and 130 ppm, also from above. This chemical shift is in surprisingly good agreement with the experimental values of 126, 124 and 128 ppm quoted previously. It should be remembered that the experimental sample was certainly not consisting of only one type of tube. Nevertheless, the agreement is encouraging, in particular when considering — by comparison with our C_{60} results — that the computed values are likely to overestimate experimental results by about 3 ppm.

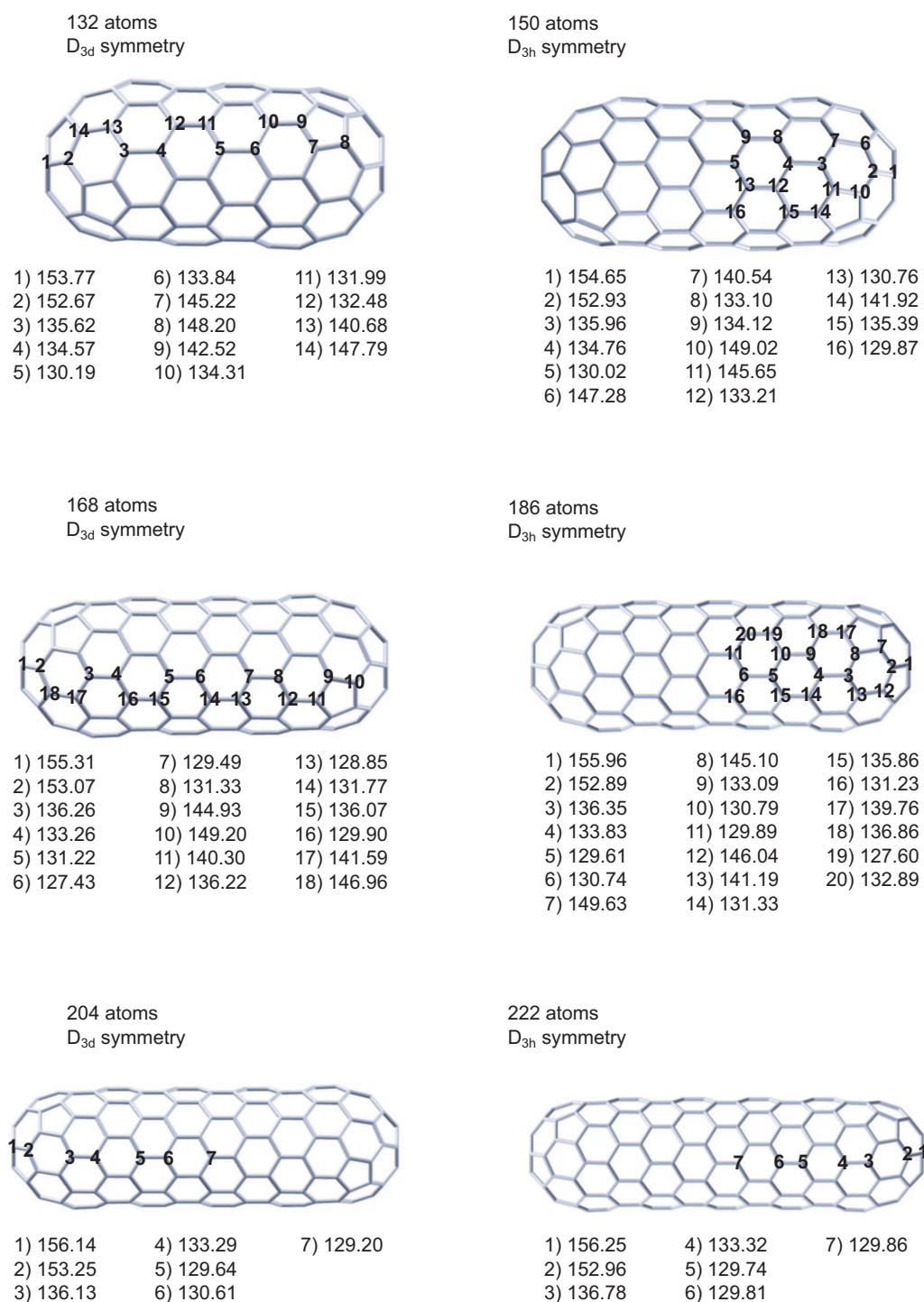


Figure 6.6: The ^{13}C NMR chemical shifts of C_{30} -capped D_{3h}/D_{3d} (9,0) SWNTs, with respect to TMS. revPBE functional, TZP basis.

The discrepancy between the central chemical shifts for the H-capped and the C₃₀-capped systems must be attributed to the different nature of the frontier orbitals. It cannot be expected that an orbital which is mainly localized at the tube's ends has a considerable direct contribution to the chemical shift of a carbon residing in the middle of a tube. However, from the preceding discussion it is obvious that there is a large effect of the HOMO on the energies of the HOMO-1 etc. which will have an influence on the ¹³C chemical shifts (the expression for the paramagnetic shielding tensor contains $(\Delta E_{vo})^{-1}$, the inverse of the energy differences between virtual (*v*) and occupied (*o*) orbitals). As long as there is a noticeable interaction between the HOMO and the HOMO-1, say, with the latter yielding an important contribution to the shielding of one of the central carbons, the chemical shift is not converged. From our analysis of the frontier orbitals in the H-capped and the C₃₀-capped fragments we believe that the chemical shifts of the latter are closer to the converged values for an infinite semiconducting (9,0) SWNT than the former. For longer fragments, improved agreement with experimental estimates should be expected, in particular for the H-capped systems. This is due to the fact that in both cases the central carbon atoms should afford the same chemical shifts as the fragments approach infinite length, unless capping effects prove to have a substantial influence on the properties of the tubes. In order to verify this conjecture, further computational studies on longer tube fragments are necessary.

In order to determine if the chemical shifts are dependent upon the symmetry of the C₃₀-capped SWNTs, a computation on the smallest tube possessing *D*₃ symmetry was made. Comparison of the results, shown in Figure 6.7, with the 132 atom tube of *D*_{3d} symmetry reveals that the shifts at the end of the tube are 3.45 and 6.11 ppm larger for the former than for the latter. Moreover for the *D*₃ tube, shifts in the middle range from \approx 124-136 ppm, whereas for the *D*_{3d} tube the shifts near the middle are 131.99 and 130.19 ppm. Under the assumption that the shifts are converged for the 132 atom *D*₃ member, we can conclude that the *D*₃ set

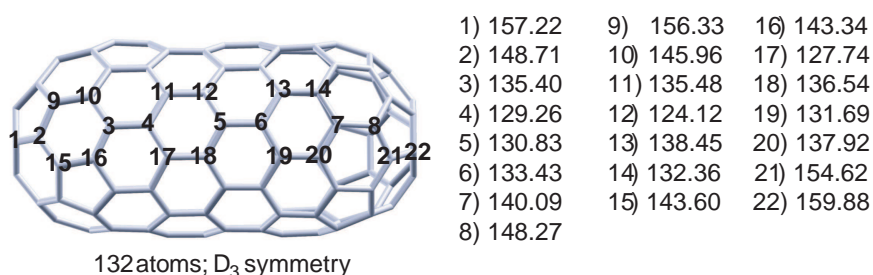


Figure 6.7: The ¹³C NMR chemical shifts of a 132 atom, C₃₀-capped *D*₃ (9,0) SWNT, with respect to TMS. revPBE functional, TZP basis.

will have a larger chemical shift range than the D_{3h}/D_{3d} series, however the average of this range will not be significantly different than the shift predicted for the energetically more stable species. However, once again calculations on longer fragments must be made in order to verify the influence of the caps on the electronic structure and properties of the tubes. The 132 atom D_3 tube is predicted to be 4.85 kcal/mol less stable than the D_{3d} tube in our calculations. This is in agreement with other DFT calculations.⁸⁸

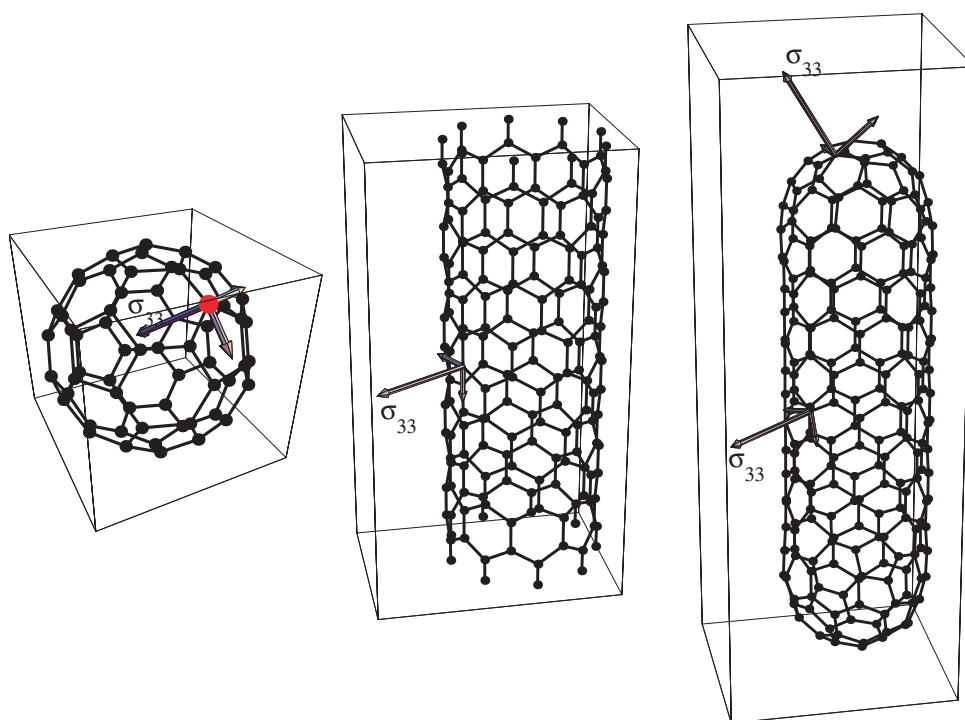


Figure 6.8: Orientation of the calculated shielding tensors for C_{60} and the largest H- and C_{30} -capped nanotube fragments. The arrows indicate the principal axes. The arrows' lengths reflect the magnitude of the principal shielding components. For reasons of clarity of presentation they are not exactly proportional. The large diamagnetic σ_{33} component is indicated. See Tables 6.6 and 6.7 for numerical data (180-atom H-capped tube: atom no. 5; 222-atom C_{30} -capped tube: atoms no. 1 and 7). See Figs. 6.5 and 6.6 for numbering.

For completeness, we also report the calculated principal components of the shielding tensors. From the data collected in Tables 6.6 and 6.7 it can be seen that the shielding tensor components converge in a similar way as the chemical shifts when increasing the tube length, albeit not as smoothly as the isotropic shieldings. The shielding tensors are strongly anisotropic. For C_{60} , the shielding tensor affords a large positive component perpendicular to the “bucky-ball’s” surface, and two negative components within the surface that are an order of magnitude smaller (Fig. 6.8). The shielding tensors for the H-capped and C_{30} -capped SWNTs are very

Table 6.6: Principal components of the shielding tensors σ for the H-capped (9,0) SWNT fragments and C_{60} , calculated at the TZP/revPBE level.

System	no ^a	σ_{11}	σ_{22}	σ_{33}	System	no ^a	σ_{11}	σ_{22}	σ_{33}
$C_{72}H_{18}$	1	-24.405	50.914	142.713	$C_{144}H_{18}$	1	-13.690	46.971	144.448
	2	-40.630	-13.914	168.437		2	-31.942	-15.694	163.420
	3	-27.934	-2.098	174.733		3	-14.133	-3.864	174.103
	4	-30.549	-6.258	178.126		4	-15.511	-9.376	172.281
$C_{90}H_{18}$	1	-18.707	49.133	143.517	5	-11.593	-7.296	175.816	
	2	-20.692	-6.646	173.485	6	-13.771	-9.037	170.827	
	3	-20.229	-6.692	175.736	7	-9.290	-7.679	172.799	
	4	-18.645	-0.252	172.589	8	-8.945	-7.971	171.168	
	5	-32.893	-13.607	168.796	$C_{162}H_{18}$	1	-17.362	46.889	142.440
$C_{108}H_{18}$	1	-20.894	47.942	143.183		2	-12.926	-7.625	170.714
	2	-34.514	-14.917	163.249		3	-8.869	-6.359	173.275
	3	-14.445	-2.182	171.804		4	-8.973	-7.237	170.824
	4	-15.442	-7.009	172.367		5	-9.193	-5.344	170.698
	5	-13.117	-6.253	175.824	6	-7.621	-5.613	171.483	
	6	-13.694	-7.533	174.305	7	-10.231	-8.320	172.018	
$C_{126}H_{18}$	1	-18.815	47.253	143.320	8	-12.137	-2.022	171.460	
	2	-14.525	-7.711	171.556	9	-30.190	-14.732	162.479	
	3	-10.663	-6.005	173.922	C_{60}		-26.037	-21.053	164.885
	4	-10.649	-7.638	172.019					
	5	-12.225	-8.094	172.502					
	6	-13.418	-1.923	172.117					
	7	-32.624	-14.784	164.328					

^aThe atom numbers refer to the numbering scheme chosen in Fig. 6.5

Table 6.7: Principal components of the shielding tensors σ for the C_{30} -capped (9,0) SWNT fragments, calculated at the TZP/revPBE level.

System	no ^a	σ_{11}	σ_{22}	σ_{33}	System	no ^a	σ_{11}	σ_{22}	σ_{33}
C_{132}	1	-54.855	-20.547	169.399	C_{186}	12	-19.462	-7.134	173.223
	2	-73.399	-0.788	171.485		13	-13.832	9.002	173.568
	3	-13.618	-9.476	171.543		14	-19.553	2.325	177.229
	4	-17.825	-5.531	174.944		15	-19.036	-11.280	177.393
	5	-16.680	1.469	179.943		16	-18.627	3.486	180.745
	6	-13.085	-3.738	170.601		17	-40.240	-15.727	186.494
	7	-48.568	-3.745	171.960		18	-64.258	-29.661	208.347
	8	-48.570	-18.930	178.213		1	-73.066	-17.124	177.621
	9	-51.820	19.884	159.685		2	-96.614	-7.141	200.386
	10	-17.923	-3.517	173.797		3	-25.874	-6.052	178.183
	11	-10.121	-4.780	174.218		4	-20.331	-8.597	182.744
	12	-21.016	-0.573	179.455		5	-6.833	-4.280	177.579
	13	-28.048	-15.425	176.717		6	-9.418	-4.732	177.226
	14	-42.689	-28.806	183.416		7	-71.798	-29.117	207.319
C_{150}	1	-63.216	-18.600	173.169	8	-65.714	-11.482	197.203	
	2	-72.678	-16.578	185.763	9	-17.876	-1.005	174.905	
	3	-18.683	-16.252	182.339	10	-19.904	0.733	182.108	
	4	-19.226	-3.985	174.222	11	-12.951	-0.791	179.374	
	5	-8.204	-6.767	180.216	12	-75.458	-28.498	221.134	
	6	-53.602	-28.239	195.313	13	-46.757	-14.467	192.941	
	7	-33.637	-14.688	182.012	14	-20.697	0.037	181.970	
	8	-21.776	-2.541	180.317	15	-17.668	-12.479	177.875	
	9	-13.536	-12.552	179.037	16	-16.954	-0.016	178.575	
	10	-55.645	-31.505	195.389	17	-54.980	17.439	173.554	
	11	-52.994	-11.019	182.348	18	-18.688	-8.950	172.359	
	12	-16.291	-0.831	172.776	19	-14.420	14.389	172.525	
	13	-18.489	0.746	180.770	20	-18.306	-1.153	176.089	
	14	-54.870	21.436	162.962	C_{204}	1	-75.801	-19.414	182.100
	15	-17.792	-4.290	171.203		2	-105.626	-10.218	211.382
	16	-15.776	8.056	173.419		3	-30.247	-8.991	186.153
C_{168}	1	-65.426	-20.424	175.059		4	-19.657	-7.014	182.098
	2	-88.549	-6.774	191.149		5	-7.091	-5.820	179.295
	3	-21.624	-9.277	177.436		6	-9.927	-3.326	176.71
	4	-16.061	-5.150	176.648		7	-10.009	0.781	176.925
	5	-11.231	-5.494	178.138	C_{222}	1	-82.120	-16.480	185.153
	6	-6.959	3.786	176.016		2	-114.918	-10.313	221.639
	7	-15.480	3.244	179.219		3	-36.064	-6.003	187.021
	8	-9.917	1.730	169.453		4	-22.210	-10.705	188.240
	9	-59.091	-7.026	186.617		5	-7.639	-4.958	178.661
	10	-65.415	-21.775	194.876		6	-9.607	-2.196	177.682
	11	-53.849	20.352	167.893		7	-9.012	-2.062	176.789

^aThe atom numbers refer to the numbering scheme chosen in Fig. 6.6

similar in the tube's center. These, as well as the shielding tensors at the tip of the caps in the C_{30} -capped systems are qualitatively comparable to C_{60} in the sense that the large diamagnetic component is perpendicular to the carbon framework. Generally, in the middle of the tube fragments, the negative components within the surface are significantly smaller in magnitude than for C_{60} . The smaller chemical shift for the (9,0) SWNT compared to C_{60} is seen to result both from an increase of the magnitude of the positive σ_{33} component and a decrease of the magnitude of the negative σ_{11} and σ_{22} components.

6.4 Summary and Conclusions

In this chapter we have presented the results of density functional calculations on the NMR chemical shifts of single-walled carbon nanotube (SWNT) fragments. The study was carried out for the nonhelical (9,0) system. In agreement with recent computational and experimental studies, the (9,0) SWNT is predicted to have a finite band gap. The analysis of the energies and the nature of the frontier orbitals indicates that hydrogen-capped tube fragments are not necessarily good models for the infinite systems, at least not at sizes which are currently accessible to first-principles molecular calculations. The HOMO and LUMO themselves need to be considered as artifacts when making attempts to compare with the infinite systems. In contrast, the C_{30} -capped SWNT fragments appear to represent good models for the infinite systems. Their properties converge reasonably fast with increasing length of the fragments. The chemical shift for the (9,0) SWNT is estimated from our calculations to be around 130 ppm which is in encouraging agreement with experimental estimates. Comparison between a tube of D_{3d} and one of D_3 symmetry indicates that tubes in the latter set may have a broader chemical shift range, whose average lies near the value predicted for the D_{3d}/D_{3h} series. When taking the theoretical predictions by Latil *et al.*⁹⁵ for the difference between semiconducting and metallic SWNTs into consideration (metallic systems were found to be 11 ppm less shielded), and assuming that the result for the (9,0) tube is typical for a semiconducting system, metallic tubes' chemical shifts can be expected to be close to that of C_{60} . Future work needs to address the influence of the caps, diameter and helicity on the properties of SWNTs.

Chapter 7

Magic $(C_{60})_n$ -Metal Compound Clusters

7.1 Introduction

Experimental work on fullerenes coated with alkali-metal atoms,¹²⁸ alkaline-earth metal atoms¹²⁹ and transition-metal atoms,¹³⁰ has revealed that each metal- C_{60} cluster displays very different behaviour and properties. The thermal stability of such clusters can be measured by Time of Flight (TOF) mass spectrometry. Particularly stable structures may be identified by a set of pronounced, commonly dubbed as *magic* peaks, in the mass spectra. The enhanced stability of $Ba_{32}C_{60}$ was attributed to so-called geometrical shell filling.¹²⁹ It was postulated that each Ba atom lies on top of one of the 12 pentagonal or 20 hexagonal faces of the fullerene and completion of this first metallic layer leads to increased stability. On the other hand, similar experiments showed that $(K_6C_{60})_nK^+$ is magic due to electronic shell filling.¹²⁸ The C_{60} LUMO is triply degenerate and can therefore accommodate six electrons. Thus, a transfer of the valence $[4s^1]$ electrons from 6 K atoms would yield a particularly stable structure. Recent work using a novel experimental set-up has revealed a different set of magic peaks for potassium and barium fullerene clusters,¹³¹ which cannot be explained by either one of the aforementioned arguments.

In the experiments of Martin *et al.*,^{128,129} the clusters were produced in a low-pressure, inert gas condensation cell cooled by liquid nitrogen. After being transported to a high vacuum chamber they were photoionized. In order to enhance the intensity of the magic peaks it was necessary to heat the clusters either with the same laser pulse used for ionization, or by a second pulse which arrived after the ionizing laser. The new experimental set-up contained a novel heating/cooling stage mounted directly after the cluster source.¹³¹⁻¹³³ Here, the clusters attained a temperature varying between 150 K to 1800 K via thermalization with a He bath for a time span on the order of ≤ 1 ms. Afterwards, they were cooled to 150 K

then photoionized and measured by TOF mass spectrometry. The heating method had a significant effect on the experimental results. For $Ba_n(C_{60})_m$, the magic peaks corresponded to $(m, n) = (2, 3), (3, 5), (4, 7), (5, 10), (6, 13)$ and $(7, 14)$, whereas for $K_n(C_{60})_m$ they were found to be $(m, n) = (2, 4), (3, 6), (4, 8), (5, 11), (6, 14)$ and $(7, 17)$, neither of which is in agreement with geometrical nor with electronic shell filling.¹³¹ The TOF mass spectra of the two systems can be found in Fig. 7.1. Since photon absorption occurs within nanoseconds, it was postulated that the clusters produced previously may not be the most energetically stable configurations. The new experimental set-up overcomes this: the longer annealing times allow the clusters to explore the potential energy surface, thereby increasing the probability to reach the global energy minima.

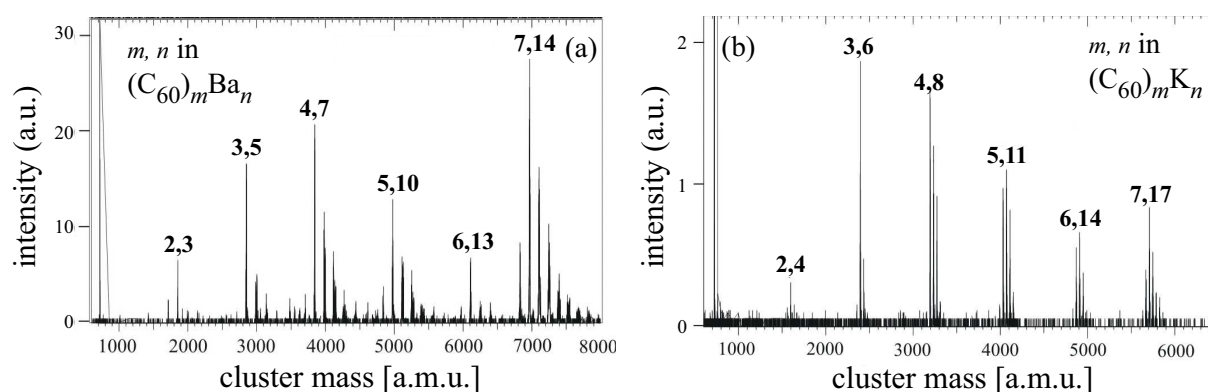


Figure 7.1: TOF mass spectra of (a) $Ba_n(C_{60})_m$ compound clusters after annealing to 1780 K, and (b) $K_n(C_{60})_m$ compound clusters after annealing to 900 K.¹³¹

Despite the fact that theoretical work on exohedral fullerene clusters is abundant, only a few papers specifically consider a single C_{60} with a varying amount of K atoms. Electronic structure calculations have been performed on K_nC_{60} with $n = 1, 2, 3$;^{134,135} $n = 6, 12$ ¹³⁵ and $n = 32$.¹³⁶ To the best of our knowledge, there has not been any previous computational work on Ba containing clusters, however DFT has been used to study Ca_nC_{60} , with $n = 12, 20$ ¹³⁷ and $n = 32$.^{136,137}

The goal of this study was to determine the nature of the stability of the newly observed magic clusters. First, we present some preliminary calculations on M_nC_{60} ($M = K, Ba$) clusters in order to gauge if the computational methodology used gives results consistent with previous literature. Moreover, this preliminary study reveals the preferred bonding mode of potassium and barium to a single C_{60} and suggests how the metals may complex with more than one fullerene. Due to the formidable computational cost the *ab initio* calculations were limited to clusters containing two C_{60} s. First, the energetically most stable species are determined and the bonding for both metals is analyzed. Secondly, the finite temperature contributions to the Gibbs

free energies are obtained and their effect on the cluster stability is determined. The entropic contributions are shown to be important in determining the cluster stability. Due to the computational expense, they are usually not considered despite the fact that at finite temperatures the most stable clusters minimize the free energy.¹³⁸ Finally, singly and doubly charged species are considered briefly.

7.2 Computational Details

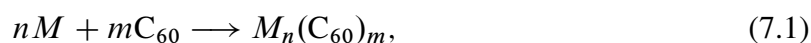
The computations were performed with the Amsterdam Density Functional (ADF)^{101,102} and the Turbomole¹³⁹ program packages. In the ADF calculations we have applied the revised Perdew–Burke–Ernzerhof (revPBE) non-hybrid gradient density functional^{65,103–105} along with the Vosko–Wilk–Nusair¹⁴⁰ (VWN) local density approximation (LDA). Full geometry optimizations were carried out employing a valence triple- ζ Slater-type basis set with polarization functions for all atoms (TZP) from the ADF basis set library. The core shells up to 1s, 4p, and 2p of carbon, barium and potassium, respectively, were kept frozen. Despite the fact that carbon and potassium are not heavy nuclei, all geometry optimizations with ADF were performed using the zeroth-order regular approximation (ZORA) Hamiltonian^{141–143} in order to facilitate comparison with the “relativistic” barium containing clusters. The ADF code was used to obtain geometries and bonding energies of high quality, and to perform the bonding energy analysis in terms of fragment orbitals. Additional finite temperature enthalpic and entropic contributions to the Gibbs free energy were calculated with the Turbomole code at a somewhat lower accuracy. The Turbomole calculations employed the PBE^{65,144–146} functional since the revPBE functional was not available. We have used the “resolution-of-identity” (RI)^{147,148} technique along with the polarized split-valence SV(P) basis set augmented with the default auxiliary (RI) basis sets from the Turbomole basis set library in order to reduce the computational effort. Relativistic effects were considered in these calculations via a scalar relativistic (6s6p5d) / [4s3p3d] ECP basis with 46 core electrons.^{139,149} A subset of the graphics were prepared using the XCRYSDEN program.¹¹⁷

For the systems containing an even number of electrons, when a given symmetry constraint arose in a half-filled HOMO, a symmetry breaking distortion was applied to the cluster, resulting in a geometry with a closed-shell electronic configuration, unless otherwise stated. When an odd number of electrons were present, the structures presented here afford a single unpaired valence electron (doublet) and unrestricted DFT calculations were performed.

It was computationally too expensive to carry out numerical-derivative frequency calculations with ADF. Therefore, the ADF geometries were reoptimized with Turbomole, using the less flexible SV(P) basis set and the RI technique in order to keep the computational effort manageable. The same computational settings were used to perform analytical calculations of

the vibrational frequencies^{150,151} and finite temperature contributions to the Gibbs free energy based thereupon. At times, it was necessary to lower the symmetry and re-optimize the cluster geometry in order to obtain minima. However, the energy changes were much smaller than the bonding energy differences obtained from ADF and Turbomole and are most likely explained by the different basis sets applied and the use of the RI technique. These cluster geometries were not reoptimized with ADF due to the immense computational cost involved. The *BEM* and *GFM* presented in the main text were obtained by using the ADF energies (which must be considered more accurate than those obtained with Turbomole because of the higher quality basis set applied), augmented with the finite temperature corrections obtained from the Turbomole frequencies calculations. Thermochemical properties were calculated, using standard expressions, at the experimental temperature (150 K) and pressure (10⁻⁶ Torr).

Within this chapter we will consider the general reaction



where $M = \text{K, Ba}$ and $m = 1, 2$. It will prove useful to compare thermochemical quantities divided by the number of metal atoms, n , in the above reaction. Thus, if $E(x)$ is the energy of species x , we will define the bonding energy per metal atom, *BEM*, as

$$BEM = \frac{E(M_n(C_{60})_m) - n \times E(M) - m \times E(C_{60})}{n}. \quad (7.2)$$

The change in the: Gibbs free energy per metal atom, *GFM*, finite temperature enthalpy correction per metal atom, *H_{EC}M*, and the entropy per metal atom multiplied by the temperature, *TSM*, will be defined similarly to the *BEM* in Eq. 7.2 for the reaction given in 7.1.

To understand why it is the *BEM* and *GFM* which determine the stability of a cluster consider, for example, a mixture of 6 fullerene molecules and 3 Ba atoms. This could lead to the formation of: (i) three Ba(C₆₀)₂ clusters; (ii) one Ba₃(C₆₀)₂ cluster and four C₆₀ molecules; (iii) one Ba₂(C₆₀)₂ and one Ba(C₆₀)₂ cluster along with two C₆₀ molecules. The *total* Gibbs free energy change for the formation of these clusters from C₆₀ molecules and Ba atoms would then be (using the computed values from Sec. 7.3.2): (i) 3 × -53.24 kcal/mol = -159.72 kcal/mol; (ii) 3 × -60.90 kcal/mol = -182.70 kcal/mol; (iii) 2 × -55.73 kcal/mol - 53.26 kcal/mol = -164.72 kcal/mol. Thus, (ii) results in the most negative Gibbs free energy for the system showing that the preferred reaction yields Ba₃(C₆₀)₂. The difference between the Gibbs free energy changes for two reactions per metal atom is then equal to the difference between the average *GFM* for a given system. For example, the average *GFM* for (ii) and (iii) are -60.90 kcal/mol and (2 × -55.73 - 53.24)/3 = -54.90 kcal/mol, respectively. Subtracting (ii) from (iii) gives 6 kcal/mol. The difference between the respective total Gibbs free energy changes per metal atom is (-164.72 + 182.7)/3 = 6 kcal/mol. The same holds true for the bonding energies. It can thus be seen that the *BEM* and *GFM* reflect the stabilities of the clusters.

In order to clarify the nature of the bonding, we performed a fragment orbital analysis, using the distorted fullerenes (as found in the optimized clusters) and the free metal atoms, as fragments.¹⁰² This yielded the composition of the molecular orbitals of the metal-fullerene cluster in terms of the occupied and unoccupied orbitals of Ba/K and C₆₀.

7.3 Results and Discussion

7.3.1 Ba_nC₆₀ and K_nC₆₀ Clusters

The geometries of five possible isomers of MC₆₀ ($M = \text{K, Ba}$) were optimized. The metal atom may lay on top of: a hexagonal face (MC_{60}^{hex}), a pentagonal face (MC_{60}^{pent}), a carbon atom (MC_{60}^{atom}), a bond belonging to two hexagonal faces (MC_{60}^{b1}) or a bond belonging to one hexagonal and one pentagonal face (MC_{60}^{b2}), of the fullerene. Table 7.1 gives the *BEM* and Mulliken charges for these different structures. For both potassium and barium, the MC_{60}^{hex} isomer had the lowest *BEM*, in accordance with previous theoretical calculations for KC₆₀.^{134,135} MC_{60}^{b2} ($M = \text{K, Ba}$) and BaC₆₀^{atom} are not minima on the potential energy surface, and optimized to yield MC_{60}^{pent} and BaC₆₀^{b1}, respectively. Examination of the charges revealed an almost full transfer of the [4s¹] valence electron from potassium to the fullerene LUMO. A full charge donation between the barium atom and C₆₀ does not occur, as can be seen in the Mulliken charges of ~ 1.3 .

Hamamoto *et al.*, have found that for the most stable isomers of K_nC₆₀ ($n = 1, 2, 6$) and K₃C₆₀⁻, the potassium atoms are located on top of the hexagonal fullerene faces. Moreover, in order to reduce the Coulombic repulsion, the positively charged potassiums are as far apart from each other as possible.¹³⁵ With this in mind, we have optimized possible structures for K_nC₆₀ ($1 \leq n \leq 6$), shown in Fig. 7.2. Since it was not the main goal of this work to study clusters

Table 7.1: The *BEM* and Mulliken charges for different isomers of MC₆₀ ($M = \text{K, Ba}$). All energies given in kcal/mol.

Isomer	Symmetry	$M = \text{K}$		$M = \text{Ba}$	
		<i>BEM</i>	Charge	<i>BEM</i>	Charge
MC_{60}^{hex}	(C _s)	-38.87	0.92	-43.75	1.31
MC_{60}^{pent}	(C _s)	-36.98	0.93	-38.14	1.31
MC_{60}^{atom}	(C _s)	-34.44	0.93	-	-
MC_{60}^{b1}	(C _{2v})	-33.47	0.93	-40.78	1.27
MC_{60}^{b2}	(C _s)	-	-	-	-

containing one fullerene, different geometrical alternatives were not considered. Nonetheless, we can examine the *BEM* and average Mulliken charges per potassium for the optimized clusters, given in Fig. 7.3(a) and 7.3(b), respectively. In agreement with previous work,^{134,135} the *BEM* becomes less negative and the charge per atom decreases, with increasing n . In order to decrease the Coulomb repulsion between potassium atoms, progressively less charge is donated to the C_{60} unoccupied orbitals as n increases. This implies a weaker ionic bonding, and moreover a decrease in the amount of energy gained upon cluster formation for larger n . However, as will be shown later, it is not the *BEM*, but the *GFM*, which determines the most stable cluster.

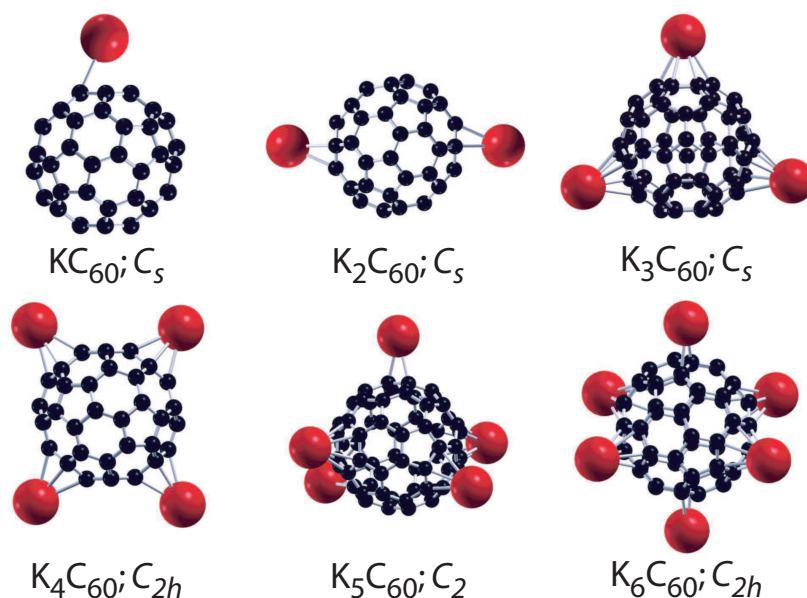


Figure 7.2: Optimized geometries and symmetries of the $K_n C_{60}$ ($1 \leq n \leq 6$) clusters.

We have also optimized possible isomers of $Ba_n C_{60}$ ($n = 2, 3$), with the same configuration as the potassium clusters shown in Fig. 7.2. The *BEM* and average Mulliken charges per barium can be found in Fig. 7.3(c) and 7.3(d), respectively. The *BEM* for the barium clusters are ~ 5 kcal/mol lower than for the potassium, indicating stronger C_{60} -Ba bonding. Once again, the average charge on the metal decreases with increasing n . However, in contrast to the potassium clusters, the structure with the lowest *BEM* contains two, not one, metal atoms.

From this initial study on potassium and barium interaction with C_{60} , the following conclusions can be made. First of all, both prefer to bond to a hexagonal fullerene face. However, the nature of the metal- C_{60} interaction is different in each case. For potassium, the bonding appears to be purely ionic with a decreasing amount of charge transfer to the C_{60} per K (and therefore a decreasing *BEM*), with increasing n . In the case of barium, the bonding cannot be completely ionic, otherwise charges of ~ 2 should be calculated. Another mechanism must be

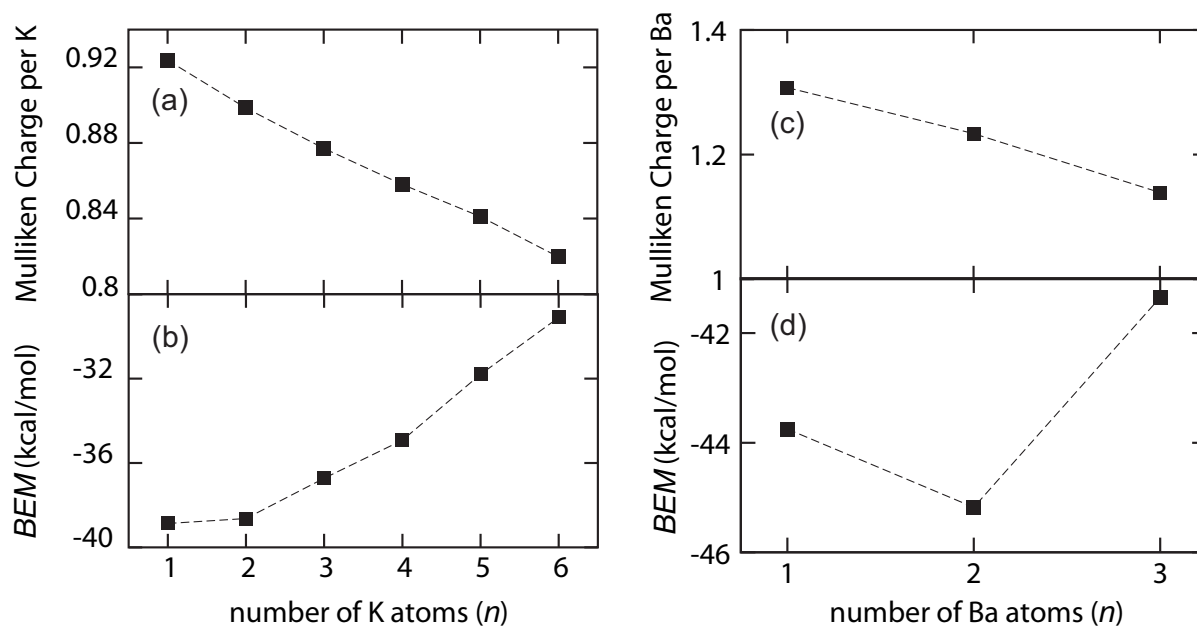


Figure 7.3: (a) *BEM* and (b) average Mulliken charges per K atom, of the K_nC_{60} ($1 \leq n \leq 6$) clusters. (c) *BEM* and (d) average Mulliken charges per Ba atom, of the Ba_nC_{60} ($1 \leq n \leq 3$) clusters.

considered which also explains the minima in the *BEM* occurring for Ba_2C_{60} .

7.3.2 Bonding and Stability of $Ba_n(C_{60})_2$ ($1 \leq n \leq 6$) Clusters

The optimized geometries and *BEM* of possible $Ba_n(C_{60})_2$ ($1 \leq n \leq 6$) isomers are given in Fig. 7.4. Due to the fact that irradiation of solid C_{60} with visible or ultra-violet light induces a [2+2] cycloaddition leading to the formation of C_{60} dimers,^{152,153} we have considered structures containing a $(C_{60})_2$ carbon framework, 7.4.1 and 7.4.4. Examination of the most stable $n = 1, 2$ clusters (7.4.2 and 7.4.5) shows that their *BEM* is much lower (40-45 kcal/mol), indicating that a C_{60} —bridging-Ba bond is much stronger than the bond between two C_{60} s. Moreover, comparison of 7.4.6 and 7.4.8 reveals that the C_{60} —bridging-Ba bond is also more favourable than a Ba-Ba bond. The most stable structures for a given n all have a C_{60} - Ba_n - C_{60} arrangement, with the barium atoms sandwiched between the two fullerenes (Set A). However, as n increases, the *BEM* of clusters with a Ba - C_{60} - $Ba_{(n-2)}$ - C_{60} - Ba configuration (Set B) becomes comparable. For example, the *BEM* of 7.4.11 is only 1.3 kcal/mol less negative than that of 7.4.12. It must be noted that for the $Ba(C_{60})_2$ cluster belonging to Set A, we considered geometries where the barium atom was situated between: two hexagonal rings (with D_{3d} , D_{3h} , C_{2v} and C_{2h} symmetries); two hexagonal rings rotated 30° with respect to each other

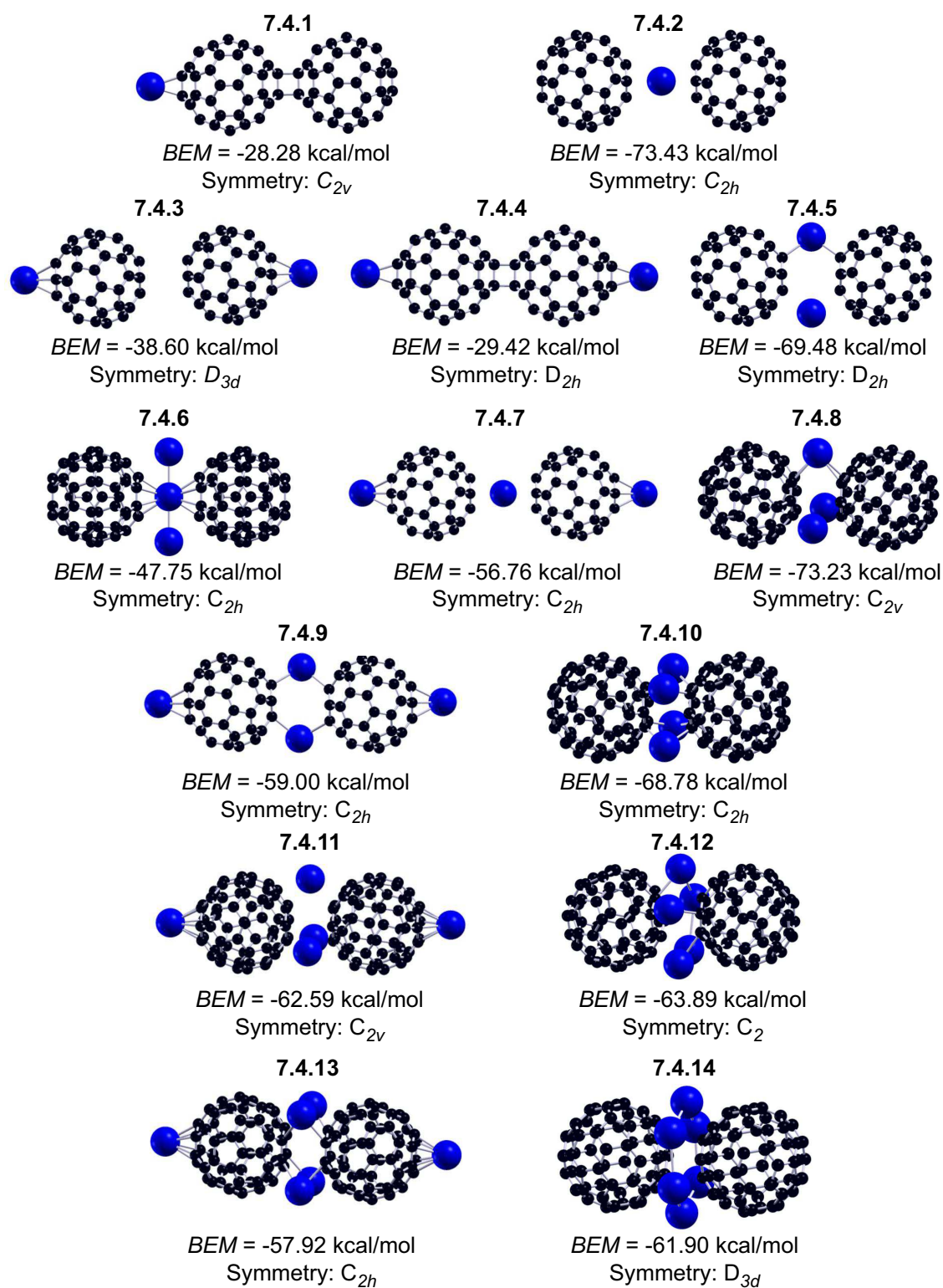


Figure 7.4: Optimized geometries and symmetries of the $Ba_n(C_{60})_2$ ($1 \leq n \leq 6$) clusters.

(D_3 and C_2 symmetries); two pentagonal rings (D_{5h} and C_{2v} symmetries) and two pentagonal rings rotated 27° with respect to each other (D_{5d} and C_{2h} symmetries). Singlet and triplet configurations were computed for all isomers with D_{5h} , D_{5d} , D_{3h} , D_{3d} and D_3 symmetries. The energies of all of the structures were within ~ 7.5 kcal/mol of each other. However, the isomer lowest in energy contained a barium atom between two hexagonal rings and C_{2h} symmetry (7.4.2). Hence, in all of the subsequent starting geometries (except 7.4.1 and 7.4.4) the two hexagonal faces of C_{60} were chosen to point towards each other. Configurations containing σ_h or σ_v symmetry operations were considered, and only the clusters with the lowest energy are shown in Fig. 7.4.

In order to clarify the nature of the bonding for the most stable structural alternatives for a given n (7.4.2, 7.4.5, 7.4.8, 7.4.10, 7.4.12 and 7.4.14) we first of all reoptimized these geometries with a higher integration accuracy and then performed a fragment orbital analysis, using the distorted fullerenes (as found in the optimized cluster) and the free Ba atoms, as fragments.¹⁰² This yielded the composition of the molecular orbitals of the metal-fullerene clusters in terms of the occupied and unoccupied orbitals of Ba and C_{60} . In $Ba(C_{60})_2$, all of the occupied orbitals, with the exception of the HOMO, were composed of occupied orbitals of the two distorted fullerenes and the Ba core and semi-core orbitals. The HOMO itself, on the other hand, was made up primarily of unoccupied C_{60} orbitals and contained some Ba $5d_{z^2}$ and $5d_{x^2-y^2}$ character (6% total). This clearly shows that an important component of the bonding in the $Ba(C_{60})_2$ cluster originates from an electron transfer from the Ba $6s$ orbital to the LUMOs of the two fullerenes. However, despite the fact that one might expect a Ba^{2+} ion to be strongly stabilized when placed between the two negatively charged C_{60} moieties, a complete transfer of the two valence $6s$ electrons to the C_{60} unoccupied orbitals does not occur. This finding is supported by a calculated Mulliken charge of 1.603 on the Ba atom. Instead, we find back donation into the empty Ba $5d$ orbitals leading to Ba $5d-C_{60}-\pi^*$ bonding, which is seen clearly in Figure 7.5. Thus, our results support the classification of Ba as an “honorary d -element” by Pyykkö *et al.*¹⁵⁴⁻¹⁵⁶ A similar analysis revealed that for $2 \leq n \leq 6$, the occupied orbitals, except for the n highest, were composed primarily of occupied C_{60} and Ba core and semi-core orbitals (in some cases a small amount of Ba $5d$ character was also present). The n highest orbitals, on the other hand, were composed primarily of the C_{60} LUMOs, other unoccupied fullerene orbitals and also contained barium $5d$ character. For $n = 5, 6$, some Ba $6s$ character could also be found.

As n increases the Ba atoms become close enough to each other so that they may also form Ba-Ba bonds, leading to the formation of a metal cluster between the C_{60} s. For example, σ -bonding between nearest neighbor Ba atoms is evident in the HOMO-3 of $Ba_6(C_{60})_2$, shown in Figure 7.6.

The aforementioned analysis illustrates that the $Ba_n(C_{60})_2$ clusters exhibit ionic bonding due to a transfer of the Ba $6s$ electrons to the unoccupied fullerene molecular orbitals (BEM_{ionic}),

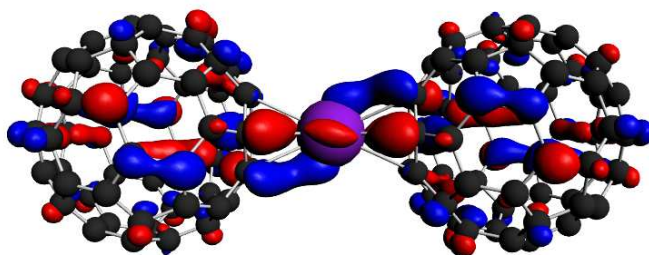


Figure 7.5: The $Ba(C_{60})_2$ HOMO, isosurface = ± 0.023 a.u. It is composed primarily of the LUMOs of the two fullerenes and contains some Ba $5d_{z^2}$ and $5d_{x^2-y^2}$ character. The Ba atom is purple, C atoms are black.

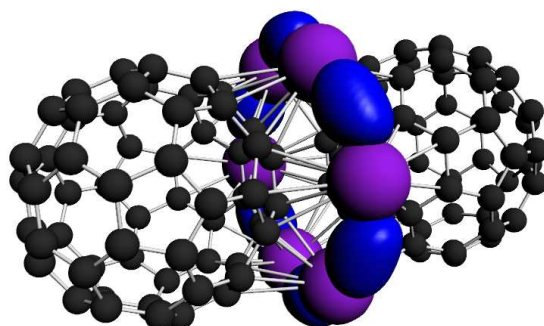


Figure 7.6: The $Ba_6(C_{60})_2$ HOMO-3, isosurface = ± 0.031 a.u. It contains primarily Ba $5d_{yz}$, $6s$ and some $C_{60}-\pi^*$ character. The Ba atoms are purple, C atoms are black.

covalent bonding between the Ba $5d$ and $C_{60}-\pi^*$ orbitals ($BEM_{covalent}$) and metal-metal bonding between the Ba atoms (BEM_{Ba-Ba}). Moreover, the fullerenes undergo small geometrical distortions from icosahedral symmetry in the formation of the clusters, (BEM_{geo}). Thus, we assumed that:

$$BEM = BEM_{ionic} + BEM_{covalent} + BEM_{Ba-Ba} + BEM_{geo}. \quad (7.3)$$

BEM_{geo} is easy to calculate exactly and varied between 2.3 to 6.6 kcal/mol. A systematic trend could not be observed. The Ba $5d$ orbitals are involved in both the Ba-Ba and covalent Ba- C_{60} bonding. Hence, a single-point energy calculation where the Ba $5d$ orbitals have been removed

from the basis set should yield approximately the ionic bonding energy. For large n however, the $6s$ orbitals also participate in Ba-Ba bonding, thus this approximation becomes less valid as n increases. In order to estimate BEM_{Ba-Ba} separately, we performed energy calculations on Ba_n clusters whose coordinates were fixed to be equivalent to those in the $Ba_n(C_{60})_2$ clusters. The BEM_{Ba-Ba} varied between -1.8 to -6.0 kcal/mol and once again no systematic trend could be found. $BEM_{covalent}$ was obtained by subtracting the geometrical, Ba-Ba and ionic bonding energies from the total bonding energy. Our approximations include various small reorganization effects. For instance, the BEM_{Ba-Ba} term as it is calculated here refers to a neutral Ba cluster whereas in the metal- C_{60} systems charge is transferred to the C_{60} moieties which will affect BEM_{Ba-Ba} to some extent. Likewise, the $BEM_{covalent}$ term also contains the change of the bonding within each Ba_n cluster upon removal of some electronic charge due to the $Ba \rightarrow C_{60}$ donation and other electronic reorganization effects. There is obviously no unique way how the total bonding energy may be split up into different contributions. We believe that our analysis is meaningful within its limitations posed by the approximations that were made, and that it offers insight into the different modes of bonding present in the $Ba_n(C_{60})_2$ clusters.

Fig. 7.7 shows the important BEM_{ionic} and $BEM_{covalent}$ contributions, along with the average Mulliken charge per Ba. Note that the BEM are slightly different than those shown in Fig. 7.4 since they were obtained using a higher integration accuracy. For $1 \leq n \leq 3$, the dominant interaction is ionic bonding. The magnitude of BEM_{ionic} decreases steadily

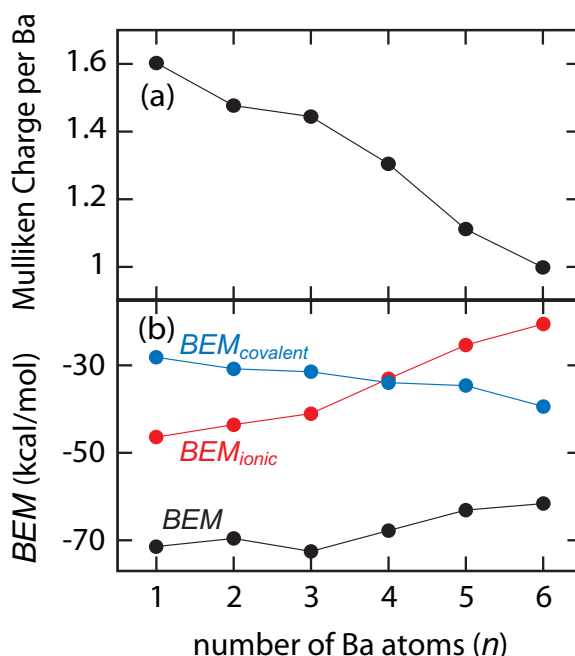


Figure 7.7: (a) average Mulliken charge per Ba and (b) relevant contributions to BEM , for the most stable $Ba_n(C_{60})_2$ ($1 \leq n \leq 6$) clusters.

with increasing n , as does the average charge per metal atom. However, the magnitude of $BEM_{covalent}$ increases with increasing n , being the dominant interaction for $n = 5, 6$. For $n = 4$, $BEM_{ionic} \sim BEM_{covalent}$. This can be understood by considering the following. For large n , full electron donation to the unoccupied fullerene orbitals cannot occur, since the electrostatic repulsion between the Ba^{2+} ions would be too large for the cluster to be stable. Instead, as n increases so does the back donation to the Ba $5d$ orbitals, stabilizing clusters where all of the Ba atoms are located between the two fullerenes. Thus, the d -element character of Ba is essential when attempting to rationalize the structural features of these clusters.

The BEM data confirm that the $Ba_3(C_{60})_2$ cluster is the most stable. Its stability results from a balance mainly between two reverse trends: on the one hand a decreasing cluster stabilization from the $Ba \rightarrow C_{60}$ electron transfer and on the other hand an increasing stability from $C_{60} \rightarrow Ba$ back donation, as n increases. However, the BEM of $Ba_2(C_{60})_2$ is only 1.1 kcal/mol higher. In order to explain the magic character of $Ba_3(C_{60})_2$, one needs to take the entropic and enthalpic contributions at 150 K into consideration. This will be done in the following section.

7.3.3 The Gibbs Free Energy of $Ba_n(C_{60})_2$ ($1 \leq n \leq 6$) Clusters

In an equilibrium mixture at constant temperature T and pressure p , it is ultimately the Gibbs free energy of a species x , $G(x)$, which determines the stability of a given structure. The Gibbs free energy is defined as

$$G(x) = H(x) - TS(x). \quad (7.4)$$

Here $H(x)$ and $S(x)$ are the enthalpy and entropy at the given temperature and pressure. The former is a sum of the energy of the species at 0 K plus the finite temperature enthalpy contribution,

$$H(x) = E(x) + H_{EC}(x). \quad (7.5)$$

Both $H_{EC}(x)$ and $S(x)$ are a sum of terms arising from rotational, translational, vibrational and electronic degrees of freedom. Upon defining $H_{EC}M$ and $-TSM$ as the change in the finite temperature enthalpy correction per metal atom and the change in entropy per metal atom, multiplied by the temperature, for reaction 7.1, then GFM may be written as

$$GFM = BEM + H_{EC}M - TSM. \quad (7.6)$$

In the previous section we considered the first term of Eq. 7.6, BEM . Within this section we will analyze the last two terms and finally the GFM itself.

Fig. 7.8(a) shows that $-TSM$ decreases with increasing n , implying that the entropic contribution to the GFM destabilizes larger clusters to a lesser extent than smaller ones. To understand why this should be the case consider a reaction between $2n C_{60}$ molecules and n Ba atoms. The two limiting cases would be the production of the largest and the smallest possible

clusters. The former would yield $Ba_n(C_{60})_2$ and $(2n-2)C_{60}$, a total of $2n-1$ molecules, and the latter $n(Ba(C_{60})_2)$, a total of n molecules. Clearly, the formation of the largest possible cluster, along with $(2n-2)$ free fullerenes is entropically more favourable, since a greater amount of molecules are produced. In general H_{ECM} becomes less negative with increasing n , as can be seen in Fig. 7.8(b). The only exception is that $H_{ECM}(Ba_3(C_{60})_2) \sim H_{ECM}(Ba(C_{60})_2)$. The finite temperature enthalpy correction stabilizes smaller clusters, however it is about an order of magnitude smaller than the entropic term and therefore has little effect on the total GFM .

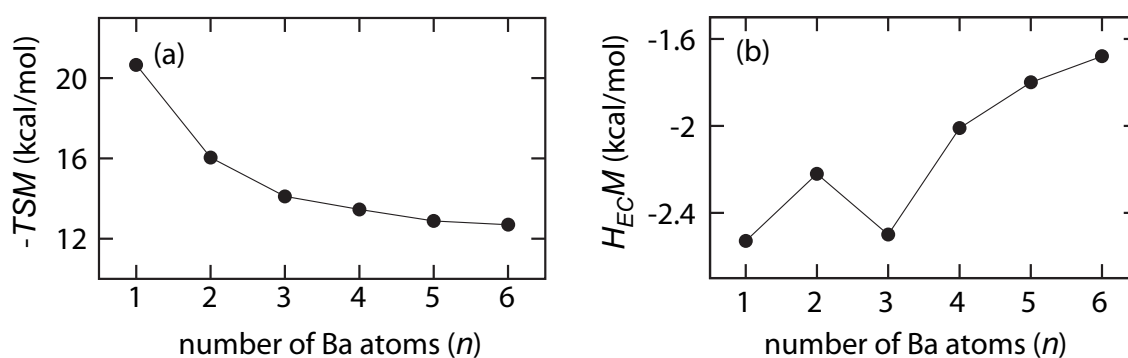


Figure 7.8: (a) $-TSM$ and (b) H_{ECM} , at the experimental temperature (150 K) and pressure (10^{-6} Torr) for the most stable $Ba_n(C_{60})_2$ ($1 \leq n \leq 6$) clusters.

In full agreement with experimental data, the total GFM given in Fig. 7.9 shows that at 150 K and 10^{-6} Torr, $Ba_3(C_{60})_2$ is magic. The BEM alone indicates that this is also the most stable structure. However, the finite temperature corrections change the order of stability. In particular, the GFM of $Ba_4(C_{60})_2$ and $Ba_2(C_{60})_2$ are less than that of $Ba(C_{60})_2$, whereas the opposite is true when only the BEM data is taken into consideration. This clearly underlines the importance of calculating the enthalpic and, even moreso, entropic contributions to the Gibbs free energy when determining absolute cluster stability. Calculations of the GFM at 300 K and 600 K (not shown) predict that the $n = 3$ cluster remains magic up to at least these temperatures. Unfortunately, a small error in the calculated entropies propagates to a large error in the GFM at high temperatures (S is multiplied by T). Therefore we cannot predict which cluster is the most stable at 1780 K, the temperature of the heating stage.

The calculations show that the $Ba_n(C_{60})_2$ clusters have many local minima, which are all very close in energy to each other, differing only in a rotation of the C_{60} s around the metal core. This suggests that perhaps configurational entropy is also important in determining the absolute stability of the clusters. Since the configurational entropy for the free C_{60} s and metal atoms is zero, the change in configurational entropy per metal atom, $S_{conf}M$, for reaction 7.1 is given as

$$S_{conf}M = (k_B \ln W)/n, \quad (7.7)$$

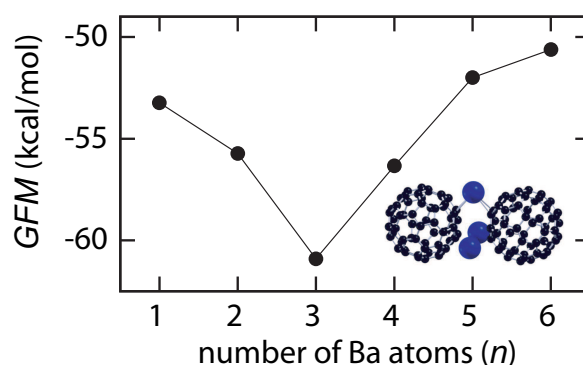


Figure 7.9: GFM at the experimental temperature (150 K) and pressure (10^{-6} Torr) for the most stable $Ba_n(C_{60})_2$ ($1 \leq n \leq 6$) clusters. The $n = 3$ cluster, also shown, has the lowest GFM .

where W is the number of configurations and k_B is the Boltzmann constant. It is unclear how one may determine W , and instead we will calculate the amount of configurations necessary to have a noticeable impact on the total entropy. We find that W should be approximately equal to 29, 821 and 3.73×10^{14} in order to change the entropy by 1, 2 and 10 kcal/mol, respectively. With this in mind, it is unlikely that inclusion of $S_{conf}M$ would affect the total GFM by more than a couple of kcal/mol. For the Ba clusters at 150 K this will not change the order of stability.

7.3.4 Bonding and Stability of $K_n(C_{60})_2$ ($1 \leq n \leq 6$) Clusters

In Section 7.3.1 it was shown that the favoured bonding mode for potassium and barium to a single C_{60} was the same (configurations where the metal atom lay on top of a hexagonal fullerene face had the lowest BEM). This indicates that the two metals may also prefer the same geometries when bonding with two C_{60} s. Thus, for the $K_n(C_{60})_2$ clusters we have not optimized species which were found to be much higher in energy than the most stable $Ba_n(C_{60})_2$ clusters (7.4.1, 7.4.3, 7.4.4, 7.4.6 in Fig. 7.4). Instead, we have primarily focused on structures belonging to Set A and Set B defined in Section 7.3.2. We have optimized clusters containing σ_h or σ_v symmetry operations, and only those lowest in energy are shown in Fig. 7.10, along with the BEM . Clearly, for ($1 \leq n \leq 4$) potassium bonds in a similar fashion as barium to the two C_{60} s. However, for $n = 5, 6$, geometries belonging to Set B are preferred. For $n = 5$, the BEM difference between the two Sets is quite small, but it is seen to increase substantially for $K_6(C_{60})_2$.

In order to clarify the nature of the bonding we reoptimized the most energetically stable moieties, then performed a fragment orbital analysis, using the distorted C_{60} s and the K atoms as fragments. This showed that the bonding is purely of an ionic nature, with an almost full transfer

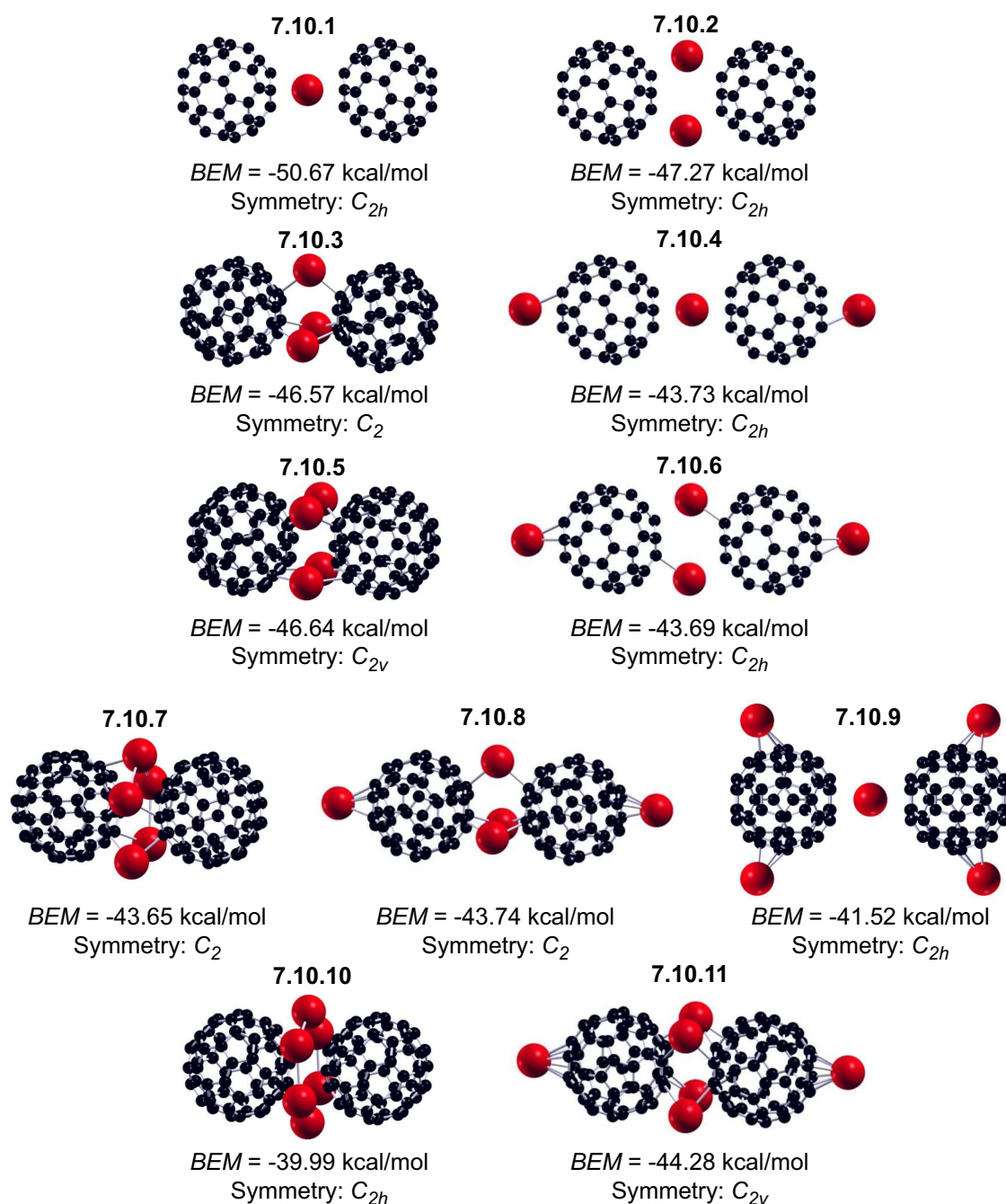


Figure 7.10: Optimized geometries and symmetries of the $K_n(C_{60})_2$ ($1 \leq n \leq 6$) clusters.

of the valence potassium [$4s^1$] electron to the LUMO of the C_{60} s. For $n = 1, 2$ analysis of the cluster orbitals confirmed that the HOMOs were composed solely of the fullerene LUMOs. For $n = 4, 6$ the highest $n/2$ orbitals and for $n = 3, 5$ the highest doubly occupied $(n-1)/2$ orbitals plus the singly occupied HOMO (SOMO), consisted only of contributions from the unoccupied orbitals of the fullerenes.

As one might have expected, for large n the electron transfer from the potassium atoms to the C_{60} moieties is not complete because of the increasing Coulomb repulsion between the K^+ ions, see Fig. 7.11. The same trend was observed for K_nC_{60} clusters as shown in Section 7.3.1. We roughly estimated the purely electrostatic energy for the different clusters by assigning each atom the calculated Mulliken charge. We found that for $n = 3, 4$, the total electrostatic energy was more negative for the clusters from Set A, whereas Set B afforded lower electrostatic energies for $n = 5, 6$, indicating that the preferred geometries tend to minimize the total electrostatic energy. For large amounts of K, the clusters from the first Set are less stable than those from the second due to the fact that the close proximity of the positively charged K atoms results in an increased Coulomb repulsion. For the Ba clusters, on the other hand, the Ba d -element character compensates for this effect by allowing for a $C_{60} \rightarrow$ Ba back donation of charge such that the clusters of Set A remain the most stable at least up to $n = 6$.

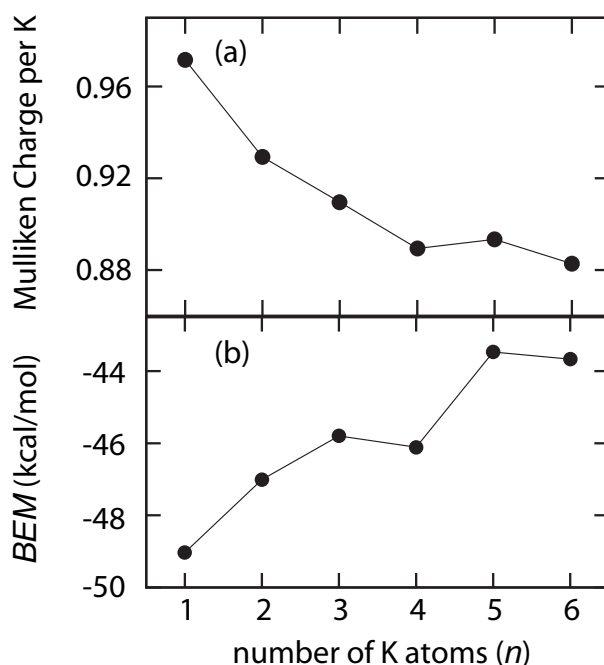


Figure 7.11: (a) average Mulliken charge per K and (b) BEM , for the most stable $K_n(C_{60})_2$ ($1 \leq n \leq 6$) clusters.

Fig. 7.11 illustrates that in general the BEM decreased in magnitude as n increased. These numbers are slightly different than those shown in Fig. 7.10 since the geometries were reoptimized with a higher integration accuracy. A certain amount of energy is gained by transferring a valence K $[4s^1]$ electron to the fullerene unoccupied orbitals. At the same time, the addition of more and more K atoms also results in an increase of the Coulomb repulsion between them. Hence, overall the energy gained by adding a K atom to the cluster decreases as n in-

creases. Once again this finding correlates with those in Section 7.3.1. It must be pointed out that $K_4(C_{60})_2$ and $K_6(C_{60})_2$ were slightly more stable than $K_3(C_{60})_2$ and $K_5(C_{60})_2$, respectively. This is due to the fact that clusters with $n = 4, 6$ afford an even number of electrons and hence a full electronic shell whereas the valence shells for clusters with $n = 3, 5$ are only half full. Our calculations and those of others^{134,135} show that for clusters containing one and two fullerenes, the K atoms prefer to be located on top of hexagonal faces. Thus, $K(C_{60})_2$ is more stable than $K_2(C_{60})_2$, despite the fact that it has only a half full valence shell, due to the fact that the K sits directly between two hexagonal fullerene faces.

7.3.5 The Gibbs Free Energy of $K_n(C_{60})_2$ ($1 \leq n \leq 6$) Clusters

The vibrational frequencies for the most stable potassium clusters of a given n were calculated. This yielded the entropic, Fig. 7.12(a) and enthalpic, Fig. 7.12(b) contributions to the *GFM*. In general, the same trends were observed as for the barium clusters: the entropic term destabilized larger clusters to a lesser extent than smaller ones and the enthalpic term stabilized smaller clusters. However, the latter term was about an order of magnitude smaller than the former and therefore did not substantially affect the total *GFM*.

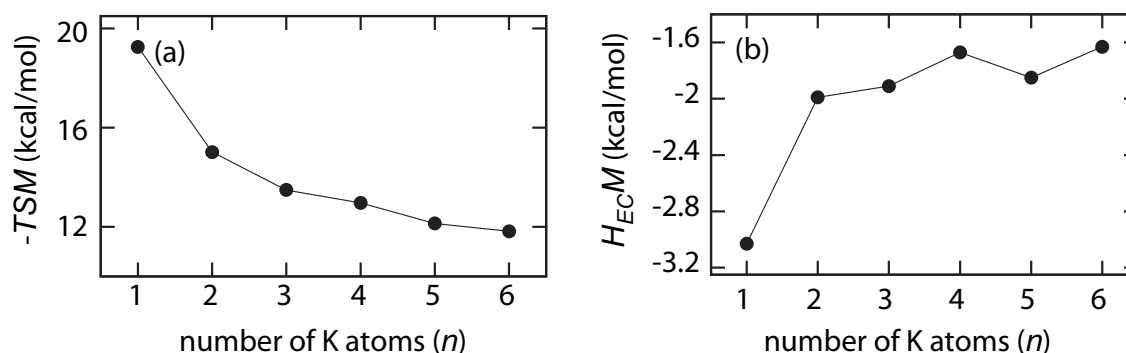


Figure 7.12: (a) $-TSM$ and (b) H_{ECM} , at the experimental temperature (150 K) and pressure (10^{-6} Torr) for the most stable $K_n(C_{60})_2$ ($1 \leq n \leq 6$) clusters.

In full agreement with experimental data, the total *GFM* given in Fig. 7.13 shows that at 150 K and 10^{-6} Torr, $K_4(C_{60})_2$ is magic. Here, even more so than for the Ba clusters, it is vital to take into account finite temperature effects when determining absolute stability. The most energetically stable configurations were: $K(C_{60})_2 < K_2(C_{60})_2 < K_4(C_{60})_2 < K_3(C_{60})_2 < K_6(C_{60})_2 < K_5(C_{60})_2$. The *GFM*, on the other hand, revealed a different order of stability: $K_4(C_{60})_2 < K_3(C_{60})_2 < K_2(C_{60})_2 < K_6(C_{60})_2 < K_5(C_{60})_2 < K(C_{60})_2$. In fact, calculations of the *GFM* at different temperatures (not shown) predict that $K(C_{60})_2$, $K_4(C_{60})_2$ and $K_6(C_{60})_2$ are magic at 75 K, 300 K and 600 K. It was shown previously that at 150 K the configurational

entropy may contribute around 1-2 kcal/mol to the total GFM . For the Ba clusters such changes were deemed unimportant in determining the order of stability, however this might not be the case for the K clusters since the GFM are all very close in energy. Nonetheless, the calculated results are in-line with experiment, suggesting that configurational entropy does not have a major influence on the total Gibbs free energies, or that $S_{conf}M$ is approximately the same for the different clusters.

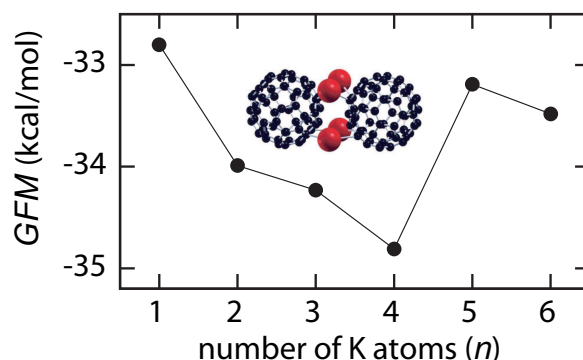


Figure 7.13: GFM at the experimental temperature (150 K) and pressure (10^{-6} Torr) for the most stable $K_n(C_{60})_2$ ($1 \leq n \leq 6$) clusters. The $n = 4$ cluster, also shown, has the lowest GFM .

7.3.6 Energetics of Doubly and Singly Charged Clusters

We have also calculated the energy difference between $M_n(C_{60})_2$ ($M = K, Ba$) and the corresponding singly or doubly charged clusters, shown in Table 7.2. If these values are to be associated with the energy needed to singly or doubly ionize the clusters, then it can be concluded that the ionization energy decreases as n increases for both metals. Moreover, the laser pulse used ($7.9 \text{ eV} \sim 182.2 \text{ kcal/mol}$) had enough energy to singly ionize the clusters. The pulse could also ionize a singly charged species, yielding a doubly charged cation. However, the laser was not strong enough to create $M_n(C_{60})_2^{2+}$ from $M_n(C_{60})_2$. The cations are highly unstable compared to the neutral clusters. It is also interesting to note that the ionization of a barium cluster with a given n requires approximately the same energy as the potassium analogue. The first and second ionization energies for $K_5(C_{60})_2$ and $K_6(C_{60})_2$ reveal that it is somewhat easier to ionize a structure belonging to Set B as opposed to Set A.

Table 7.2: The energy differences between (a) $M_n(\text{C}_{60})_2$ and $M_n(\text{C}_{60})_2^+$, (b) $M_n(\text{C}_{60})_2$ and $M_n(\text{C}_{60})_2^{2+}$ ($M = \text{K}, \text{Ba}$) clusters. All energies given in kcal/mol.

n	$\text{Ba}_n(\text{C}_{60})_2^+$	$\text{Ba}_n(\text{C}_{60})_2^{2+}$	$\text{K}_n(\text{C}_{60})_2^+$	$\text{K}_n(\text{C}_{60})_2^{2+}$
1	125.48	302.96	123.85	-
2	125.38	299.96	119.12	285.47
3	116.90	286.63	115.84	280.08
4	113.85	281.50	112.69	278.47
5	109.53	270.80	94.11	240.66
6	111.15	271.88	94.24	236.04

7.4 Summary and Conclusions

The preliminary study on $M\text{C}_{60}$ ($M = \text{K}, \text{Ba}$) clusters indicated that the preferred bonding mode for both metals is to lie on top of a hexagonal fullerene face. The Mulliken charges revealed an almost full transfer of the potassium $[4s^1]$ valence electron to the fullerene, however for barium a transfer of both valence $[6s^2]$ electrons was not observed. Geometries for possible K_nC_{60} ($1 \leq n \leq 6$) and Ba_nC_{60} ($n = 1, 2, 3$) structures were also optimized. The Mulliken charges on the metals decreased as n increased, in accordance with previous computational studies.^{134,135} KC_{60} and Ba_2C_{60} afforded the lowest *BEM*.

An extensive study of different possible $\text{Ba}(\text{C}_{60})_2$ isomers showed that the barium atom prefers to lie between two hexagonal C_{60} faces. The most stable structural alternatives for $\text{Ba}_n(\text{C}_{60})_2$ ($1 \leq n \leq 6$) all belonged to Set A, with the Ba atoms sandwiched between the two fullerenes. Ionic bonding, arising from an incomplete transfer of the valence $[6s^2]$ electrons to the unoccupied fullerene orbitals, was found to be the dominant bonding mechanism for small n . As n increased, covalent bonding between the Ba $5d$ and $\text{C}_{60}-\pi^*$ orbitals increased, being the dominant bonding mechanism for $n = 5, 6$. This occurred as a result of $\text{C}_{60} \rightarrow \text{Ba}$ back donation into the empty $5d$ orbitals. Metal-metal bonding between the Ba atoms was also found, however it was about an order of magnitude smaller than the aforementioned bonding mechanisms. Thus, for the barium clusters the energetically most stable structures and their geometries are determined by an interplay between ionic and covalent bonding. On the other hand, the $\text{K}_n(\text{C}_{60})_2$ ($1 \leq n \leq 6$) clusters exhibited only ionic bonding arising from a transfer of the $[4s^1]$ valence electrons into unoccupied C_{60} orbitals. The most stable geometries were found to minimize the total electrostatic energy. For $1 \leq n \leq 4$ isomers from Set A were the most stable, whereas for $n = 5, 6$, Set B afforded structures with lower energies.

An analysis of the finite temperature contributions to the *GFM* revealed that the entropic

term tends to destabilize larger clusters to a lesser extent than smaller ones. This is due to the fact that a reaction yielding a single large cluster and many free fullerene molecules has greater entropy than one forming many small clusters and no or few free C_{60} s. The enthalpic term was seen to stabilize small clusters, however it was about ten times smaller compared to the entropic term. In full agreement with experimental results, the *GFM* indicated that $Ba_3(C_{60})_2$ and $K_4(C_{60})_2$ are the most stable structures, and therefore appear as magic clusters, at the experimental temperature and pressure. Calculation of thermodynamic quantities was shown to be essential in determining which of the potassium containing clusters are magic: different temperatures changed the order of stability. Due to the formidable computational cost of calculating vibrational frequencies for such large systems, currently only a few studies, for example Refs. 157–159, are available which specifically consider the Gibbs free energies in determining absolute cluster (oligomer) stability.

Despite the fact that the theoretical and experimental results agree, there are many open questions as to what actually occurs in the experiment. For example, is the measured cluster distribution formed during the heating or the cooling stage and does the ionization procedure affect the distribution? The calculations strongly suggest the following interpretation of the experiment. A certain cluster distribution forms at the source. In the heating stage it is necessary to provide enough energy so that the clusters can overcome the activation barrier to break bonds in these initial meta-stable structures. If the temperature and dwell time in the heating stage are not high and long enough then clusters formed at the source will be present when they enter the cooling stage. The clusters must first overcome the activation barrier necessary in order to reach the structure which is the global minimum on the PES at the given temperature. Next, it is presumed that the clusters reach an equilibrium distribution for the temperature found in the heating stage. The intensities show that few clusters survive this heating stage suggesting that the heating temperature is close to the threshold where all of the clusters decompose, ie. where *GFM* becomes positive for all of the clusters. After exiting the heating stage the clusters are cooled to 150 K, then photoionized and measured by TOF mass spectrometry. Unless the clusters are much more kinetically stable than we expect, the cooling stage should yield clusters which are thermodynamically stable at that temperature and not at the temperatures obtained during the heating. The calculations show that at low temperatures clusters with a smaller amount of metal atoms are more stable. Thus, it is likely that the clusters formed at high temperatures emit some metal atoms upon cooling. We do not know the activation barrier for this process but predict it to be relatively small. This is due to the fact that the clusters exit the heating stage with a high energy and with all of the atoms vibrating quickly. It is likely that these vibrations will yield enough energy to emit a few metal atoms from the cluster. Unfortunately, we are unable to make any predictions about the cluster distribution within the heating stage due to the fact that at high temperatures a small error in the entropy would propagate to a large error

in the *GFM* (S is multiplied by T). For such systems *ab initio* molecular-dynamics (MD) simulations would be prohibitively expensive and MD would be unreliable since it requires as an input interaction potentials, which are unknown in this case. Thus, the computational method employed is the most sophisticated possible. One way to experimentally determine if this interpretation is correct would be to determine if varying the temperature of the cooling stage changes the distribution of the K clusters, as the calculations predict.

Part III

Summary

Chapter 8

Conclusions and Outlook

Within this thesis density functional calculations have been carried out on a variety of different systems of chemical and physical interest. Band structure calculations on insulators, semi-metals and metals have been performed. It was shown how one may construct Wannier-like orbitals for a number of compounds and how these orbitals may be used for analysis purposes. The bonding and properties of metal-C₆₀ clusters and SWNT fragments was examined via molecular calculations. In particular, the ¹³C NMR chemical shifts for a number of finite nanotube fragments were calculated and the geometries and stability of Ba_{*n*}(C₆₀)₂ and K_{*n*}(C₆₀)₂ ($1 \leq n \leq 6$) clusters was investigated. The application of DFT based periodic and quantum chemical codes to study the electronic structure and properties of various systems shows that DFT is a versatile and useful tool in both solid state physics and theoretical chemistry.

Part I: Solids

An Introduction to *NMTO* Wannier-like Functions

The *NMTO* method has been employed to generate Wannier-like functions for the π and σ bands of graphite and boron nitride. We have shown that it may be used to design a basis of atom-centered localized orbitals, which span the wave function in a given energy range. The energy mesh determines which bands, bonding or anti-bonding, are described by the method. This was demonstrated by constructing Wannier-like orbitals for just the occupied or unoccupied π -bands in graphite. The orbitals are seen to be in-line with a chemical picture of bonding in the solid state and may therefore be useful as a tool for analysis. Currently the orbitals are not maximally localized, but we have shown how this may be achieved by performing tight-binding calculations on the benzene π -bond.

Theoretical Studies of High Pressure Cesium

The band structures of Cs-I (bcc), Cs-II (fcc) and Cs-IV (tetragonal) were calculated. The pressure induced electronic $s \rightarrow d$ transition was confirmed. It was noted that near the

experimental vicinity of the Cs-I \rightarrow Cs-II, Cs-II \rightarrow Cs-III and Cs-IV \rightarrow Cs-V transitions, a Lifshitz transition (change in the topology of the Fermi surface) is predicted computationally. FP-LMTO calculations revealed a softening of the $T_{[1\bar{1}0]}[\xi\xi0]$ phonon mode which becomes imaginary around $\xi = 1/3$ for Cs-II at a volume of approximately $0.40v_0$. A large electron-phonon coupling was also calculated for this wave vector. It was postulated that Fermi surface nesting between pockets arising from the Lifshitz transition are at least partially responsible for the structural instability. Future work could include calculation of the nesting function in the manner described within Ref. 66. Moreover, the phonon spectra and electron-phonon coupling for the other structural transitions occurring near a calculated Lifshitz transition could be computed in order to determine if all of the structural instabilities have a similar origin.

A procedure by which one may generate Wannier-like functions for only the occupied bands in a metal was proposed. In principle, it is necessary to find an appropriate supercell where the bands have cusps touching the Fermi level. However, much smaller cells were found to reproduce the rough shape of the orbital. The NMTOs for Cs-I, Cs-II ($v/v_0 = 0.6, 0.4$) and Cs-IV have been calculated in order to visualize the pressure induced $s \rightarrow d$ electronic transition. For Cs-I the orbital is completely spherical and in Cs-II ($v/v_0 = 0.6$) four d -like lobes are seen to develop. Two of these lobes are raised and two are lowered upon increasing pressure. Raising and lowering of these lobes even further yields the orbital calculated for Cs-IV. This NMTO was found to reproduce the charge density calculated by standard electronic structure methods.

Further work could include calculation of the Cs-III NMTOs. Due to the fact that the unit cell contains 84 atoms, it would not be necessary to construct a supercell in order to create a Wannier-like function for only the occupied bands. The main difficulty would be to determine where the orbitals should be placed and where they should be downfolded. Currently the calculated orbitals are symmetry breaking. The implementation of a scheme in which the NMTOs are symmetrized through a maximal localization procedure could provide further insight on the pressure induced electronic transition.

The stability of the Cs-IV structure was explained via the splitting of the xz/yz bands near the N -point. At this wave vector the orbitals show $dd\delta\pi$ -bonding/anti-bonding interactions for the occupied and unoccupied band, respectively, along the direction of maximum electron density. The lobes of the calculated Wannier-like orbitals were also found to point in the same direction as the lobes of the orbitals which form $dd\delta\pi$ -bonds.

The Electronic Structure of α -ThSi₂ and β -ThSi₂

The band structures of α -ThSi₂ and β -ThSi₂ have been studied using TB-LMTO and the newly developed NMTO method, which was used to generate Wannier-like functions for selected groups of bands. Even for these intermetallic compounds, it was possible to generate a truly minimal basis set which described most of the occupied bands correctly. It was shown that the

bonding within both systems could be understood in a similar way. The lowest bands arose from σ -bonding within the silicon sublattice. The sp^2 NMTOs were similar to those obtained for graphite, however a small amount of hybridization with the Th atoms was found. In β -ThSi₂ the next set of bands higher in energy could be described by a Si π -bonding orbital which hybridized strongly with the d_{z^2} orbitals on the nearest neighbour Th atoms. For α -ThSi₂ the π -bonding bands also hybridized with the uppermost σ -bonding band due to the z -connections between the zig-zag chains running in the x and y directions. For both structures, the occupied band structure could be quite well described by a basis consisting of Si σ -bonding, π -bonding and $s^*\pi^*$ orbitals. The latter hybridize forming two $s^*\pi^*$ NMTOs which have large d_{z^2} -like tails on the six neighbouring Th atoms. This interpretation shows that for α -ThSi₂/ β -ThSi₂, there are 12/6 electrons in the Si σ -bands, 4/2 electrons in the Si π -bonding bands and 8/4 electrons in the Si $s^*\pi^*$ orbitals (since α -ThSi₂ and β -ThSi₂ contain 2 and 1 formula units in the unit cell, respectively). Formally, this leads to a Th⁴⁺/Si²⁻ valence electronic configuration. However, the Si π -bonding and especially the Si $s^*\pi^*$ orbitals show large tails on the thorium atoms implying that not all of the charge is completely transferred to silicon.

For α -ThSi₂ an alternative truly minimal basis set was proposed, based upon the calculations for Cs-IV. The thorium atoms are located in the same positions as the cesiums and the band width for both elements is similar. A basis composed of Si σ -bonding, π -bonding and anti-bonding NMTOs as well as an s -like orbital on every thorium atom (Th s/s^* basis) reproduced the occupied bands quite well. This formally yields a Th²⁺/Si⁻ valence electronic configuration. The Th Wannier-like function resembled the s -like orbital calculated for Cs-IV, except that it had one and not two lobes which pointed along the center of the prisms. However, this orbital was not symmetric with respect to the lattice and it would be necessary to construct a maximally localized symmetric NMTO in order to make a definite comparison of the orbitals and bonding present in the two metals. Future work should therefore focus on the implementation of an automatic maximal localization scheme.

Part II: Molecules

The ¹³C NMR Chemical Shifts in (9,0) Carbon SWNTs

Density functional calculations on the electronic structure and ¹³C NMR chemical shifts of finite (9,0) SWNTs were performed. Two different models for the finite systems were considered: the dangling bonds were saturated (capped) with either hydrogen or with half of a C₆₀. Computations on progressively longer fragments were carried out in order to determine if the properties converge with respect to increasing length. In agreement with computational and experimental work, the C₃₀-terminated tubes were predicted to have a finite band gap. The HOMOs and LUMOs were delocalized over the whole fragment. In contrast, the H-capped SWNTs were found to be metallic, even at relatively short lengths. Analysis of the frontier

orbitals showed that they need to be considered as artifacts when comparing with the infinite systems. Thus, it was concluded that the latter are not necessarily good models for infinite SWNTs, whereas the former appear to yield results in-line with experiments and theoretical work on periodic systems. Moreover, the convergence of the HOMO and LUMO energies, band gaps and chemical shifts appeared to be somewhat faster for structures capped by fullerene hemispheres. Thus, it was proposed that the chemical shift of an infinite (9,0) SWNT should be approximately equivalent to the shift of a central carbon atom in the longest C_{30} -terminated system considered, about 130 ppm. Previous theoretical work suggested that metallic SWNTs should be 11 ppm less shielded than semiconducting ones.⁹⁵ Therefore, under the assumption that the (9,0) tube yields a shift typical of other semiconducting tubes, it was predicted that the chemical shift of metallic tubes should be close to that of C_{60} . These results indicate that NMR may be a useful tool in the characterization of a heterogeneous mixture of SWNTs.

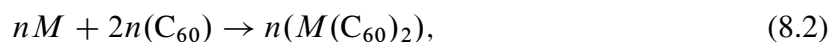
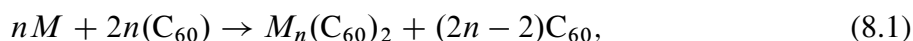
The results of Latil et al. suggest that the chemical shifts of the semiconducting nanotubes should not be very sensitive to the helicity and diameter of the tube.⁹⁵ However, the calculations employed a tight-binding model with one π electron per site and in order to verify this conjecture density functional calculations on finite and infinite systems should be performed. For finite tubes, one would first need to construct appropriate caps composed of fullerene hemispheres. Next, the electronic structure of the capped tubes must be investigated in order to determine if the results agree with predictions from periodic calculations, or if the capping has a large influence on the properties. Recently DFT calculations have examined how fullerene hemispheres influence the geometry and vibrational structures of finite nanotubes.^{90,160,161} It would also be interesting to use solid state codes to calculate the shifts of infinite systems. The effect of functionalization could be another topic of investigation. Finally, metallic tubes may be studied and it should be verified if the Knight shift is indeed negligible, as was previously suggested.⁹⁵

Magic $(C_{60})_n$ -Metal Compound Clusters

Geometry optimizations of a number of possible structures for $Ba_n(C_{60})_2$ ($1 \leq n \leq 6$) showed that in all cases the most stable isomer affords Ba atoms sandwiched between the two fullerenes. The main bonding mechanisms were determined to be ionic and covalent, for $n \leq 3$ and $n = 5, 6$, respectively. The former arises from an incomplete transfer of the valence $[6s^2]$ electrons into the empty fullerene orbitals. The latter is due to $C_{60} \rightarrow Ba$ back donation into the empty Ba $5d$ orbitals which undergo covalent bonding with the fullerene MOs. Due to the close proximity of the Ba atoms, metal-metal bonding was also present, however its contribution to the total bonding energy was about an order of magnitude smaller than the aforementioned mechanisms. Thus, the geometries of the energetically most stable isomers were found to be determined primarily by an interplay between covalent and ionic bonding. On the other hand,

a simple model showed that the most energetically favourable $K_n(C_{60})_2$ ($1 \leq n \leq 6$) clusters tend to minimize the total electrostatic energy. Accordingly, they only exhibited ionic bonding due to a transfer of the $[4s^1]$ valence electrons into unoccupied C_{60} orbitals. For $n \leq 4$, and $n = 5, 6$ the preferred geometries had a $C_{60}-K_n-C_{60}$ and a $K-C_{60}-K_{n-2}-C_{60}-K$ configuration, respectively.

For both metals, the entropic contribution to the Gibbs free energy was found to destabilize larger clusters to a lesser extent than smaller ones. This was explained by noting that Reaction 8.1 produces more molecules than Reaction 8.2 and therefore is entropically more favourable:



with $M = K, Ba$. It was argued that the configurational entropy should not affect the order of stability of the Ba clusters at 150 K and probably have little influence for the K clusters as well. The enthalpic contribution to the Gibbs free energy was found to be an order of magnitude smaller than the entropic one. In full agreement with experiment $Ba_3(C_{60})_2$ and $K_4(C_{60})_2$ were found to be magic at the experimental temperature (150 K) and pressure (10^{-6} Torr). Inclusion of finite temperature effects was found to be crucial in determining which of the K clusters is the most stable. It was found that $K(C_{60})_2$, $K_4(C_{60})_2$ and $K_6(C_{60})_2$ are magic at 75 K, 300 K and 600 K. In contrast, the $Ba_3(C_{60})_2$ cluster was the preferred structure within the temperature range of 0 K-600 K. Nonetheless, inclusion of finite temperature corrections was found to change the order of stability for clusters with $n \neq 3$.

The agreement between experiment and theory suggests that the measured cluster distribution is formed in the cooling stage. However this is still unclear and further experiments which vary not only the heating temperature, but also that of the cooling stage could be performed to verify if this interpretation is correct. It would also be interesting to calculate the activation energy and find the transition state for a cluster emitting a metal atom. Since C_{60} and SWNTs have very similar structures it is conceivable that nanotube-metal clusters may also be highly stable. One could perform such calculations using the finite (9,0) fragments capped by half of a fullerene as models. The electronic structure and properties of these clusters could also be investigated.

Bibliography

- [1] Hohenberg, P.; Kohn, W. *Phys. Rev.* **1964**, *136*, B864.
- [2] Kohn, W.; Sham, L. J. *Phys. Rev.* **1965**, *140*, A1133.
- [3] Andersen, O. K. Comments on the KKR Wavefunctions; Extension of the Spherical Wave Expansion Beyond the Muffin Tins. In *Computational Methods in Band Theory*; Marcus, P. M.; Janak, J. F.; Williams, A. R., Eds.; Plenum: New York, 1971.
- [4] Skriver, H. *The LMTO Method*; Springer: New York, 1984.
- [5] Gaunt, J. A. *Phil. Trans. Roy. Soc. (London)* **1929**, *228*, 151.
- [6] Andersen, O. K.; Jepsen, O.; Glötzel, D. Canonical Description of the Band Structures of Metals. In *Highlights of Condensed-Matter Theory*; Bassani, F.; Fumi, F.; Tosi, M., Eds.; North-Holland: New York, 1985.
- [7] Andersen, O. K. *Phys. Rev. B.* **1975**, *12*, 3060.
- [8] Weyrich, K. H. *Phys. Rev. B.* **1988**, *37*, 10269.
- [9] Wannier, G. H. *Physical Review* **1937**, *52*, 191.
- [10] Kohn, W. *Physical Review* **1959**, *115*, 809.
- [11] Wannier, G. H. *Rev. Mod. Phys.* **1962**, *34*, 645.
- [12] Kohn, W. *Phys. Rev. B.* **1973**, *7*, 4388.
- [13] Koster, G. F. *Phys. Rev.* **1953**, *89*, 67.
- [14] Marzari, N.; Vanderbilt, D. *Phys. Rev. B.* **1997**, *56*, 12847.
- [15] Boys, S. F. *Revs. Modern Phys.* **1960**, *32*, 296.
- [16] Souza, I.; Marzari, N.; Vanderbilt, D. *Phys. Rev. B.* **2002**, *65*, 035109.

- [17] Andersen, O. K.; Saha-Dasgupta, T. *Phys. Rev. B.* **2000**, *62*, R16219.
- [18] Savrasov, S. Y. *Phys. Rev. B.* **1996**, *54*, 16470.
- [19] Savrasov, S. Y.; Savrasov, D. Y. *Phys. Rev. B.* **1996**, *54*, 16487.
- [20] Autschbach, J.; Ziegler, T. *Coord. Chem. Rev.* **2003**, *238/239*, 83-126.
- [21] Hehre, W. J.; Radom, L.; Schleyer, P. v. R.; Pople, J. A. *Ab Initio Molecular Orbital Theory*; John Wiley and Sons: New York, 1986.
- [22] Car, R.; Parrinello, M. *Phys. Rev. Lett.* **1997**, *55*, 2471.
- [23] Silvestrelli, P. L.; Marzari, N.; Vanderbilt, D.; Parrinello, M. *Solid State Communications* **1998**, *107*, 7.
- [24] Boero, M.; Parrinello, M.; Hüfner, S.; Weiss, H. *J. Am. Chem. Soc.* **2000**, *122*, 501.
- [25] Andersen, O. K.; Saha-Dasgupta, T.; Tank, R. W.; Arcangeli, C.; Jepsen, O.; Krier, G. *Electronic Structure and Physical Properties of Solids. The Uses of the LMTO Method. (Lecture notes in Physics, vol. 535).* In ; Dreyssé, H., Ed.; Springer: Berlin/Heidelberg, 2000.
- [26] Tank, R. W.; Arcangeli, C. *Phys. Stat. Sol.(b)* **2000**, *217*, 89.
- [27] Andersen, O. K.; Saha-Dasgupta, T.; Ezhov, S. *Bull. Mater. Sci.* **2003**, *26*, 19.
- [28] Pavarini, E.; Biermann, S.; Poteryaev, A.; Lichtenstein, A. I.; Georges, A.; Andersen, O. K. *Phys. Rev. Lett.* **2004**, *92*, 176403.
- [29] Pavarini, E.; Yamasaki, A.; Nuss, J.; Andersen, O. K. *New J. Phys.* **2005**, *7*, 188.
- [30] Müller, T. F. A.; Anisimov, V.; Rice, T. M.; Dasgupta, I.; Saha-Dasgupta, T. *Phys. Rev. B.* **1998**, *57*, R12655.
- [31] Valenti, R.; Saha-Dasgupta, T.; Alvarez, J. V.; Požgajčić, K.; Gros, C. *Phys. Rev. Lett.* **2001**, *86*, 5381.
- [32] Pavarini, E.; Dasgupta, I.; Saha-Dasgupta, T.; Jepsen, O.; Andersen, O. K. *Phys. Rev. Lett.* **2001**, *87*, 047003.
- [33] Williamson, A. J.; Hood, R. Q.; Grossman, J. C. *Phys. Rev. Lett.* **2001**, *87*, 246406.
- [34] Williamson, A. J.; Grossman, J. C.; Hood, R. Q.; Puzder, A.; Galli, G. *Phys. Rev. Lett.* **2002**, *89*, 196803.

- [35] Kohn, W.; Rostocker, J. *Phys. Rev.* **1954**, *94*, 1111.
- [36] Korringa, J. *Physica* **1947**, *13*, 392.
- [37] Trucano, P.; Chen, R. *Nature* **1975**, *258*, 136.
- [38] Pease, R. S. *Acta Crystallographica* **1952**, *5*, 356.
- [39] Andersen, O. K.; Jepsen, O. *Phys. Rev. Lett.* **1984**, *53*, 2571.
- [40] Vosko, S. H.; Wilk, L.; Nusair, M. *Can. J. Phys.* **1980**, *58*, 1200.
- [41] Perdew, J. P.; Wang, Y. *Phys. Rev. B.* **1986**, *33*, 8800.
- [42] Blöchl, P. E.; Jepsen, O.; Andersen, O. K. *Phys. Rev. B.* **1994**, *49*, 16223.
- [43] Ahuja, R.; Auluck, S.; Trygg, J.; Wills, J. M.; Eriksson, O.; Johansson, B. *Phys. Rev. B.* **1995**, *51*, 4813.
- [44] Catellani, A.; Posternak, M.; Baldereschi, A.; Freeman, A. J. *Phys. Rev. B.* **1987**, *36*, 6105.
- [45] Hall, H. T.; Merrill, L.; Barnett, J. D. *Science* **1964**, *146*, 1297.
- [46] McMahon, M.; Nelves, R.; Rekhi, S. *Phys. Rev. Lett.* **2001**, *87*, 255502.
- [47] Takemura, K.; Minomura, S.; Shimomura, O. *Phys. Rev. Lett.* **1982**, *49*, 1772.
- [48] Schwarz, U.; Takemura, K.; Hanfland, M.; Syassen, K. *Phys. Rev. Lett.* **1998**, *81*, 2711.
- [49] Takemura, K.; Christensen, N. E.; Novikov, D. L.; Syassen, K.; Schwarz, U.; Hanfland, M. *Phys. Rev. B* **2000**, *61*, 14399.
- [50] Wittig, J. *Phys. Rev. Lett.* **1970**, *24*, 812.
- [51] Sternheimer, R. *Phys. Rev.* **1950**, *78*, 235.
- [52] Takemura, K.; Shimomura, O. *Phys. Rev. Lett.* **1991**, *66*, 2014-2017.
- [53] Schwarz, U.; Jepsen, O.; Syassen, K. *Solid State Communications* **2000**, *113*, 643-648.
- [54] Ahuja, R.; Eriksson, O.; Johansson, B. *Phys. Rev. B.* **2000**, *63*, 014102.
- [55] McMahan, A. K. *Phys. Rev. B* **1978**, *17*, 1521.
- [56] Glötzel, D.; McMahan, A. K. *Phys. Rev. B* **1979**, *20*, 3210.

- [57] McMahan, A. K. *Phys. Rev. B* **1984**, 29, 5982.
- [58] Christensen, N. E.; Boers, D. J.; van Velsen, J. L.; Novikov, D. L. *Phys. Rev. B* **2000**, 61, R3764.
- [59] Christensen, N. E.; Boers, D. J.; van Velsen, J. L.; Novikov, D. L. *J. Phys. Condens. Matter* **2000**, 12, 3293.
- [60] Kong, Y.; Jepsen, O. *Phys.: Condens. Matter* **2000**, 12, 8973-8982.
- [61] Osorio-Guillén, J. M.; Ahuja, R.; Johansson, B. *ChemPhysChem* **2004**, 5, 1411-1415.
- [62] Katzke, H.; Tolédano, P. *Phys. Rev. B* **2005**, 71, 184101.
- [63] Tse, J. Z. *Kristallogr.* **2005**, 220, 521-530.
- [64] Anderson, M. S.; Gutman, E. J.; Packard, J. R.; Swenson, C. A. *J. Phys. Chem. Solids* **1969**, 30, 1587.
- [65] Perdew, J. P.; Burke, K.; Ernzerhof, M. *Phys. Rev. Lett.* **1996**, 77, 3865-3868.
- [66] Kasinathan, D.; Kunes, J.; Lazicki, A.; Rosner, H.; Yoo, C. S.; Scalettar, R. T.; Pickett, W. E. *Phys. Rev. Lett.* **2006**, 96, 047004.
- [67] Kohn, W. *Phys. Rev. Lett.* **1996**, 76, 3168.
- [68] Jacobson, E. L.; Freeman, R. D.; Tharp, A. G.; Searcy, A. W. *J. Am. Chem. Soc.* **1956**, 78, 4850-4852.
- [69] Brown, A. *Acta. Cryst.* **1961**, 14, 860-865.
- [70] Hardy, G. F.; Hulm, J. K. *Phys. Rev.* **1954**, 93, 1004-1016.
- [71] Chevalier, B.; Zhong, W. X.; Buffat, B.; Etourneau, J.; Hagenmuller, P. *Mat. Res. Bull.* **1986**, 21, 183-194.
- [72] Lejay, P.; Chevalier, B.; Etourneau, J.; Tarascon, J. M.; Hagenmuller, P. *Mat. Res. Bull.* **1983**, 18, 67-71.
- [73] Zhong, W. X.; Ng, W. L.; Chevalier, B.; Etourneau, J.; Hagenmuller, P. *Mat. Res. Bull.* **1985**, 20, 1229-1238.
- [74] Zheng, C.; Hoffmann, R. *Inorg. Chem.* **1989**, 28, 1074-1080.
- [75] Von Schnering, H. G.; Nesper, R. *Angew. Chem. Int. Ed. Engl.* **1987**, 26, 1059.

- [76] Brauer, G.; Mitius, A. *Zeitschrift fuer Anorganische und Allgemeine Chemie* **1942**, *249*, 325-339.
- [77] Iijima, S. *Nature* **1991**, *354*, 56-58.
- [78] Minett, A.; Atkinson, K.; Roth, S. Carbon nanotubes. In *Handbook of porous solids*; Schüth, F.; Sing, S. W.; Weitkamp, J., Eds.; Wiley-VCH: Weinheim, 2002.
- [79] Yao, Z.; Postma, H. W. C.; Balents, L.; Dekker, C. *Nature* **1999**, *402*, 273-276.
- [80] Zhou, O.; Shimoda, H.; Gao, B.; Oh, S.; Fleming, L.; Yue, G. *Acc. Chem. Res.* **2002**, *35*, 1045-1053.
- [81] Baughman, R. H.; Cui, C.; Zakhidov, A. A.; Iqbal, Z.; Barisci, J. N.; Spinks, G. M.; Wallace, G. G.; Mazzoldi, A.; De Rossi, D.; Rinzler, A. G.; Jaschinski, O.; Roth, S.; Kertesz, M. *Science* **1999**, *284*, 1340-1344.
- [82] Gao, H.; Kong, Y.; Cui, D. *Nano Letters* **2003**, *3*, 471-473.
- [83] Yudasaka, M.; Komatsu, T.; Ichihashi, T.; Achiba, Y.; Iijima, S. *J. Phys. Chem. B.* **1998**, *102*, 4892-4896.
- [84] Zhang, M.; Yudasaka, M.; Iijima, S. *J. Phys. Chem. B.* **2004**, *108*, 149-153.
- [85] Bandow, S.; Asaka, S.; Saito, Y.; Rao, A. M.; Grigorian, L.; Richter, E.; Eklund, P. C. *Phys. Rev. Lett.* **1998**, *80*, 3779-3782.
- [86] Krupke, R.; Hennrich, F.; v. Löhneysen, H.; Kappes, M. M. *Science* **2003**, *301*, 344-347.
- [87] Zheng, M.; Jagota, A.; Strano, M. S.; Santos, A. P.; Barone, P.; Chou, S. G.; Diner, B. A.; Dresselhaus, M. S.; McLean, R. S.; Onoa, G. B.; Samsonidze, G. G.; Semke, E. D.; Usrey, M.; Walls, D. J. *Science* **2003**, *302*, 1545-1548.
- [88] Ciosłowski, J.; Rao, N.; Moncrieff, D. *J. Am. Chem. Soc.* **2002**, *124*, 8485-8489.
- [89] Zhou, Z.; Steigerwald, M.; Hybertsen, M.; Brus, L.; Friesner, R. A. *J. Am. Chem. Soc.* **2004**, *126*, 3597-3607.
- [90] Yumura, T.; Hirahara, K.; Bandow, S.; Yoshizawa, K.; Iijima, S. *Chem. Phys. Lett.* **2004**, *386*, 38-43.
- [91] Nomura, Y.; Fujita, H.; Narita, S.; Shibuya, T. *Chem. Phys. Lett.* **2003**, *375*, 72-75.
- [92] Ciosłowski, J.; Rao, N.; Pernal, K.; Moncrieff, D. *J. Chem. Phys.* **2003**, *118*, 4456-4462.

- [93] Reiher, M.; Neugebauer, J. *J. Chem. Phys.* **2003**, *118*, 1634-1641.
- [94] Rochefort, A.; Salahub, D. R.; Avouris, P. *J. Phys. Chem. B.* **1999**, *103*, 641-646.
- [95] Latil, S.; Henrard, L.; Goze Bac, C.; Bernier, P.; Rubio, A. *Phys. Rev. Lett.* **2001**, *86*, 3160-3163.
- [96] Goze-Bac, C.; Latil, S.; Lauginie, P.; Jourdain, V.; Conard, J.; Duclaux, L.; Rubio, A.; Bernier, P. *Carbon* **2002**, *40*, 1825-1842.
- [97] Goze Bac, C.; Latil, S.; Vaccarini, L.; Bernier, P.; Gaveau, P.; Tahir, S.; Micholet, V.; Aznar, R. *Phys. Rev. B.* **2001**, *63*, 100302.
- [98] Tang, X.-P.; Kleinhammes, A.; Shimoda, H.; Fleming, L.; Bennoune, K. Y.; Shina, S.; Bower, C.; Zhou, O.; Wu, Y. *Science* **2000**, *288*, 492-494.
- [99] Hayashi, S.; Hoshi, F.; Ishikura, T.; Yumura, M.; Ohshima, S. *Carbon* **2003**, *41*, 3047-3056.
- [100] Kitaygorodskiy, A.; Wang, W.; Xie, S.-Y.; Lin, Y.; Fernando, K. A. S.; Wang, X.; Qu, L.; Chen, B.; Sun, Y.-P. *J. Am. Chem. Soc.* **2005**, *127*, 7517-7520.
- [101] Baerends, E. J. *et al.* "Amsterdam Density Functional, Theoretical Chemistry, Vrije Universiteit, Amsterdam", URL <http://www.scm.com>.
- [102] te Velde, G.; Bickelhaupt, F. M.; Baerends, E. J.; van Gisbergen, S. J. A.; Fonseca Guerra, C.; Snijders, J. G.; Ziegler, T. *J. Comput. Chem.* **2001**, *22*, 931-967.
- [103] Zhang, Y.; Yang, W. *Phys. Rev. Lett.* **1998**, *80*, 890.
- [104] Perdew, J. P.; Burke, K.; Ernzerhof, M. *Phys. Rev. Lett.* **1998**, *80*, 891.
- [105] Hammer, B.; Hansen, L. B.; Norskov, J. K. *Phys. Rev. B.* **1999**, *59*, 7413-7421.
- [106] Schreckenbach, G.; Ziegler, T. *J. Phys. Chem.* **1995**, *99*, 606-611.
- [107] Schreckenbach, G.; Ziegler, T. *Int. J. Quantum Chem.* **1996**, *60*, 753-766.
- [108] Schreckenbach, G.; Dickson, R. M.; Ruiz-Morales, Y.; Ziegler, T. The calculation of NMR parameters by density-functional theory. In *Chemical Applications of Density-Functional Theory*, Vol. 629; Laird, B. B.; Ross, R. B.; Ziegler, T., Eds.; American Chemical Society: Washington, 1996.
- [109] Schreckenbach, G.; Ziegler, T. *Theor. Chem. Acc.* **1998**, *99*, 71-82.

- [110] Hertel, I. V.; Steger, H.; de Vries, J.; Weisser, B.; Menzel, C.; Kamke, B.; Kamke, W. *Phys. Rev. Lett.* **1992**, *68*, 784-787.
- [111] Yoo, R. K.; Ruscic, B.; Berkowitz, J. *J. Chem. Phys.* **1992**, *96*, 911-918.
- [112] de Vries, J.; Steger, H.; Kamke, B.; Menzel, C.; Weisser, B.; Kamke, W.; Hertel, I. V. *Chem. Phys. Lett.* **1992**, *188*, 159-162.
- [113] Steger, H.; Holzapfel, J.; Hielscher, A.; Kamke, W.; Hertel, I. V. *Chem. Phys. Lett.* **1995**, *234*, 455-459.
- [114] Brink, C.; Andersen, L. H.; Hvelplund, P.; Mathur, D.; Voldstad, J. D. *Chem. Phys. Lett.* **1995**, *233*, 52-56.
- [115] Wang, X. B.; Ding, C.-F.; Wang, L.-S. *J. Chem. Phys.* **1999**, *110*, 8217-8220.
- [116] Casida, M. E. Time-dependent density functional response theory for molecules. In *Recent advances in density functional methods*, Vol. 1; Chong, D. P., Ed.; World Scientific: Singapore, 1995.
- [117] Kokalj, A. *J. Mol. Graphics Modelling* **1999**, *17*, 176-179 Code available from <http://www.xcrysden.org/>.
- [118] Flükiger, P.; Lüthi, H.; Portmann, S.; Weber, J. "Molekel 4.0", Swiss Center for Scientific Computing, Manno (Switzerland), 2000.
- [119] White, C. T.; Robertson, D. H.; Mintmire, J. W. *Phys. Rev. B.* **1993**, *47*, 5485-5488.
- [120] Saito, R.; Fujita, M.; Dresselhaus, G.; Dresselhaus, M. S. *Phys. Rev. B.* **1992**, *46*, 1804-1811.
- [121] Hamada, N.; Sawada, S.; Oshiyama, A. *Phys. Rev. Lett.* **1992**, *68*, 1579-1581.
- [122] Mintmire, J. W.; Dunlap, B. I.; White, C. T. *Phys. Rev. Lett.* **1992**, *68*, 631-634.
- [123] Blase, X.; Benedict, L. X.; Shirley, E. L.; Louie, S. G. *Phys. Rev. Lett.* **1994**, *72*, 1878-1881.
- [124] Ouyang, M.; Huang, J.-L.; Cheung, C. L.; Lieber, C. M. *Science* **2001**, *292*, 702-705.
- [125] Bulusheva, L. G.; Okotrub, A. V.; Romanov, D. A.; Tomanek, D. *J. Phys. Chem. A.* **1998**, *102*, 975-981.
- [126] Dresselhaus, M. S.; Dresselhaus, G.; Saito, R. *Phys. Rev. B.* **1992**, *45*, 6234-6242.

- [127] Taylor, R.; Hare, J. P.; Abdul-Sada, A. K.; Kroto, H. W. *J. Chem. Soc., Chem. Commun.* **1990**, 20, 1423-1424.
- [128] Martin, T. P.; Malinowski, N.; Zimmermann, U.; Näher, U.; Schaber, H. *J. Chem. Phys.* **1993**, 99, 4210-4212.
- [129] Zimmermann, U.; Malinowski, N.; Näher, U.; Frank, S.; Martin, T. P. *Phys. Rev. Lett.* **1994**, 72, 3542-3545.
- [130] Tast, F.; Malinowski, N.; Frank, S.; Heinebrodt, M.; Billas, I. M. L.; Martin, T. P. *Phys. Rev. Lett.* **1996**, 77, 3529-3532.
- [131] Enders, A.; Malinowski, N.; Ievlev, D.; Zurek, E.; Autschbach, J.; Kern, K. 2006 Submitted.
- [132] Branz, W.; Malinowski, N.; Enders, A.; Martin, T. P. *Phys. Rev. B* **2002**, 66, 094107.
- [133] Ievlev, D. N.; Küster, A.; Enders, A.; Malinowski, N.; Schaber, H.; Kern, K. *Rev. Sci. Inst.* **2003**, 74, 3031.
- [134] Weis, P.; Beck, R. D.; Gräuchle, G.; Kappes, M. M. *J. Chem. Phys.* **1994**, 100, 5684-5695.
- [135] Hamamoto, N.; Jitsukawa, J.; Satoko, C. *Eur. Phys. J. D.* **2002**, 19, 211-221.
- [136] Östling, D.; Rosén, A. *Chem. Phys. Lett.* **1997**, 281, 352-359.
- [137] Gong, X. G.; Kumar, V. *Chem. Phys. Lett.* **2001**, 334, 238-244.
- [138] Martin, T. P. *Physics Reports* **1983**, 95, 167.
- [139] R. Ahlrichs et al., Quantum Chemistry Group, Universitaet Karlsruhe, Turbomole, Version 5.4.
- [140] Vosko, S. H.; Wilk, L.; Nusair, M. *Can. J. Phys.* **1980**, 58, 1200-1211.
- [141] van Lenthe, E.; Baerends, E. J.; Snijders, J. G. *J. Chem. Phys.* **1993**, 99, 4597-4610.
- [142] van Lenthe, E.; Baerends, E. J.; Snijders, J. G. *J. Chem. Phys.* **1994**, 101, 9783-9792.
- [143] van Lenthe, E. *The ZORA Equation*, Thesis, Vrije Universiteit Amsterdam, Netherlands, 1996.
- [144] Dirac, P. A. M. *Proc. Royal Soc. (London) A* **1929**, 123, 714.
- [145] Slater, J. C. *Phys. Rev.* **1951**, 81, 385.

- [146] Perdew, J. P.; Chevary, J. A.; Vosko, S. H.; Jackson, K. A.; Pederson, M. R.; Singh, D. J.; Fiolhais, C. *Phys. Rev. B* **1992**, *46*, 6671-6687.
- [147] Eichkorn, K.; Treutler, O.; Öhm, H.; Häser, M.; Ahlrichs, R. *Chem. Phys. Lett.* **1995**, *242*, 652-660.
- [148] Eichkorn, K.; Treutler, O.; Öhm, H.; Häser, M.; Ahlrichs, R. *Chem. Phys. Lett.* **1995**, *240*, 283-289.
- [149] Kaupp, M.; Schleyer, P. v. R.; Stoll, H.; Preuss, H. *J. Chem. Phys.* **1991**, *94*, 1360.
- [150] Deglmann, P.; May, K.; Furche, F.; Ahlrichs, R. *Chem. Phys. Lett.* **2004**, *384*, 103.
- [151] Deglmann, P.; Furche, F.; Ahlrichs, R. *Chem. Phys. Lett.* **2002**, *362*, 511.
- [152] Scuseria, G. E. *Chem. Phys. Lett.* **1996**, *257*, 583-586.
- [153] Zhou, P.; Dong, Z. H.; Rao, A. M.; Eklund, P. C. *Chem. Phys. Lett.* **1993**, *211*, 337-340.
- [154] Gagliardi, L.; Pyykkö, P. *Theor. Chem. Acc.* **2003**, *110*, 205-210.
- [155] Pyykkö, P. *J. Chem. Soc. Faraday Trans. II* **1979**, *75*, 1256.
- [156] Gagliardi, L. *J. Am. Chem. Soc.* **2002**, *124*, 8757-8761.
- [157] Zurek, E.; Woo, T. K.; Firman, T. K.; Ziegler, T. *Inorg. Chem.* **2001**, *40*, 361-370.
- [158] Timoshkin, A. Y.; Schaefer, H. F. *Chemical Record* **2002**, *2*, 319-338.
- [159] Timoshkin, A. Y.; Schaefer, H. F. *J. Am. Chem. Soc.* **2004**, *126*, 12141-12154.
- [160] Yumura, T.; Bandow, S.; Yoshizawa, K.; Iijima, S. *J. Phys. Chem. B.* **2004**, *108*, 11426-11434.
- [161] Yumura, T.; Nozaki, D.; Bandow, S.; Yoshizawa, K.; Iijima, S. *J. Am. Chem. Soc.* **2005**, *127*, 11769-11776.

Acknowledgments

I would like to thank my supervisor, Professor Dr. Ole Krogh Andersen, for his guidance, insight and understanding. In particular, he has taught me how to see something within a mess of “spaghetti” and how orbitals may be used to gain a deeper understanding of a system. I am also grateful to Ole for giving me the freedom and support to pursue my own ideas and thankful for his friendship and humor.

Special thanks should be given especially to Professor Dr. Arndt Simon for his efforts as “Hauptberichter” and also to Professor Dr. Emil Roduner for taking the role as “Prüfungsvorsitzender” on my examination committee.

Dr. Hans-Georg Libuda must be acknowledged for organizing and coordinating not only the IMPRS-AM, but also for his constant assistance with day-to-day problems. Many thanks to the other members of the Research School for enjoyable scientific and non-scientific discussions.

Dr. Ove Jepsen has been particularly helpful in teaching me how to use and understand the LMTO and NMTO programs. He has also spent a considerable amount of time proofreading papers and even more importantly, this thesis. Through knowing Ove, I also managed to become a Danish cookie *connoisseur*. In fact, all of the members and visitors in Abteilung Andersen have always provided a very warm work atmosphere and entertaining conversations over coffee and cakes. I acknowledge Jens Kunstmann for editing the Zusammenfassung and Jochen Autschbach for writing it.

I am grateful to all of my collaborators. Especially to Professor Dr. Jochen Autschbach with whom I worked on the molecular calculations. I very much appreciated Jochen’s enthusiasm to tackle an interesting topic. Our work together has always been fruitful, enjoyable and has taught me much. I would also like to thank Jochen for his constant support, understanding, patience and nice times throughout these years.

I would like to acknowledge Dr. Axel Enders and Dr. Nikola Malinowski for being interested in an experimental/theoretical collaboration. Within our meetings they have provided many ideas and asked difficult questions that inspired much of the calculations on the metal-C₆₀ clusters. It was a great pleasure to work together.

My stay in Stuttgart would not have been half as pleasant and productive if it weren’t for the wonderful friends which I have made. Just to mention a few of these individuals: Paul

Bellina, Frank Baumann, Jadranka Čubrilo, Jean Rene Duclere, Craig Hawthorne, Omar Stern and Rodney Wiersma. Special thanks to Aleksandar Tucić, the best (and worst) roommate I could have ever had.

And finally I would like to thank my parents for their constant help, support, visits, travels throughout Europe, good cooking, understanding and friendship. I am grateful for the sacrifices they have made for me and for those they continue to make.

Lebenslauf

Name: Eva Dagmara Zurek
Geburtsdatum: 21.12.1976
Geburtsort: Krakau, Polen
Staatsangehörigkeit: Polnisch, Kanadisch

Schulausbildung

1982-1988 Sacred Heart Elementary School, Calgary, Canada.
1988-1991 St. Mary's Junior High School, Calgary, Canada.
1991-1994 Gymnasium am St. Mary's High School, Calgary, Canada.

Hochschulstudium

1994-2000 University of Calgary, Calgary, Canada.
Bachelor of Science in Chemistry.
1994-2000 University of Calgary, Calgary, Canada.
Bachelor of Science in Physics.
2000-2002 University of Calgary, Calgary, Canada.
Master of Science in Chemistry.
seit 11/2002 Anfertigen der vorliegenden Dissertation am Max-Planck-
Institut für Festkörperforschung bei Prof. Ole Krogh Andersen.

Stipendien und Auszeichnungen

11/2002-04/2006 IMPRS-AM fellowship
(International Max Planck Research School for Advanced Materials).

09/2001-09/2002	Masters scholarship (Alberta Learning).
09/2001-11/2002	Alberta Ingenuity fellowship.
09/2001-05/2002	Graduate Research scholarship.
06/2000	Hypercube Award.
09/1999-01/2000	Undergraduate NSERC scholarship (National Sciences and Engineering Research Council).

Berufliche Erfahrungen/Praktika

05/1998-09/1998	Studentische Hilfskraft, University of Calgary, Betreuung durch Prof. Tom Ziegler.
05/1999-09/1999	Sommer Internship bei Akzo Nobel, Arnheim, Niederlande, Betreuung durch Dr. Erik Kirchner.
05/2000-09/2000	Studentische Hilfskraft, University of Calgary, Betreuung durch Prof. Tom Ziegler.

Publikationen

1. Zurek, E.; Woo, T. K.; Firman, T. K.; Ziegler, T.; "Modeling the dynamic equilibrium between oligomers of $(\text{AlOCH}_3)_n$ in Methylaluminoxane (MAO). A theoretical study based on a combined quantum mechanical and statistical mechanical approach." *Inorganic Chemistry*, **2001**, *40*, 361-370.
2. Zurek, E.; Ziegler, T.; "A combined quantum mechanical and statistical mechanical study of the equilibrium in trimethylaluminum (TMA) and oligomers of $(\text{AlOCH}_3)_n$ found in Methylaluminoxane (MAO)." *Inorganic Chemistry*, **2001**, *40*, 3279-3292.
3. Zurek, E.; Ziegler, T.; "Toward the identification of dormant and active species in MAO (Methylaluminoxane)-activated, dimethylzirconocene-catalyzed olefin polymerization." *Organometallics*, **2002**, *21*, 83-92.

4. Xu, Z.; Vanka, K.; Firman, T.; Michalak, A.; Zurek, E.; Zhu, C.; Ziegler, T.; "Theoretical study of the interactions between cations and anions in Group IV transition-metal catalysts for single-site homogeneous olefin polymerization." *Organometallics*, **2002**, *21*, 2444-2453.
5. Zurek, E.; Ziegler, T.; "A density functional study of the insertion mechanism in MAO (Methylaluminoxane)-activated, dimethylzirconocene-catalyzed olefin polymerization; further evidence for the structural assignment of dormant and active species." *Faraday Discussions*, **2003**, *124*, 93-109.
6. Autschbach, J.; Zurek, E.; "Relativistic density-functional computations of the chemical shift of ^{129}Xe in $\text{Xe}@C_{60}$." *Journal of Physical Chemistry A.*, **2003**, *107*, 4967-4972.
7. Zurek, E.; Ziegler, T.; "Theoretical studies of the structure and function of MAO (Methylaluminoxane)." *Progress in Polymer Science*, **2004**, *29*, 107-148.
8. Zurek, E.; Autschbach, J.; "Density functional calculations of the ^{13}C NMR chemical shifts in (9,0) single-walled carbon nanotubes." *Journal of the American Chemical Society*, **2004**, *126*, 13079-13088.
9. Zurek, E.; Jepsen, O.; Andersen, O. K. "NMTO Wannier-like functions for insulators and metals." *ChemPhysChem*, **2005**, *6*, 1934-1942.
10. Zurek, E.; Pickard, C. J.; Walczak, B.; Autschbach, J. "Density-Functional calculations of the ^{13}C NMR chemical shifts in small- to medium-diameter single-walled carbon nanotubes: Chemical shift range, comparison of finite-length with infinite tubes, and choice of the NMR reference in the computations." Submitted.
11. Enders, A.; Malinowski, N.; Ievlev, D.; Zurek, E.; Autschbach, J.; Kern, K. "Magic alkali-fullerene compound clusters of extreme thermal stability." Submitted.
12. Zurek, E.; Autschbach, J. "DFT studies of magic $(C_{60})_2$ -metal clusters." In preparation.